Nanoparticle Engineering for Neurotargeting in the Dorsal Root Ganglia

by

Thitikan Jirakittisonthon

DVM, Chulalongkorn University, 2013
MS, Kansas State University, 2016

AN ABSTRACT OF A DISSERTATION

submitted in partial fulfillment of the requirements for the degree

DOCTOR OF PHILOSOPHY

Department of Anatomy and Physiology
College of Veterinary Medicine

KANSAS STATE UNIVERSITY
Manhattan, Kansas

2026

Abstract

Dorsal Root Ganglia (DRG), clusters of neuronal cell bodies, are hubs for signal transduction and contain various neuroreceptors that mediate their functions, transmitting information from peripheral tissues to the central nervous system. Their neuroanatomy allows peripheral administration to the DRG. To take advantage of this opportunity to deliver drugs or molecules of interest, nanoparticles, both natural and synthetic, serve as useful vehicles (e.g., Extracellular Vesicles (EVs) or liposomes). However, unmodified forms may lack preferential targeting of non-target tissues or cells. Therefore, this study aims to functionalize nanoparticles (EVs and liposomes) to target preferred cells in the DRG. The selected ligands are Cholera Toxin B (CTB) and Wheat Germ Agglutinin (WGA), chosen based on previous findings in a neurotracing study showing that tagging with Horseradish Peroxidase (HRP) is specific to large DRG and small DRG, respectively. Large DRG contain mainly proprioceptors and mechanoreceptors, and small DRG are enriched in nociceptors. However, size relates to the sensory neuron population but does not definitively determine sensory function. Therefore, this strategy can be applied to nanoparticles to specifically target cells of interest.

To achieve this, I have 2 sub-aims. First, CTB and WGA will be tagged with EVs. Second, those ligands will be tagged to liposomes. To achieve aim 1, EVs were produced and isolated from Mesenchymal Stromal Cell Conditioned Media (MSCs-CM) under Good Manufacturing Practice (GMP) conditions and used in subsequent experiments. It was demonstrated that different tagging methods, either the Avidin-Biotin Conjugation method (biotinylating EVs with avidin and biotinylating CTB to make CTB-EVs) or the lipid-linking method (using DOPE-PEG-NHS), successfully conjugated EVs to CTB and increased cellular uptake in neuronal cell lines, ACS 5004. The lipid-linking method was chosen because it is simpler and performed better. Next,

WGA-EVs were tested in vitro. Unfortunately, WGA-EVs did not show the same neural cell-line-specific uptake trend as CTB-EVs did. To further test this hypothesis, an animal model was used to compare peripheral injection of CTB-EVs and WGA-EVs. The in vivo results showed that CTB-EVs were preferentially taken up by medium- to large-sized neurons. However, WGA-EVs did not provide enough information for further analysis.

To address aim 2, liposomes, CTB-liposomes, and WGA-liposomes were tested in neural cell lines, as in aim 1. Liposome batches were prepared using the thin-film hydration method. The results showed no ACS 5004-specific cellular uptake for CTB-liposomes or WGA-liposomes across the different nanoparticles. Therefore, advanced in vivo testing of these CTB-liposomes and WGA-liposomes was not conducted.

In summary, both the ligands and the nanoparticle type can affect cellular uptake. CTB-EVs prefer medium-to-large neurons, while WGA-EVs show no preference for small neurons. This finding is not observed in liposomes. Further optimization of liposome membrane/lipid composition may help better determine cellular uptake preferences.

Nanoparticle Engineering for Neurotargeting in the Dorsal Root Ganglia

by

Thitikan Jirakittisonthon

DVM, Chulalongkorn University, 2013
MS, Kansas State University, 2016

A DISSERTATION

submitted in partial fulfillment of the requirements for the degree

DOCTOR OF PHILOSOPHY

Department of Anatomy and Physiology
College of Veterinary Medicine

KANSAS STATE UNIVERSITY
Manhattan, Kansas

2026

Approved by:

Major Professor
Dr. Mark L. Weiss

Copyright

© Thitikan Jirakittisonthon 2026.

Abstract

Dorsal Root Ganglia (DRG), clusters of neuronal cell bodies, are hubs for signal transduction and contain various neuroreceptors that mediate their functions, transmitting information from peripheral tissues to the central nervous system. Their neuroanatomy allows peripheral administration to the DRG. To take advantage of this opportunity to deliver drugs or molecules of interest, nanoparticles, both natural and synthetic, serve as useful vehicles (e.g., Extracellular Vesicles (EVs) or liposomes). However, unmodified forms may not preferentially target non-target tissues or cells. Therefore, this study aims to functionalize nanoparticles (EVs and liposomes) to target preferred cells in the DRG. The selected ligands are Cholera Toxin B (CTB) and Wheat Germ Agglutinin (WGA), chosen based on previous findings in a neurotracing study showing that tagging with Horseradish Peroxidase (HRP) is specific to large DRG and small DRG, respectively. Large DRG contain mainly proprioceptors and mechanoreceptors, and small DRG are enriched in nociceptors. However, size relates to the sensory neuron population but does not definitively determine sensory function. Therefore, this strategy can be applied to nanoparticles to specifically target cells of interest.

To achieve this, I have 2 sub-aims. First, CTB and WGA will be tagged with EVs. Second, those ligands will be tagged to liposomes. To achieve aim 1, EVs were produced and isolated from Mesenchymal Stromal Cell Conditioned Media (MSCs-CM) under Good Manufacturing Practice (GMP) conditions and used in subsequent experiments. It was demonstrated that different tagging methods, either the Avidin Biotin Conjugation method (biotinylating EVs with avidin and biotinylating CTB to make CTB-EVs) or the lipid-linking method (using DOPE-PEG-NHS), successfully conjugated EVs to CTB and increased cellular uptake in neuronal cell lines, ACS 5004. The lipid-linking method was chosen because it is simpler and performed better. Next,

WGA-EVs were tested in vitro. Unfortunately, WGA-EVs did not show the same neural cell-line-specific uptake trend as CTB-EVs did. To further test this hypothesis, an animal model was used to compare peripheral injection of CTB-EVs and WGA-EVs. The in vivo results showed that CTB-EVs were preferentially taken up by medium- to large-sized neurons. However, WGA-EVs did not provide enough information for further analysis.

To address aim 2, liposomes, CTB-liposomes, and WGA-liposomes were tested in neural cell lines, as in aim 1. Liposome batches were prepared using the thin-film hydration method. The results showed no ACS 5004-specific cellular uptake for CTB-liposomes or WGA-liposomes across the different nanoparticles. Therefore, advanced in vivo testing of these CTB-liposomes and WGA-liposomes was not conducted.

In summary, both the ligands and the nanoparticle type can affect cellular uptake. CTB-EVs prefer medium-to-large neurons, while WGA-EVs show no preference for small neurons. This finding is not observed in liposomes. Further optimization of liposome membrane/lipid composition may help better determine cellular uptake preferences.

.

Table of Contents

List of Figures xi
List of Tables xv
Acknowledgements xviii
Dedication xx
Chapter 1 - Introduction 1
Dorsal Root Ganglion (DRG) 2
CTB and WGA 3
Nanoparticle-based drug delivery to the nervous system 4
Extracellular Vesicles 5
Liposomes 5
Nanoparticles Surface Engineering 6
Biological Approach--Genetic Engineering 7
Chemical Approach 11
Lipid-linking method 11
ABC method 12
Click chemistry 12
Have any ligands been used for neuron targeting? 14
Summary 18
Chapter 2 - CTB and WGA Functionalized Nanoparticles Targeting Neurons in the Dorsal Root Ganglia 20
Abstract 20
Introduction 21
Materials and Methods 24
EVs Isolation 24
Liposomes manufacturing 25
Characterization of EVs and liposomes 26
Protein quantitation and analysis 27
Modification of EVs and liposomes with CTB or WGA 27
Quantitative analysis of ligand tagging to EVs 28

PKH 26 Staining of EVs and liposomes 29
Cell culture 29
MTT assay 30
In Vitro uptake analysis 30
Loading fluorescent proteins into EVs 31
In Vivo Assay 32
Animals and procedures 32
Imaging 34
Histology 34
Immunofluorescence staining 35
Data analysis 35
Results 36
Experimental Overview 37
Exp 1. Yield and Purity Analysis of EV Production from Mesenchymal Stromal Cells Conditioned Media (MSCs-CM) derived from Good Manufacturing Practice (GMP) MSC production runs 37
Exp 1b. EVs Characterization 40
Exp 2. Comparison of EV conjugation methods 40
EV characterization after surface modification. 41
Cellular uptake comparison of the different methods for conjugating CTB onto EVs 43
Experiment 3a. 50
Lipid-linking method for WGA-EVs (In Vitro Analysis: dose-response) 50
EV characterization after surface modification. 50
Cellular uptake comparison of WGA-EVs and naïve EVs. 50
Experiment 3b: Lipid-linking method for CTB, WGA, to liposomes (In Vitro Analysis:dose-response) 53
Cellular uptake comparison of liposomes conjugated with CTB or WGA (CTB-liposomes and WGA-liposomes) 54
Metabolic activity assessment of CTB-EVs, CTB-liposomes, WGA-EVs, and WGA-liposomes on ACS 5004 and HEK 293 57
Experiment 4a: Fluorogold injection to determine the end of the experiment 58

Experiment 4b: Loading eGFP/ mCherry-EVs (In vitro analysis) 58
Experimental 4c: eGFP-CTB EVs vs mCherry-EVs (In vivo analysis) 61
Experimental 4d: eGFP-WGA EVs vs mCherry-EVs (In vivo analysis) 64
Discussion 65
Using CM from GMP production to generate EVs: Purity and Yield 66
Nanoparticle Characterization 67
Ligand binding methods 70
Ligand testing for retrograde transport to DRG after peripheral injection 71
Alternative to CTB and WGA 72
Chapter 3 - Conclusion 75
Appendix A - Supplemental Materials and Methods 78
Appendix B - Supplementary Figures and Tables 83

List of Figures

Figure 1.1. Surface Modification of EVs 7
Figure 1.2. Engineering of CD 63 with RFP and GFP 9
Figure 1.3. Ligands on EVs surface 15
Figure 2.1. Labeling of neurons in DRG after WGA-HRP or CTB-HRP injection. WGA-HRP injection predominantly labels small-diameter DRG neurons (left), while CTB-HRP injection predominantly labels large-diameter DRG neurons (right) [1]. 24
Figure 2.5. Experimental Schematic: Extracellular Vesicles (EVs) were isolated from human mesenchymal stromal cells conditioned medium (MSCs-CM) using either tangential flow filtration (TFF) and size exclusion chromatography (SEC) or SEC alone. Liposomes were prepared by thin-film hydration. The two conjugation methods for attaching CTB to EVs were compared for efficiency via in vitro uptake. CTB- and WGA-conjugated EVs and liposomes were compared in vitro. Next, fluorogold injection experiments were performed, followed by comparison of loading with either eGFP or eGFP. To determine fluorescence Localization, CTB-EVs were compared with EVs, and WGA-EVs were compared with EVs, to assess uptake after injection into the hind footpad of rats. 36
Figure 2.6. Yield and Purity Analysis of EV Production from CM. (a) Yield (total EV particles for each CM isolation) and regression analysis showed a positive correlation between CM (mL) and yield (CM volume as the x variable, p=0.01). (b) EV particle per 1 mL of CM. mean = 3.71 x 1010 ± 1.98 x 1010 EV particle per 1 mL of CM, median = 3.87 x 1010 EV particle per 1 mL of CM. (c) EV particle per 1 mL of CM based on each isolation (CM (mL)). (d) Purity (EV particles/ ug protein). The yield and purity of EVs isolated from CM were not impacted by batch effects or isolation method. 39
Figure 2.7. EVs characterization and their purity comparison of ligand conjugation: Western blot for (a) CD9, CD63, CD81, and β-actin detection. Naïve EVs were positive for all EV markers. (b) CTB detection. After EV conjugation with CTB, CTB-EVs were positive for CTB. (c) Purity of EVs and CTB-EVs. CTB-EVS with both the ABC method and the lipid-linking method tend to decrease purity compared to naïve EVs. 42

Figure 2.8. Uptake of EVs or CTB-EVs by two cell lines: ACS 5004 and HEK 293. (a) Representative confocal microscopy images of EVs or CTB-EVs (EV membrane labeled with the lipophilic membrane dye PKH 26, red) in ACS 5004 and HEK 293 cells at different doses (0.25, 1.25, 6.25, 31.25, and 156.25 pM) using the ABC method. (b) Representative confocal microscopy images of EVs and CTB-EVs (labeled with the lipophilic membrane dye PKH 26, red) in ACS 5004 and HEK 293 at different doses (6.25, 31.25, 156.25, and 781.25 pM) using the lipid-linking method. (c) Quantitative analysis of the ABC method. CTB-EVs were taken up in a dose-dependent manner by ACS 5004 cells. (d) Quantitative analysis of the lipid-linking method. (Calibration bar = 20 μm, brightness and contrast adjusted). Note: Both ABC method and lipid linker method for CTB conjugation on EVs were successful and tend to be specific to ACS 5004 more than HEK 293..... 47

Figure 2.9. Uptake of EVs or WGA-EVs by two cell lines: ACS 5004 and HEK 293. (a) Representative confocal microscopy images of EVs or WGA-EVs (EV membrane labeled with the lipophilic membrane dye PKH 26, red) in ACS 5004 and HEK 293 cells at different doses (6.25, 31.25, 156.25, 781.25 pM) using the lipid-linking method. (b) Quantitative analysis using the lipid-linking method indicated that ACS 5004 did not specifically take up WGA-EVs. (Calibration bar = 20 μm, brightness and contrast adjusted). 52

Figure 2.10. Uptake of liposomes, CTB-liposomes, or WGA-liposomes by two cell lines: ACS 5004 and HEK 293. (a) Representative confocal microscopy images of liposomes, CTB-liposomes, or WGA-liposomes (liposome membrane labeled with the lipophilic membrane dye PKH 26, red) in ACS 5004 and HEK 293 cells at different doses (6.25, 31.25, 156.25, 781.25 pM). (b) Quantitative analysis showed that ACS 5004 did not specifically take up CTB-liposomes or WGA-liposomes. (Calibration bar = 20 μm, brightness and contrast adjusted)..... 56

Figure 2.11. Loading of fluorescent protein into EVs using various methods and detection. (a) Western blot of eGFP-EVs under different treatments after EV loading with eGFP. (a(1).) eGFP was loaded into EVs at RT or 37 °C, then subjected to various treatments to determine its localization. (a (2).) eGFP was loaded into EVs at RT or by sonication, then subjected to various treatments to determine its localization. (b) Western blot of (b (1))

eGFP-EVs or (b (2)) mCherry-EVs under different treatments after EV loading. (c) Fluorescent detection of naïve EVs, eGFP-EVs, and mCherry-EVs. (d) Fluorescent detection of eGFP-CTB-EVs and eGFP-WGA-EVs. (RT: room temperature, PK: proteinase K, PI: protease inhibitor, TX: Triton X-100). Note: eGFP and mCherry were successfully loaded into EVs. eGFP was present on the membrane and inside, whereas mCherry was membrane-only. 59

Figure 2.12 CTB-EVs vs EVs uptake analysis in an animal model. (a) Footpad thickness of animals. (b) Analysis using the IVIS system. Note: No statistically significant difference between CTB-EVs and EVs uptake in different organs. (c) Representative confocal microscopy images of mCherry-EVs or eGFP-CTB-EVs in DRG. (d) Quantitative analysis using a binomial model of CTB and EVs in DRG, and quantitative analysis of the number of detected observations of CTB and EVs in DRG. 62

Figure 2.13. WGA-EVs vs EVs uptake analysis in an animal model. (a) Footpad thickness of animals. (b) Analysis using the IVIS system. Note: No statistically significant difference between WGA-EVs and EVs uptake in different organs. (c) Representative confocal microscopy images of mCherry-EVs or eGFP-CTB-EVs in DRG..... 65

.

Appendix Figure B.1. EV characterization using NTA and TEM..... 83

Appendix Figure B.2. Measurement of EV samples: mean and mode size by NTA and mean size, PDI, and Z-potential by DLS. 88

Appendix Figure B.3. CTB control standard curve and quantification. 90

Appendix Figure B.4. Western Blot of WGA detection. After EV conjugation with WGA, WGA-EVs were positive for WGA. 92

Appendix Figure B.5. Liposome characterizations. (experiment 3b)..... 93

Appendix Figure B.6. Dose-response effects of EVs, CTB-EVs, WGA-EVs, liposomes, CTB-liposomes, and WGA-liposomes on ACS5004 or HEK293 cell proliferation, as measured by the MTT assay. (a) EVs in ACS 5004 cells. (b) EVs in HEK 293 cells. No trend or significance was observed across all doses, treatments, and cell lines. (c) Liposomes in ACS 5004 cells. (b) Liposomes in HEK 293 cells. No trend or significance was observed across all doses, treatments, and cell lines. 95

Appendix Figure B.7. Uptake of Fluorogold (FG) in Dorsal Root Ganglia (DRG). (a) Representative fluorescent microscopy images of negative controls and FG detection on days 5 and 7 after injection. (b) Quantitative analysis of FG detection on days 5 and 7 after injection. No difference in the % of FG-positive cells across days after injection. (Calibration bar = 100 µm, brightness and contrast adjusted) 96

List of Tables

Figure 1.1. Surface Modification of EVs 7
Figure 1.2. Engineering of CD 63 with RFP and GFP 9
Figure 1.3. Ligands on EVs surface 15
Figure 2.1. Labeling of neurons in DRG after WGA-HRP or CTB-HRP injection. WGA-HRP injection predominantly labels small-diameter DRG neurons (left), while CTB-HRP injection predominantly labels large-diameter DRG neurons (right) [1]. 24
Figure 2.5. Experimental Schematic: We isolated extracellular vesicles (EVs) from human mesenchymal stromal cell conditioned medium (MSCs-CM) using either tangential flow filtration (TFF) and size exclusion chromatography (SEC) or SEC alone. Liposomes were prepared by thin-film hydration. We compared the efficiency of the two conjugation methods for attaching CTB to EVs by in vitro uptake. We compared CTB- and WGA-conjugated EVs and liposomes in vitro. Next, fluorogold injection experiments were performed, followed by comparison of loading with either eGFP or mCherry. To determine fluorescence Localization, CTB-EVs were compared with EVs, and WGA-EVs were compared with EVs, to assess uptake after injection into the hind footpad of rats. 36
Figure 2.6. Yield and Purity Analysis of EV Production from CM. (a) Yield (total EV particles for each CM isolation) and regression analysis showed a positive correlation between CM (mL) and yield (CM volume as the x variable, p=0.01). (b) EV particles per 1 mL of CM. mean = 3.71 x 1010 ± 1.98 x 1010 EV particle per 1 mL of CM, median = 3.87 x 1010 EV particle per 1 mL of CM. (c) EV particles per 1 mL of CM based on each isolation (CM (mL)). (d) Purity (EV particles/ ug protein). The yield and purity of EVs isolated from CM were not impacted by batch effects or isolation method 39
Figure 2.7. EV characterization and purity comparison of ligand conjugation: Western blot for (a) CD9, CD63, CD81, and β-actin detection. Naïve EVs were positive for all EV markers. (b) CTB detection. After EV conjugation with CTB, CTB-EVs were positive for CTB. (c) Purity of EVs and CTB-EVs. CTB-EVS with both the ABC method and the lipid-linking method tend to decrease purity compared to naïve EVs 42
Figure 2.8. Uptake of EVs or CTB-EVs by two cell lines: ACS 5004 and HEK 293. (a) Representative confocal microscopy images of EVs or CTB-EVs (EV membrane labeled

with the lipophilic membrane dye PKH 26, red) in ACS 5004 and HEK 293 cells at different doses (0.25, 1.25, 6.25, 31.25, and 156.25 pM) using the ABC method. (b) Representative confocal microscopy images of EVs and CTB-EVs (labeled with the lipophilic membrane dye PKH 26, red) in ACS 5004 and HEK 293 at different doses (6.25, 31.25, 156.25, and 781.25 pM) using the lipid-linking method. (c) Quantitative analysis of the ABC method. CTB-EVs were taken up in a dose-dependent manner by ACS 5004 cells. (d) Quantitative analysis of the lipid-linking method. (Calibration bar = 20 μm, brightness and contrast adjusted). Note: Both the ABC method and lipid linker method for CTB conjugation on EVs were successful and tend to be specific to ACS 5004 more than HEK 293..... 47

Figure 2.9. Uptake of EVs or WGA-EVs by two cell lines: ACS 5004 and HEK 293. (a) Representative confocal microscopy images of EVs or WGA-EVs (EV membrane labeled with the lipophilic membrane dye PKH 26, red) in ACS 5004 and HEK 293 cells at different doses (6.25, 31.25, 156.25, 781.25 pM) using the lipid-linking method. (b) Quantitative analysis using the lipid-linking method indicated that ACS 5004 did not specifically take up WGA-EVs. (Calibration bar = 20 μm, brightness and contrast adjusted). 52

Figure 2.10. Uptake of liposomes, CTB-liposomes, or WGA-liposomes by two cell lines: ACS 5004 and HEK 293. (a) Representative confocal microscopy images of liposomes, CTB-liposomes, or WGA-liposomes (liposome membrane labeled with the lipophilic membrane dye PKH 26, red) in ACS 5004 and HEK 293 cells at different doses (6.25, 31.25, 156.25, 781.25 pM). (b) Quantitative analysis showed that ACS 5004 did not specifically take up CTB-liposomes or WGA-liposomes. (Calibration bar = 20 μm, brightness and contrast adjusted)..... 56

Figure 2.11. Loading of fluorescent protein into EVs using various methods and detection. (a) Western blot of eGFP-EVs under different treatments after EV loading with eGFP. (a(1).) eGFP was loaded into EVs at RT or 37 °C, then subjected to various treatments to determine its localization. (a (2).) eGFP was loaded into EVs at RT or by sonication, then subjected to various treatments to determine its localization. (b) Western blot of (b (1)) eGFP-EVs or (b (2)) mCherry-EVs under different treatments after EV loading. (c) Fluorescent detection of naïve EVs, eGFP-EVs, and mCherry-EVs. (d) Fluorescent

detection of eGFP-CTB-EVs and eGFP-WGA-EVs. (RT: room temperature, PK: proteinase K, PI: protease inhibitor, TX: Triton X-100). Note: eGFP and mCherry were successfully loaded into EVs. eGFP was present on the membrane and inside, whereas mCherry was membrane-only. 59

Figure 2.12 CTB-EVs vs. EVs uptake analysis in an animal model. (a) Footpad thickness of animals. (b) Analysis using the IVIS system. Note: No statistically significant difference between CTB-EVs and EVs uptake in different organs. (c) Representative confocal microscopy images of mCherry-EVs or eGFP-CTB-EVs in DRG. (d) Quantitative analysis using a binomial model of CTB and EVs in DRG, and quantitative analysis of the number of detected observations of CTB and EVs in DRG. 62

Figure 2.13. WGA-EVs vs EVs uptake analysis in an animal model. (a) Footpad thickness of animals. (b) Analysis using the IVIS system. Note: No statistically significant difference between WGA-EVs and EVs uptake in different organs. (c) Representative confocal microscopy images of mCherry-EVs or eGFP-CTB-EVs in DRG..... 65

.

Appendix Table B.1. Physicochemical characterization of EVs (experiments 2 and 3a (in vitro experiments)) 85

Appendix Table B.2. Physicochemical characterization of EVs (experiments 4c and 4d (in vivo experiments)) 87

Appendix Table B.3. Physicochemical characterization of liposomes (experiment 3b) 91

Acknowledgements

First, I thank Dr. Mark L. Weiss. His invaluable guidance helped shape me into the scientist I am today. I am grateful that he believes in me, even when I don't. Without him, I could not have achieved this. Thank you also to the Thai government for granting me study leave. Thank you to the previous lab manager, Dr. Hong He, for assisting with the molecular experiment.

To the committee members, Dr. Mathew Basel, Dr. Butch KuKanich, and Dr. Shih-Kang Fan, thank you for your valuable time and guidance throughout my Ph.D. journey. Your guidance beyond EVs helped broaden my perspective.

To Dr. Larry Snyder, thank you for helping me with the NTA and DLS experiments whenever I asked, without hesitation. To Dr. Meena Kumari, thank you for your guidance in the EV field and for supporting me as a woman scientist. To Dr. Tej Shrestha and the CORE facility, thank you for your valuable time in helping me analyze the samples. To Joel Sanneman and the confocal facility, thank you for your help with the experimental setup and design. To the Comparative Medicine Group, thank you for caring for the animals in our experiments. To Marla Pyle, thank you for helping me troubleshoot experimental equipment, especially when Dr. Weiss was on sabbatical leave, and I had no one to help me with the Coles Hall 116 arrangement.

I thank MAI for helping me with the TEM, KU Medical Center for CM resources, and especially Dr. Soder Rupal, who served as a contact for valuable advice and resources.

Faculty members and staff are always supportive. When I need help, I know that if I ask, I will get answers. I feel that everyone is willing to help me.

Lastly, Dr. Jadsada Ratthanophart, my first boss and mentor, helped me from the very beginning, when I didn't know how to pipette, guided me, and changed my perspective, helping

me become a scientist in the laboratory. Dr. Kreeson Packthongsuk suggested me to Dr. Weiss, and without him, I would not have started my MS and PhD in Dr. Weiss's lab.

Without all of you, this journey would not have been possible. I am deeply grateful for all the support I have received, and I hope that one day I can pay it forward by supporting others in the same way; without them, my journey would not be easy. I will pay it forward.

Dedication

To my family for supporting me through texts, voice calls, and video calls. Every moment with you is valuable.

To Mathieu Smith for understanding me on the days when I needed emotional support. Thank you for always being there for me, calming me down when I felt overwhelmed and lifting me again when I needed it most.

To my friends in Thailand, here in the US, and in the Philippines. Thank you for your friendship, encouragement, and support throughout this journey

To me, for the moments when I doubted, but still chose to believe.

Chapter 1 - Introduction

My goal in generating this work is to target neurons in the dorsal root ganglia (DRG). I hypothesize that synthetic or natural nanoparticles can be engineered to enhance neuronal uptake. To achieve this objective, I break down my goal into two sub-goals: 1. Engineering extracellular vesicles (EVs) with ligands that specifically target small neurons and medium- to large neurons in the DRG, and 2—developing liposomes with those same ligands, as in EVs. The following paragraph will briefly elaborate on the literature supporting each sub-goal. Next, I will summarize the literature review to underpin my overall thesis work.

My first sub-goal is to target neurons after peripheral EV injection. I hypothesize that attaching the Cholera Toxin Beta subunit (CTB) or the lectin Wheat Germ Agglutinin (WGA) to the surface of extracellular vesicles (EVs) will enhance EV binding to neurons and subsequent cellular uptake compared with control naïve EVs. I will test this hypothesis by assessing retrograde transport of fluorescent particles to dorsal root ganglion (DRG) neurons following peripheral injection. I chose CTB because it binds the monosialo-ganglioside (GM1) receptor found in neural membrane lipid rafts. Previous work showed that injecting CTB conjugated to horseradish peroxidase (CTB-HRP) enhanced DRG neuron labeling compared with free HRP [1]. I also selected WGA because this lectin binds the carbohydrate N-acetylglucosamine (GlyNAc) found on neural membranes. Like CTB-HRP, WGA-HRP has been used as a neural tract tracer and has shown greater efficiency in labeling neurons than free HRP. Based on their previous use in neuroanatomical tract tracing, I propose labeling EVs with either CTB or WGA on their surface and testing whether this promotes neuronal uptake and retrograde transport to DRG neurons.

My second sub-goal is to engineer synthetic nanoparticles, specifically liposomes with the same ligands as the EVs mentioned above. Although no work has been done on WGA-liposome

engineering, previous work showed that CTB-liposomes successfully transported retrograde to the DRG after nerve injection [2]. Below, I review nanoparticle surface modification, focusing on strategies, techniques, and challenges.

Dorsal Root Ganglion (DRG)

The DRG is a cluster of sensory neuron cell bodies responsible for sensation, including light touch, temperature, proprioception, and nociception [3]. It consists of pseudo-unipolar neurons with T-shaped axons that carry signals from the peripheral nervous system to the central nervous system [4]. The trigeminal ganglion, which conducts head and neck sensation, and the vagal ganglia, which conduct visceral sensation, are structurally similar to the DRG. DRG neurons are surrounded by non-neuronal satellite glial cells and rare cells resembling local macrophages, whose functions remain poorly understood. The DRG also contains connective tissues, blood vessels, and nerve fibers.

DRG neurons in humans range from 20 to 100 um in diameter, larger than in rodents but with a similar distribution [4]. Human soma size diversity can be categorized as small (<25 um), medium (25-35 μm), and large (>35 um) in diameter [5]. Axonal fiber properties can also be categorized by conduction velocity as C-fibers (unmyelinated, slow conduction), Ad-fibers (thinly myelinated, intermediate conduction), and Aa/b-fibers (thickly myelinated, fast conduction) [6]. DRG size relates to axon type, with smaller neurons associated with C- and Ad-fibers (slow-to-intermediate conduction) and larger neurons associated with Aa/b-fibers (fast conduction) [7].

Researchers have long proposed a relationship between neuronal size, fiber type, and sensory function. Small neurons with unmyelinated C fibers are enriched for nociception, thermosensation, and pruriception, whereas medium-to-large neurons mainly signal as mechanoreceptors and proprioceptors [8,9]. However, neuronal size alone is not a reliable basis for

distinguishing functional properties, since morphological populations overlap across functions [10,11]. Specifically, small neurons contain many nociceptors, but this does not mean that small neurons are identified as nociceptors. For example, RNA sequencing shows that small neurons include one low-threshold mechanoreceptor and multiple mechanoheat nociceptor types [11]. Wang et al. report that mouse DRGs have 17 cell types based on molecular markers [12]. Therefore, size provides useful information for DRG characterization, but it is not definitive for defining sensory function.

DRG size, function, and molecular heterogeneitysupports targeting different populations rather than focusing on a single population. Therefore, propose the ligands Cholera toxin B (CTB) and Wheat Germ Agglutinin (WGA), which have been reported to target different DRG neuron subpopulations based on size, medium-to-large and small, respectively. This complementary labeling pattern provides a rationale for testing whether different targeting ligands can bias nanoparticle uptake toward distinct DRG neuronal populations.

CTB and WGA

I chose these two ligands, CTB and WGA, to test the hypothesis. I describe them in detail below.

Cholera toxin B (CTB) is derived from the cholera toxin of Vibrio cholerae. The A subunit is the toxic component, and the B subunit binds to the monoganglioside GM1 to mediate uptake [13]. Peripheral injections of CTB conjugated to HRP are retrogradely transported to DRG neurons, especially to large cell bodies [1] or to the trigeminal ganglion after facial skin injection [14], and label their axon terminals in the dorsal horn. CTB conjugated to fluorescent dye can travel via the phrenic nerves after pleural injections [15], and lipid-bilayer-encapsulated nanoparticles, called protocells, conjugated with CTB can also be retrogradely transported to the phrenic nerve [16].

Fukui and colleagues (2022) used CTB-conjugated liposomes and found retrograde transport to the DRG and spinal cord after peripheral injection. Their work showed that CTB-liposomes were superior to naïve liposomes for neural tracing in rat models [2]. This directly supports our hypothesis that adding ligands can improve neural uptake of EVs or liposomes.

Wheat germ agglutinin is a plant-based lectin that binds N-acetylglucosamine and sialic acid residues found on neurons. WGA-HRP injections have enhanced retrograde labeling compared to free HRP [17,18], especially in small cell bodies in DRG [19]. WGA-HRP injection into facial skin labels cells in the trigeminal ganglion [14]. One study showed that WGA conjugation on nanoparticles improved BBB crossing and reduced AB plaque deposition in the Alzheimer's disease model [20]. Based on these findings, the premise is that ligands can be conjugated to EVs or liposomes with Cholera toxin B and Wheat germ agglutinin and traffic to DRG neurons after peripheral injection.

In summary, these two ligands have several properties that support their use for nanoparticles. Tagging the vehicles with ligands via conjugation provides a rational approach to investigate uptake preferences among different DRG neuronal populations.

Nanoparticle-based drug delivery to the nervous system

Challenges in targeting the nervous system for drug delivery include off-target biodistribution after systemic administration; biological barriers, including the inaccessibility of the DRG, which is difficult to target directly; and pharmacokinetic and pharmacodynamic considerations. In DRG, another consideration is targeting the relevant neuronal populations after systemic or peripheral administration. Delivery vehicles can help address these challenges by improving cargo stability, biodistribution, cellular uptake, and targeting. EVs and liposomes are

strong candidates because both can encapsulate drugs or molecules and be engineered with ligands to target relevant populations and enhance uptake.

Extracellular Vesicles

Extracellular vesicles (EVs) are lipid bilayer, membrane-bound vesicles ranging from 50 nanometers to 1 micrometer. All cell types can release them. EVs were once considered cellular waste products; however, their role in intercellular communication under physiological and pathological conditions is now of growing interest. Based on size and biogenesis, the basic classes are exosomes, microvesicles, and apoptotic bodies. Exosomes are an EV subclass that originates from endocytic pathways and range from 30 to 200 nm. In contrast, microvesicles bud off the plasma membrane and range from 100 to 1000 nm, and apoptotic bodies form by blebbing or fragmentation during programmed cell death and are the largest, at 1000 nm [21]. EVs offer native biocompatibility due to their physiological components and low immunogenicity, but they exhibit low batch-to-batch homogeneity. Their complexity, driven by source and isolation methods, is difficult to characterize. Scaling EV manufacturing is also challenging. Currently, EVs are gaining attention for diagnostics and therapeutics, although none have yet been clinically approved by the FDA [22].

Liposomes

Liposomes are synthetic nanoparticles with a lamellar structure of phospholipid bilayers that form a spherical shape [23]. Lipids are amphipathic, allowing liposomes to encapsulate either hydrophobic or hydrophilic molecules [24]. They are therefore considered among the most effective and widely used nanocarriers. Liposomes are formulated with phospholipids as the major structural component, with cholesterol to increase phospholipid rigidity and polyethylene glycol

(PEG) to help prevent binding of blood opsonins and elimination from the system, thereby prolonging circulation time [25].

Liposomes are superior to EVs for batch-to-batch quality control, but they lack natural tissue tropism. Interest has grown, and the FDA has approved many products, including vaccines for cancer and infectious diseases [26].

EVs and liposomes are both nanoparticle delivery systems with lipid bilayers, cargo-carrying capacity, and surface-modification options. EVs have a complex biological makeup with surface and internal molecules, whereas liposomes are a more defined system that is easier to control. These similarities and differences support testing the same ligand approach with both EVs and liposomes to evaluate whether preferential uptake is associated with the targeting ligands, the delivery vehicle, or both.

Nanoparticles Surface Engineering

One exciting and significant area of study in nanoparticles is analyzing and optimizing their therapeutic effects. However, a key challenge is ensuring they efficiently reach and deliver their contents to the intended targets, given their distribution throughout the body. Unmodified or naïve EVs preferentially distribute to the liver, kidneys, lungs, and spleen [27]. Therefore, to improve delivery efficiency to targets beyond these organs, researchers can introduce specific ligands on the EV surface to enhance interactions with target cells [28]. Figure 1.1 illustrates two approaches to EV surface modification: biological and chemical, as reviewed in the next section.

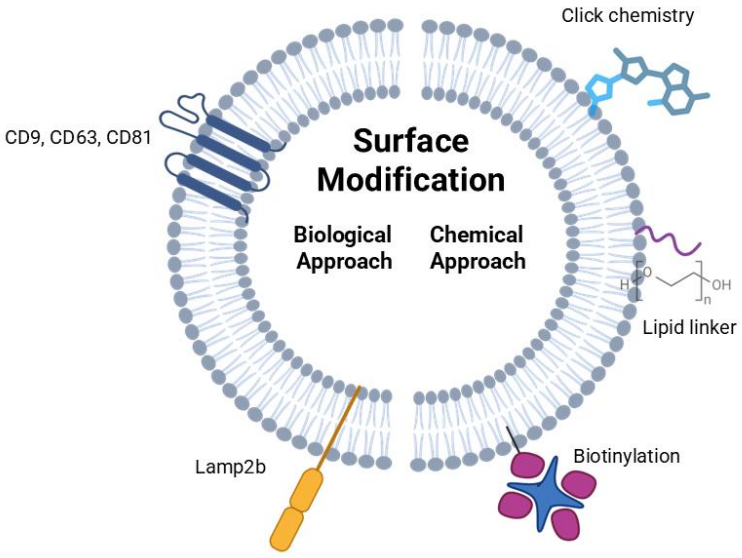


Figure 1.1. Surface Modification of EVs

EV surface modification assumes that ligands can be added to EV membranes to enhance tissue targeting and uptake. This figure illustrates two approaches to surface engineering: biological and chemical. In the biological approach, researchers modify genes for tetraspanins (CD9, CD63, and CD81) or other EV-enriched peptides, such as Lamb2b, in the host cell line to add ligands (peptide sequences), then isolate the modified EVs from the cell culture medium. Alternatively, host cells may be transduced with plasmids (for example, via viral transduction) that overexpress a fusion protein of a tetraspanin and a ligand, and the modified EVs are collected from the culture medium. The primary chemical approaches are chemical crosslinking of targeting ligands to EV membranes or inserting lipid linkers into EVs to incorporate targeting ligands into the EV membrane. (created with BioRender)

Biological Approach--Genetic Engineering

Genetic engineering of EV-producing cells modifies the EV membrane surface (see reviews [29,30]). A popular approach is to engineer changes to proteins found in EV membranes. The two commonly used membrane proteins for genetic engineering are tetraspanins and Lamp2b. The details are provided below.

The first strategy targets tetraspanins, a family of transmembrane proteins. They have been used because some are enriched in EVs [31]. The tetraspanins bearing clusters of differentiation (CD) 9, CD63, and CD81 are commonly found in EVs and, as such, are part of the International Society for Extracellular Vesicles' (ISEV) minimum definition of EVs [32]. These molecules share a similar structure with four transmembrane domains (crossing the membrane four times), and amino acid "tails" are found on the EVs' inner (cytoplasmic) region [33,34]. Two common methods for modifying the cell's tetraspanin genes are 1) adding a fusion protein to the N-terminus or C-terminus of the tetraspanin, or 2) transducing plasmids that overexpress tetraspanins with targeting peptide sequences so cells package them into EVs and enhance binding to tissue targets. This approach is similar to adding a targeting peptide "address" to an EV "envelope". This bioengineering approach has successfully enhanced EV binding and uptake by target cells, and several examples are discussed below.

The examples of targeting tetraspanin genes are as follows. The amino acids are targeted by genetic or chemical modification methods to add targeting motifs to the EV surface (Figure 1.1). For example, to target brain tissue, CD9 was genetically engineered with ApoB by transfection in the Expi293F cell line; after intravenous injection, CD9-ApoB EVs were visualized with an intravital confocal microscope and accumulated more in the brain than naïve EVs in mice [35]. Tetraspanins, especially CD63, are good candidates for genetic engineering because they have the highest expression of the antibody Fc binder, particularly when fused with the Z domain, as shown by their highest fluorescent intensity [36]. As shown in Figure 1.2, CD63 with a red fluorescent protein (RFP) fused in-frame to the outer second loop or green fluorescent protein (GFP) fused in-frame to the C-terminus in mammalian Human Embryonic Kidney cells (HEK cells) [37]. Thus, researchers can track EV trafficking by tagging tetraspanins with fluorescent

fusion proteins. In summary, tetraspanin domains are well documented as promising targets for EV surface engineering applicable to neurotargeting models.

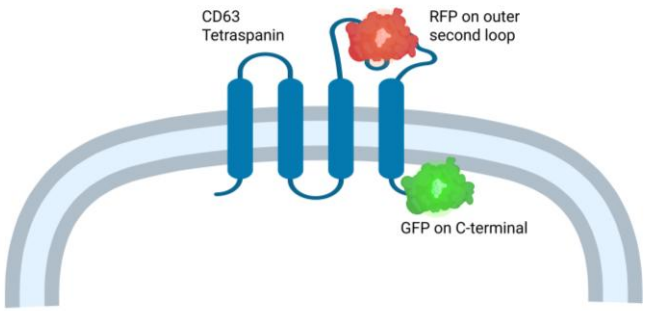


Figure 1.2. Engineering of CD 63 with RFP and GFP
RFP was engineered on the outer second loop, and GFP on the C-terminus. We engineered both RFP and GFP into the CD63 tetraspanin. (adapted from Stickney et al. [37] and created with BioRender)

The second main target is Lamp2b. It is a lysosomal-associated transmembrane protein enriched in EVs and exosomes and has also been used for surface engineering [38]. The most widely studied ligand for targeting neural tissue with EVs is the rabies virus glycoprotein (RVG) peptide. RVG enhances neural uptake by binding to the nicotinic acetylcholine receptor (nAChRs). RVG fused in-frame to Lamp2b has been tested [39,40]. RVG-presenting exosomes demonstrated enhanced neural uptake after IV injection [41]. RVG-Lamp2b-modified EVs successfully targeted neurons in Parkinson's disease [42]. Another study by He et al. demonstrated the specificity of neural uptake by comparing neurons and glial cells (Schwann cells) with endothelial cells [43]. In summary, RVG-Lamp2b-modified EVs are a good example of how surface engineering can enhance tissue specificity.

Lamp2b fusion peptide engineering has also been used to add ligands that direct EV delivery to other cells and tissues. For example, Kim et al. engineered EVs to target heart cells by fusing CTP, a cardiac-specific peptide [44]. Similarly, Kim et al. enhanced the anti-inflammatory action of EVs by adding an in-frame RAGE-binding peptide (RBP) to Lamp2b and tested this construct in an inflammatory lung cell model [45]. Lastly, Liu et al. fused a collagen II-targeting peptide to Lamp2b to target cartilage [46]. In summary, Lamp2b, like tetraspanins, is a viable target for displaying ligands that enhance EV delivery to specific cells or tissues.

While EV surface modification can improve tissue delivery and uptake, Hung and Leonard suggested that not all peptides fused to ligands function efficiently, possibly because proteolytic enzymes degrade them during biogenesis [47]. This concept has been demonstrated for peptides fused to Lamp2b that failed to reach the target in muscle [41]. To address this drawback, one study suggested that glycosylation of the motif could reduce degradation and increase stability, thereby increasing relative peptide expression without hindering cellular interaction [47]. Kim and colleagues (2018) also applied this strategy to the cardiac target peptide (CTP)-Lamp2b [44]. Although they did not compare glycosylation motif engineering with its absence, this method may help CTP-Lamp2b uptake cellular material into target cells.

In addition, this biological approach requires cells to produce EVs, which may pose production, reproducibility, and scaling challenges for clinical testing. To address these limitations, I considered alternative chemical approaches that can modify preformed nanoparticles, including EVs and liposomes. This flexibility also enables investigation of similar surface modifications using fully synthetic nanoparticles, which, for clinical development, would avoid some of the GMP cell manufacturing and EV isolation bottlenecks in clinical translation.

Chemical Approach

In this section, I review chemical methods for adding targeting ligands to EVs and liposome membranes. The three approaches, including lipid-linking, the ABC method, and click chemistry, are described below.

Lipid-linking method

A strategy to modify EV or liposome membranes uses a lipid linker to alter tissue distribution and trafficking. Phosphatidylethanolamine (PE) is a class of phospholipids found in cell membranes [48]. PEs such as DOPE (1,2-Dioleoyl-sn-glycero-3-phosphoethanolamine) and DSPE (1,2-Distearoyl-sn-glycero-3-phosphoethanolamine) are widely used as linkers for lipid nanoparticles to modify nanoparticle surfaces [49]. Both lipids are often PEGylated (PEG: polyethylene glycol), which reduces aggregation and interactions with mononuclear cells, prolongs circulation, and reduces immune clearance [50,51]. PEGylation has been applied to liposomes and lipid-based nanoparticle drugs on the market, such as DOXIL®, Onivyde®, and AmBisome®.

PE-PEGylation is a successful strategy for modifying EV surfaces and has been used to conjugate peptides to EVs. Several studies in the tumor field have used this method to conjugate ligands to EVs [52,53]. ADDIN EN.CITE (54, 70, 71) This method could be used to target neurons. DSPE-PEGylation has been shown to tag the C3 peptide, and triphenylphosphonium (TPP) can target neurons' mitochondria [54]. RVG can be used as a ligand with the DSPE-PEG linker to target neurons in Parkinson's disease [55]. Cui et al. inserted the RVG peptide into the MSC-EVs' surface using DOPE. They showed that EVs could reach the cortex and hippocampus after IV injection in the AD model [40]. Similarly, Vandergriff et al. used EVs decorated with cardiac-derived peptides and DOPE on the surface and showed homing to infarcted heart tissue after IV injection [56]. In

summary, lipid linkers are a useful surface-engineering method, leveraging existing literature on surface modifications applied to lipid nanoparticles.

Zheng and colleagues (2023) used a fluorescent NBD tag on EVs to compare linkers, including ceramide, cholesterol, and DOPE [57]. They reported that DOPE outperformed the others, yielding the highest fluorescence intensity. They also noted that the DOPE anchor appeared to bind firmly to EVs after incubation in media or after freeze/thaw cycles. This linker has been used with the RVG peptide and click chemistry to increase cellular uptake in AchR and neuronal cells [36]. In addition, albumin-EVs with DOPE tagging increased EV plasma half-life [57]. In sum, lipid anchoring is a method for surface engineering EVs and maintaining stability under harsh conditions.

ABC method

The avidin-biotin interaction forms a strong, non-covalent bond, resulting in stable binding [58,59]. Avidin is a glycoprotein with 4 subunits, and biotin is vitamin B7, important for cell signaling and growth promotion [58,59]. This strategy has been applied in molecular contexts and used in nanoparticle conjugation systems.

This system can be used with the lipid-linking method. For example, Deng et al. conjugated DSPE-PEG-biotin in situ to produce EV-DSPE-PEG-biotin for interaction with NHS-PEG-biotin crosslinking, using avidin as a complement for conjugation [59]. Another liposome example uses biotinylated DSPE-PEG in liposomes and combines it with avidin and biotinylated CTB [2]. These studies showed that the biotin-avidin system can bridge ligands and nanoparticles. Beyond nanoparticles, this system is commonly used in immunoassays and has been applied to deliver small molecules, monoclonal antibodies, vaccines, proteins and peptides, and nucleic acids [58].

Click chemistry

Several methods have been used to covalently link ligands to lipid membranes. Click chemistry includes reactions such as Copper-Catalyzed Azide-Alkyne Cycloaddition (CuAAC) (136), which is a fast, simple, high-yielding reaction used for one-step chemical crosslinking. This reaction forms a stable 1,2,3-triazole linkage between an alkyne and an azide. This is the most popular method because it is easy, stable, and efficient [60]. Another advantage is that this method can also be applied to lipid nanoparticles to improve biodistribution and tissue uptake. Another copper-free reaction, e.g., strain-promoted azide–alkyne cycloaddition (SPAAC), avoids potential copper toxicity in biological systems [61].

Several laboratories have demonstrated the effectiveness of these methods for EV surface modification, and the literature is reviewed below. Yan et al. used click chemistry to engineer EVs carrying a mitochondrial-targeting ligand (MTL) specific to brain cell mitochondria [62]. In a mouse model of ischemic stroke, click chemistry linked a cyclopeptide to EVs to target brain tissue, including microglia, astrocytes, and neurons [63]. In a multiple sclerosis model, sialic acid-conjugated EVs, prepared via click chemistry, targeted the CNS, specifically microglia, after intranasal administration [64]. Researchers added a tetanus toxin-C fragment to EVs via click chemistry, enhancing transport to peripheral neurons [65]. Jia et al. showed that conjugating a neuropilin-1-targeting peptide to EVs could target glioma, with success in imaging and therapy [66]. Researchers can incorporate RVG into EVs via click chemistry to target neurons [67].

Few articles have compared surface engineering strategies to explore EVs' morphology, function, and binding activity. One example is Musicò et al., who compared the binding of the antibody Cetuximab (CTX) to its antigen, EGFR, using different chemical conjugation methods, including click chemistry and a non-clickable method (NHS ester conjugation). They found that binding affinity for EGFR did not differ between the two methods, but click chemistry enhanced

cellular uptake in target cells [68]. In summary, click chemistry-based conjugation is promising for engineering surface modifications on EV membranes.

Click chemistry has also successfully facilitated ligand conjugation to liposomes [69,70]. Researchers have proposed using click chemistry to conjugate monoclonal antibodies to liposomes for cancer models [71]. Click chemistry has also been used to attach proteins to liposomes [72]. These support the use of click chemistry in liposomes.

Taken together, chemical approaches, including ABC methods, lipid-linking methods, and click chemistry, have been proposed for surface modification. Importantly, these methods apply to both EVs and liposomes. In this dissertation, I selected the ABC and lipid-linking methods to test conjugation for further evaluation. I chose the ABC method because biotinylated CTB is commercially available and can be coupled to EVs, providing strong affinity for avidin. I also chose the lipid-linking method because EVs and liposomes share a similar composition: a lipid bilayer that allows direct insertion into the membrane. I did not choose click chemistry or assess copper-free conjugation because these approaches require additional steps: adding a reactive group and a reactant. Therefore, I will assess these two practical approaches for surface modification.

Have any ligands been used for neuron targeting?

Many different ligands have been tested on EV surfaces, either on the outside or inside, to serve a targeting purpose: increasing specificity for the tissue of interest. As shown in Figure 1.3, both large and small molecules can modify EVs using biological or chemical means, as discussed above. Examples of ligands that successfully target tissues of interest include aptamers, proteins, peptides, and nanobodies (see Fig. 1.3).

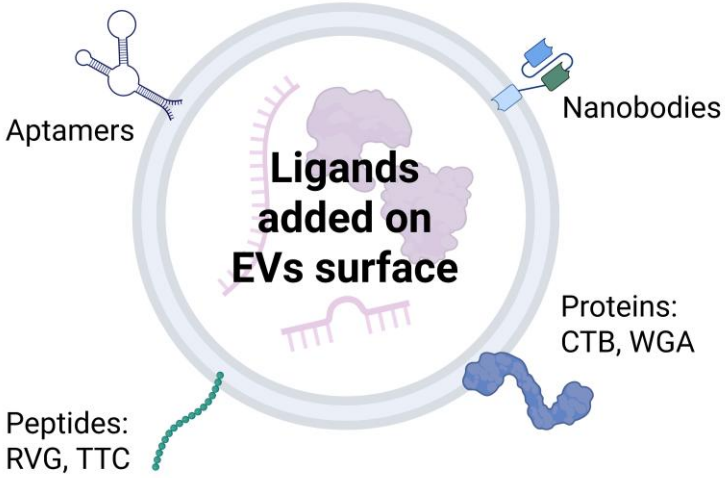


Figure 1.3. Ligands on EVs surface

Different ligands can be decorated on the EV surface, including aptamers, nanobodies, peptides, and proteins (RVG: Rabies Virus Glycoprotein, TTC: tetanus toxin C fragment, CTB: Cholera toxin B, WGA: Wheat germ agglutinin) (created with BioRender).

An aptamer is a short nucleic acid sequence that folds into a 3D structure and functions like an antibody, binding a specific target. Aptamers occur naturally or can be engineered to bind a target [73]. EVs can be tagged with an aptamer [74]. Hosseini et al. decorated EVs with AS1411 aptamers to fight colorectal cancer [75]. Esposito et al. used an RNA aptamer to detect breast cancer EVs, which can aid early diagnosis [76]. Wu and colleagues showed that a nano platform coated with EVs decorated with the aptamer AS1411 could cross the BBB and target glioblastoma [77]. Liang et al. developed EVs decorated with angiopep-2, which can bind to GBM and the BBB due to high expression of receptor-related protein 1, and with a CD133 RNA aptamer to target glioblastoma stem cells in a glioblastoma multiforme model [78]. Hosseini and colleagues developed an aptamer with affinity for myelin, which has both prophylactic and therapeutic effects via inflammatory modulation [79].

In addition to aptamers, nanoparticles can be decorated with peptides and proteins, including Rabies Viral Glycoprotein (RVG), Tetanus Toxin C (TTC), substance P, CTB, and WGA (Table 1). Below, I explain RVG, TTC, and substance P, but not CTB and WGA, which I discussed above.

One of the most attractive is the Rabies Viral Glycoprotein (RVG). RVG is responsible for the neurotropism of the Rabies virus in nature [80]. RVG contains 505 amino acids, and positions 189-214 and 330-357 are important nerve-binding regions, primarily for the nicotinic acetylcholine receptor (nChR) [81]. This peptide is safe and BBB-permeable. It successfully tags synthetic and natural nanocarriers, including liposomes, dendrimers, EVs, polymers, micelles, and bioactive proteins [81]. The first study demonstrated the proof of concept of using RVG to deliver siRNA to neuronal cells in the brain after IV injection [82]. To highlight RVG's utility, researchers have used it to tag polymers to deliver genes to the brain, as shown by in vitro and in vivo analyses [83]. Furthermore, liposomes carrying siRNA target hippocampal and cortical neurons to knock down alpha-synuclein in a mouse cell culture model [84]. In EV research, RVG has helped decorate EVs that fuse with Lamp2b, an exosomal membrane protein, to deliver siRNA to the mouse brain after IV injection to knock down BACE1, a target gene in Alzheimer's disease [41]. Likewise, Cui et al. described using RVG in an Alzheimer’s disease model but used an NHS lipid linker to conjugate RVG to the surface. The results showed specificity for cortex and hippocampus tissue and improved clinical signs [40]. However, no evidence shows that adding the RVG ligand enhances uptake in peripheral sensory systems.

Tetanus toxin, a neurotoxin produced by *Clostridium tetani,* has been used to neurotarget EVs. [85]. It has been used as a neurotrophic factor for neurodegenerative disease to transport retrogradely to the central nervous system [86]. Tet1, a peptide from Tetanus toxin, can act as an

analog of fragment C of tetanus toxin [87]. It has been used as a neurotrophic factor for neurodegenerative disease and can retrograde to the central nervous system [88]. Tet1, a peptide from Tetanus toxin, can act as an analog of fragment C of tetanus toxin [87]. Phage display screening showed it binds primary motor neurons and DRG neurons, but not muscle cells [88]. Because it binds motor neurons, it transports retrogradely to the soma [89]. Several studies demonstrate Tet1's neuronal specificity, including one using Tet1-conjugated liposomes with morphine encapsulation, which showed uptake by DRG [90]. Beyond using a single ligand for neurotargeting, liposomes encapsulated with curcumin and dual Tet1 and transferrin ligands showed neuronal targeting, neuroprotective ability, and alleviated cognitive dysfunction in mouse models [91]. In addition, liposomes encapsulated with curcumin and dual Tet1 and transferrin ligands showed neuronal targeting, neuroprotective ability, and alleviated cognitive dysfunction in mouse models [91]. In addition to the Tet1 ligand, tetanus toxin-c fragment (TTC), a Clostridium neurotoxin, has been successfully added to nanoparticles to enhance binding specifically to the neuroblastoma cell line in vitro [90]. EV surface modification using click chemistry to add TTC can enhance uptake and retrograde transport after IM injection and show specificity for neuronal cells compared with unmodified EVs [65]. No evidence shows that TTC enhances uptake in peripheral sensory systems.

Substance P (SP) is a neuropeptide and a ligand for the neurokinin type 1 receptor (NK1R). This receptor is highly expressed in brain cancer [92]. Ruan et al. showed that SP-decorated albumin nanoparticles can target glioma after intravenous administration [93]. Rangger et al. conjugated SP to liposomes, creating a dual-ligand system with the arginine-glycine-aspartic acid (RGD) peptide to target the neurokinin-1 receptor (NK1R) and αvβ3 integrin receptors, respectively. They demonstrated receptor-associated cellular interactions in vitro but observed low

tumor uptake in their biodistribution study [94]. SP and NGF are both ligands found on the sensory neurons of interest. No evidence shows that they can serve as functional ligands to enhance nanoparticle uptake in peripheral sensory systems.

Table 1.1 Ligand targeting neurons

Ligands	Binding site	References
Rabies viral glycoprotein (RVG)	Nicotinic acetylcholine receptor (nAChR)	[40,41,82,95]
Tetanus toxin-c fragment (TTC)	G1b Ganglioside	[65,90]
Supstance-P	Neurokinin type 1 receptor (NK1R)	[92-94]
Cholera toxin B (CTB)	GM1 ganglioside	[1,14,17,18,96]
Wheat germ agglutinin (WGA)	N-acetylglucosamine (GlcNAc)	[1]

Taken together, researchers have described a list of neuron-targeting ligands. These include aptamers, proteins, peptides, and nanobodies. One of the most extensively studied ligands is RVG. However, much of the current research focuses on brain targeting. Given the limited information on ligands that preferentially target different neuron populations in DRG beyond brain targeting, further studies need to expand this knowledge.

Summary

I aim to target distinct neuronal populations in the DRG after peripheral injection. I break this down into two subaims. First, I chose EVs as carriers and modified their surfaces (CTB or WGA) to assess cellular uptake. Second, I modified liposomes, an alternative carrier to EVs, with the same ligand. To support these aims, this chapter reviews targeting and surface-modification

approaches to demonstrate the feasibility of the engineering method. I also provide a rationale for investigating CTB and WGA ligands on EVs and liposomes across different neural populations in the DRG.

Chapter 2 - CTB and WGA Functionalized Nanoparticles Targeting Neurons in the Dorsal Root Ganglia

Abstract

Dorsal root ganglia (DRG) contain heterogeneous populations of sensory neurons that vary in size and function. Small neurons are enriched in nociceptive populations, whereas medium- to large neurons mainly contribute to mechanosensation and proprioception. Ligand-functionalized nanoparticles (e.g., extracellular vesicles (EVs), liposomes) offer a therapeutic approach to target preferred DRG subpopulations. We hypothesize that wheat germ agglutinin (WGA)-functionalized nanoparticles would preferentially target small neurons in the DRG, whereas Cholera toxin B (CTB) can target medium- to large neurons. We demonstrated two ligand-conjugation methods, ABC (biotin EVs-avidin-biotinylated CTB) and lipid-linking (DOPE-PEG-NHS), in initial in vitro dose-response experiments to show specific uptake of CTB-EVs in a neuronal cell line (ACS 5004). We then used the lipid-linking method for the remaining experiments to test CTB- and WGA-functionalized EVs and liposomes. CTB-liposomes did not show preferential uptake in the neural cell line. WGA-EVs and WGA-liposomes also did not demonstrate preferential uptake in ACS 5004. Subsequently, we conducted in vivo experiments comparing CTB-EVs to EVs and WGA-EVs to EVs, using peripheral injection to assess retrograde transport to DRG and examine size-dependent preferential uptake by subpopulations. The results showed that only CTB-EVs were successfully transported retrogradely to DRG and taken up specifically in medium- to large DRG. In contrast, WGA-EVs were not detected in DRG following peripheral administration and did not show a preference for uptake in small neuronal subpopulations. These findings suggest the importance of considering both ligand selection and

carrier properties when designing targeted nanoparticle delivery systems for peripheral sensory neurons, DRG.

Introduction

Delivering therapeutics to the dorsal root ganglia (DRG) after peripheral administration remains a significant challenge because drugs must overcome multiple biological barriers that limit delivery efficiency and can result in subtherapeutic efficacy or off-target effects [97,98]. Selective delivery of therapeutics to specific DRG neuronal populations could improve treatment strategies for chronic pain and other peripheral nervous system disorders while minimizing systemic exposure and unwanted side effects. This study aims to develop a targeted delivery approach for DRG neurons by functionalizing nanoparticles with ligands that enhance neuronal uptake and retrograde axonal transport after peripheral injection.

DRGs contain a heterogeneous population of sensory neurons that differ in morphology, physiology, axonal conduction properties, and molecular phenotype [8,10]. These neurons include multiple functional subtypes, such as unmyelinated C-fiber peptidergic nociceptors and thinly myelinated, non-peptidergic Aδ-fiber neurons. Although the DRG's anatomical location makes direct injection technically challenging, these neurons' peripheral axons are readily accessible. Molecules or delivery vehicles internalized at peripheral nerve terminals can undergo retrograde axonal transport to neuronal cell bodies within the DRG, providing an attractive route for targeted therapeutic delivery. We hypothesize that this endogenous transport pathway can be exploited to selectively deliver therapeutic cargoes to defined DRG neuronal subpopulations following peripheral administration, e.g., targeting the TrkA+, TRPV1+, peptidergic nociceptor subpopulation.

Nanoparticles, including naturally derived extracellular vesicles (EVs) and synthetic lipid nanoparticles such as liposomes, have emerged as versatile drug delivery platforms because of their biocompatibility, ability to encapsulate diverse therapeutic cargoes, and capacity for surface engineering. EVs function as endogenous mediators of intercellular communication and naturally transport proteins, lipids, and nucleic acids between cells [99]. Although no EV-based therapeutics have yet received FDA approval, several candidates are advancing through clinical development, including a phase III trial investigating EV-based therapy for acute respiratory distress syndrome [100]. In contrast, liposomes have an established clinical record, with multiple FDA-approved formulations used to deliver therapeutics for cancer, infectious diseases, and vaccines [101]. Importantly, both EVs and liposomes can be engineered to modulate their biodistribution and cellular tropism through surface functionalization with targeting ligands or by modifying membrane composition [102].

Surface engineering with neuron-targeting ligands is a promising strategy to enhance neuronal uptake and retrograde transport. Two well-characterized neuronal targeting ligands are cholera toxin B subunit (CTB) and wheat germ agglutinin (WGA). CTB binds with high affinity to the GM1 ganglioside [103], which is enriched on neuronal membranes and internalized primarily via lipid raft-associated, caveolin-dependent endocytosis [104]. Classic neuroanatomical studies showed that CTB conjugated to horseradish peroxidase (CTB-HRP) injected into the sciatic nerve preferentially labels large-diameter DRG neurons and neurons within spinal cord laminae III–V [1], indicating preferential access to myelinated sensory neuron populations rather than small-diameter nociceptors. More recently, Fukui and colleagues demonstrated that CTB-functionalized liposomes with optimized lipid compositions exhibited enhanced retrograde transport to the spinal cord and DRG after sciatic nerve administration compared with untargeted liposomes [2].

In contrast, WGA is a plant lectin that binds N-acetyl-D-glucosamine and N-acetylneuraminic acid residues on neuronal glycoconjugates [105]. WGA is efficiently internalized via receptor-mediated endocytosis, primarily through clathrin-dependent pathways [106]. Following sciatic nerve administration, WGA-HRP preferentially labels small-diameter DRG neurons that terminate in spinal cord laminae I and II, unlike CTB-HRP, suggesting that CTB and WGA access distinct sensory neuronal populations (Figure 2.1) [1]. Because many nociceptors are contained within small-diameter, unmyelinated C-fiber populations, WGA-mediated targeting may offer a strategy to access the target nociceptive sensory neuron population. However, small-diameter neurons are molecularly heterogeneous and include both nociceptive and non-nociceptive sensory populations; therefore, additional characterization is required to determine the extent of nociceptor-specific targeting.

Despite their extensive use as neuronal tracers, the application of CTB- and WGA-functionalized extracellular vesicles or liposomes for retrograde transport from peripheral tissues to the DRG has not been extensively investigated. To address this gap, we developed CTB- and WGA-functionalized extracellular vesicles and liposomes using two membrane-conjugation strategies. We evaluated their uptake in vitro and in vivo after peripheral footpad injection in rats, compared with unmodified nanoparticles. Based on the established neuronal tropism of CTB and WGA, we hypothesized that CTB-functionalized nanoparticles would preferentially target medium- and large-diameter DRG neurons. In contrast, WGA-functionalized nanoparticles would preferentially target small-diameter DRG neurons enriched for nociceptive populations. This approach may provide a platform for targeted delivery of therapeutic cargoes to defined sensory neuronal populations and improve the efficacy and specificity of nanoparticle-based therapies for peripheral nervous system disorders.

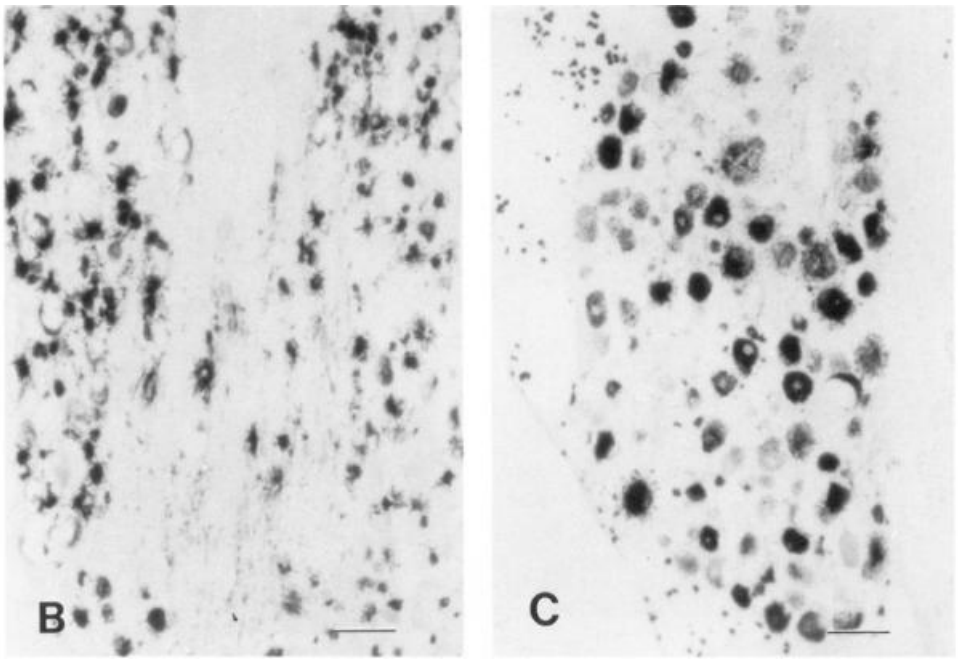


Figure 2.1. Labeling of neurons in DRG after WGA-HRP or CTB-HRP injection. WGA-HRP injection predominantly labels small-diameter DRG neurons (left), while CTB-HRP injection predominantly labels large-diameter DRG neurons (right) [1].

Materials and Methods

EVs Isolation

The Midwest Stem Cell Therapy Center at the University of Kansas Medical Center (RS) kindly provided human umbilical cord mesenchymal stromal cell-conditioned media (MSC-CM). The cells were grown in three-dimensional suspension culture on microcarriers in a 2 L bioreactor, as described here [107]. The plating density was 4,500 cells/ cm^2. The expansion media consisted of 500 mL of MSC NutriStem® XF Basal Medium (Sartorius, 05-200-1A) supplemented with 3 mL of MSC NutriStem XF Supplement (Sartorius, 05-201-1U) and 27 mL of PLTGold® Clinical Grade (GMP) (Mill Creek Life Science, PLTGold27GMP). Approximately 5×10^9 cells yielded 2 liters of conditioned medium (CM), collected at passage 3 after 144 hours of conditioning and stored in frozen aliquots until processing.

EVs were isolated from the CM by a combination of ultrafiltration (UF) and size-exclusion chromatography (SEC) as described by Wright et al. [108], with or without tangential flow filtration (TFF) as described below. CM was thawed overnight at 4 °C and centrifuged at 3000 x g for 30 minutes at 4 °C in a benchtop centrifuge (Eppendorf 5810R) to remove cell debris. The supernatant was then filtered through a 0.22 μm sterile filter and centrifuged with a 100 kDa cutoff centrifugal filter (Amicon Ultra–15, UFC910024) for 30 minutes at 3000 x g and 4 °C. The filter was loaded with additional CM, and centrifugation was repeated until the CM volume was reduced to approximately 1/10 of the starting volume, yielding concentrated CM. The concentrated CM was then processed by SEC with a 70 nm qEV column (Izon) using either qEV original (loading 500 μL and collecting 4 fractions of 0.5 mL after 2.7 mL of void volume) or qEV10 (loading 10 mL and collecting 4 fractions of 5 mL after 21.4 mL of void volume) using an automatic fraction collector (Izon, AFC-V1) per the manufacturer's instructions. The collected fractions containing EVs were pooled and concentrated using an Amicon Ultra–15 ultrafiltration device to obtain approximately 1/100 of the CM starting volume. If TFF was performed, it was conducted after filtration through a 0.22 μm sterile filter and before UF and SEC. Using TFF, the CM was concentrated using a 300-kDa cutoff Pellicon XL Cassette (surface area 50 cm^2, Ultracel 300 kDa, Millipore, PXC300C50) to obtain the retentate, yielding about a 12-fold concentration. EV samples were stored at 4 °C for up to 1 week or at -80 °C for long-term storage.

Liposomes manufacturing

Liposomes were prepared by thin-film hydration, followed by freeze-thaw cycles and extrusion, as described by Zhang et al., with some modifications. [109]. In short, we prepared liposomes from a mixture of 20% cholesterol (Sigma-Aldrich, Cat. No. c8667) in DPPC (1,2-dipalmitoyl-sn-glycero-3-phosphocholine, or 16:0 PC, DPPC, Avanti, Cat. No. 850355C). We

formed a thin film by rotary evaporation, then hydrated and vortexed it to form liposomes. The lipid mixture was then subjected to 10 freeze-thaw cycles between liquid nitrogen and a 55 °C water bath, followed by 10 extrusion cycles through a polycarbonate membrane with a 100 nm pore diameter (SPI Supplies, E0125-MB) at 50 °C for heat setting. The liposome fraction was collected by chromatography on a Sephadex G-50 column with a molecular weight cutoff of 30 kDa.

Characterization of EVs and liposomes

We used ISEV methods to characterize the nanoparticles [32]. We measured hydrodynamic size distribution (polydispersity index) and surface charge by dynamic light scattering (DLS) and zeta potential (ZP) using a Zetasizer Nano ZS, following the manufacturer's protocols (Malvern Instruments, Ltd.). The samples were run for 30 seconds, 3 times/ sample. The nanoparticle size and concentration were measured by Nanoparticle Tracking Analysis (NTA) using a NanoSight LM-10 (Malvern Instruments, Ltd.) with NTA 3.3 software, a CMOS camera, and a blue 405 laser, using the manufacturer's protocols, as described below. Briefly, samples were diluted in DPBS (Gibco, 14190-144), filtered through a 30-nm filter, and yielded approximately 100 particles per field. We averaged the NTA data from 5 videos, each a 30-second capture at camera levels 10-13 and a detection threshold of 5, at a constant temperature of 25 °C. We characterized size and morphology using transmission electron microscopy (TEM, University of Kansas Medical Center), as previously described [108]. The nanoparticle sample was placed on a carbon film-coated 400-mesh copper grid (Electron Microscopy Sciences, CF400-CU-50), air-dried, and counterstained with 2% uranyl acetate (Electron Microscopy Sciences, 22400). Images were collected from randomly selected fields using a Hitachi H-8100 TEM at an accelerating voltage of 200 kV. TEM images were collected at at least 10,000× magnification from at least 5 randomly

selected fields, each comprising approximately 2.1-54 μm^2. We generated size means and representative images for each sample.

Protein quantitation and analysis

Protein characterization was performed using a western blot, per ISEV specifications [32]. First, protein concentrations were measured with a Pierce bicinchoninic acid (BCA) protein assay kit (Thermo Scientific, 23235) or with a micro BCA protein assay (Thermo Scientific, 23235) according to the manufacturer's instructions. The kit included bovine serum albumin to construct the standard curve. We measured absorbance at 562 nm with a BioTek Synergy H1 Hybrid reader. We calculated protein concentration using the standard curve, subtracting the albumin concentration from the blank solution. Samples were plated in duplicate or triplicate in a 96-well plate (Corning, 9017). The SDS-PAGE protocol is in the supplemental section. Next, samples were lysed with RIPA lysis buffer (Millipore, 20-188), treated with a protease and phosphatase inhibitor cocktail (Sigma-Aldrich, PPC1010), and incubated on ice for 15 minutes. For western blotting, 3-30 µg of protein was loaded per lane, and the protocol of Sule et al. was followed [110]. The detailed procedure is in the appendix. section.

Modification of EVs and liposomes with CTB or WGA

we added avidin (Sigma Aldrich, A9275) and biotinylated CTB (Sigma Aldrich, C9972) od and a lipid-linking method. To functionalize using the ABC method, we followed the protocol outlined in by Fukui et al. [2] with modifications. Briefly, EVs were biotinylated with Sulfo-NHS-LC-LC-Biotin (Thermo Scientific, 21338) using a molar addition calculated according to the manufacturer's protocol. Next, excess unbound biotin was removed by desalting (Thermo Scientific, 89892) or by ultrafiltration (Amicon filter with 100 kDa cutoff). To functionalize EVs,

avidin (Sigma Aldrich, A9275) and biotinylated CTB (Sigma Aldrich, C9972) were added at a molar ratio of biotinylated EVs: avidin: biotinylated CTB of 1:1.8:1.

To add CTB or WGA using the lipid-linker method, we followed the protocol described by Hu et al., with modifications [111]. Briefly, we reacted EVs or liposomes with DOPE-PEG 5000-NHS (Nanoc, PG2-DONS-5K), a linker conjugated to either CTB (Sigma-Aldrich, C9903) or WGA (Sigma-Aldrich, L9640). The lipid linker: ligand ratio was 1:1.5 (DOPE-PEG 5000-NHS: CTB or WGA) in 1 mL of PBS (Gibco, 20012-027) at room temperature overnight. Then, the unreacted DOPE was removed from DOPE-CTB or DOPE-WGA (DOPE-ligand) by ultrafiltration using a 10 kDa filter cutoff, and the retentate was collected. To complete the linkage, EVs or liposomes (10^{13} nanoparticles) were added at a ratio of 6,000:1 DOPE-ligand to particles (EV or lipid nanoparticles), and the mixture was incubated at 37 °C for 1 hour.. Extrusion was subsequently performed for 10 cycles using a polycarbonate membrane with a 1,000-nm pore size (Sterlitech, 1270092). We then collected CTB- or WGA-nanoparticles as the retentate via ultrafiltration using a 100-kDa filter cutoff. Further details are in the supplemental section.

Quantitative analysis of ligand tagging to EVs

CTB-EVs prepared by both ABC and lipid-linking methods were quantified using indirect ELISA to estimate the ligand concentration per EV. First, a standard curve of native protein was established by checkerboard titration with 2-fold dilutions of protein starting at 1 mg/mL in PBS, 100 µL/well, coated onto a clear, flat-bottom, 96-well immune plate (Thermo Scientific, 44204) at 4°C overnight. The next day, add a blocking buffer with 3% Bovine Serum Albumin (BSA, Sigma-Aldrich, A3912) in PBS-T and incubate for 1 hour at room temperature. Then, add primary goat anti-cholera toxin B subunit pAb (Sigma-Aldrich, 227040) at 1:1,000 in PBS. Rabbit anti-goat IgG antibody labeled with horseradish peroxidase (HRP, Sigma-Aldrich, AP106) was used

as the secondary antibody at 1:5000 in PBS. PBS-T 0.05% was used to wash 3 times between steps before adding the solution. Tetramethyl benzidine substrate (Sigma-Aldrich, T0440) was incubated in the dark for 10 minutes, then 1 M H_2SO_4 was added to stop the reaction. The OD value at 450 nm was read with a BioTek Synergy H1 Hybrid reader. Second, after establishing the standard curve, CTB-EV samples diluted in PBS with known particle concentrations were analyzed, and their concentrations were calculated using the standard curve. Triplicate samples were averaged for analysis.

PKH 26 Staining of EVs and liposomes

PKH26 red fluorescent dye (Sigma, PKH26GL-1KT) was used for labeling EVs or liposomes according to the manufacturer's protocol. In short, concentrated nanoparticles in 0.25 mL were mixed with diluent C 0.25 mL, then 1.5 µL of PKH26 was added, gently mixed, and left to stand at room temperature for 5 minutes. The excess dye was removed by adding 0.5 mL of 1% BSA. The solution was washed and rinsed with PBS 3 times using an Amicon Ultra with a 100 kDa cut-off to obtain the PKH26-labeled nanoparticles.

Cell culture

Human Neural Progenitor Cells (ACS 5004, ATCC, BYS012) and human embryonic kidney cells (HEK 293, ATCC, CRL 1573) were obtained from ATCC and grown at 37 °C in an HEPA-filtered incubator with 90% humidity and 5% CO_2 (Nuaire 5690). ACS 5004 was cultured per the manufacturer's instructions in KnockOut™ DMEM/ F-12 (Gibco, 12660012) supplemented with 2% StemPro Neural Supplement (Gibco, 1050801), 1% GlutaMax™ Supplement (Gibco, 35050-061), 1% Antibiotic-Antimycotic (AA, Gibco, 15240062) containing bFGF (PHG0024) 20 ng/ ml, and PDGF-AA (10 ng/ ml) on a plate coated with cell basement membrane (ATCC, ACS-3035). HEK 293 cells were cultured in DMEM (ATCC, 30-2002)

supplemented with 10% FBS (ATCC, 30-2021) and 1% Antibiotic-Antimycotic. The seeding density will be detailed in the following sections.

MTT assay

ACS 5004 cells were grown in Neurobasal medium without phenol red (Gibco, 12348017) with 2% B-27 supplement (50X) (Gibco, 17504-044) and 1% AA. HEK 293 cells were cultured in DMEM without phenol red (Gibco, 21063029) containing 10% FBS (ATCC, 30-2021) and 1% AA. We seeded both ACS 5004 and HEK 293 cells at 10,000 cells/cm^2 in a 96-well plate. After reaching ~70-80% confluence, the media were removed, the cells were washed with DPBS containing calcium and magnesium (Gibco, 14040133), and fresh media (DMEM without FBS for HEK 293) containing a known particle concentration (0, 6.25, 31.25, 156.25, and 781.25 pM) was added to each well. The plate was returned to the incubator. The cells were incubated for 24 hours. Next, replace the medium with phenol red-free medium containing 12 mM MTT solution. After 4 hours of incubation, add 10% SDS in 0.01 M HCl to each well, then incubate for another 4 hours. Measure the MTT assay absorbance at 570 nm using a BioTek Synergy H1 Hybrid reader. MTT assay results were averaged from technical triplicates.

In Vitro uptake analysis

ACS 5004 and HEK 293 cells were seeded at 40,000 cells/cm^2 and 20,000 cells/cm^2, respectively. On a U-slide 8-well (IBIDI, 80826), cells were cultured at 37 °C, 5% CO2 until reaching ~70-80% confluence. The media was removed, the plate was washed with DPBS containing Calcium and Magnesium, and fresh media without FBS containing a known concentration of nanoparticles was added. The plate was returned to the incubator for 24 hours. After 24 hours of incubation, the medium was removed, and the plate was fixed with 4% freshly prepared paraformaldehyde in 50 mM phosphate-buffered saline (PFA) for 15 minutes at room

temperature, followed by 3 rinses with DPBS for 5 minutes each. The cells were permeabilized by adding 0.3% Triton X-100 (PBS-TX) in PBS at room temperature for 10 minutes, followed by 3 rinses with DPBS for 5 minutes each. Next, phalloidin counterstaining (CF 488A, Biotium, 00042-T) was performed by incubating cells for 20 minutes at room temperature, then rinsing 3 times with DPBS for 5 minutes each. Then, DAPI (1 µg/ml; Thermo Scientific, 62248) or NucBlue Fixed Cell ReadyProbe reagent (DAPI) (Invitrogen, R37606) was added and incubated for 3 minutes to stain the nuclei. After rinsing with DPBS, the slides were coverslipped with a #1 coverslip using EverBrite™ mounting medium (Biotium, 23001). The slides were stored in a lightproof box at 4 °C until confocal microscopy analysis (Zeiss LSM 880 Airy scan). We plated each treatment in triplicate and imaged with a 40x objective (Zeiss Neofluor, 1.3 NA). We randomly selected six non-overlapping fields (approximately 69.64 x 69.69 μm^2 sampled per treatment). After setting the imaging parameters, we processed the stored images offline using the Zen application to calculate the fluorescent intensity ratio of the positive signal to DAPI.

Loading fluorescent proteins into EVs

We loaded fluorescent proteins into EVs by 1-hour room-temperature incubation, 1-hour incubation at 37 °C, or sonication followed by 1-hour room-temperature incubation. We used enhanced GFP (Origene, TP790050, >0.05 µg/µl) to label either CTB-EVs or WGA-EVs, and mCherry (Origene, TP790040, >0.1 µg/µl) to label naïve EVs. Briefly, 10^{13} particles were mixed with 250 µg of fluorescent protein in a 2.5 mL solution. For sonication, we sonicated the tubes on a Sonics VCX-130 at 130 W and 20 kHz, with 6 cycles of 4 seconds on/2 seconds off, twice, followed by a 2-minute incubation on ice between cycles, then incubation at 37 °C for 1 hour. The free fluorescent dye was removed by ultrafiltration using an Amicon centrifugal unit with a 100-kDa cutoff, and the retentate containing fluorescent nanoparticles (either eGFP-EVs or mCherry-

EVs) was collected and stored until use. We confirmed successful loading of fluorescent protein into EVs by fluorescence imaging (Azure Biosystems, Azure 600) or western blot analysis. We then labeled the eGFP-EVs with either CTB or WGA.

The experiment to determine the location of fluorescent protein after loading into EVs, e.g., on the outside surface of the membrane or inside the EV, different treatments were perform: (1) negative control (no treatment), (2) the sample added with proteinase K (PK) 0.05 µg/µL in 2.5 mM $CaCl_2$ for treatment at 37°C for 1 hour followed by stopping the reaction with a proteinase inhibitor (PI), (3) the sample was added with 3% Triton X-100 (TX) on ice for 15 minutes followed by PK and PI, (4) the sample with PK, PI, and followed by TX. After the treatments, SDS-PAGE and a western blot were performed to confirm whether the protein was loaded into particles (as suggested by [110]).

In Vivo Assay

Animals and procedures

The animal protocol was reviewed and approved by the Kansas State University Institutional Animal Care and Use Committee (reference number IACUC-4916). A total of 16 male Fisher 344 rats, aged 8-10 weeks, from Charles River were used. Samples of mCherry-EVs, eGFP-CTB-EVs, or eGFP-WGA-EVs were prepared at 5 x 10^{10} particles/30 µL/injection site. In one experiment, 5 animals were used to compare eGFP-CTB-EVs and mCherry-EVs, and 1 animal served as a negative control (no treatment). In another experiment, 5 animals were used to compare eGFP-WGA-EVs and mCherry-EVs, and 1 animal served as a negative control. To inject the animals, they were anesthetized with 3% isoflurane in oxygen for restraint. The left hind paw of anesthetized rats was injected between the metatarsal pads with either eGFP-CTB-EVs or eGFP-WGA-EVs, and the right hind paw was injected with mCherry-EVs. To prepare the injection, the

paw surface was cleaned with 70% ethanol, then sterile saline on a 2x2 gauze pad. A Hamilton 100 or 250 µL syringe fitted with a 27 g needle was preloaded with EV solution (or PBS), inserted into the paw, and the 30 µL injection was slowly infused over 15 s. After delivering the full volume, the needle was left in place for about 10 s before being slowly removed. The injection site was wiped again with a clean gauze pad. For the negative control group, 30 µl of PBS was injected into the left hind paw, and the needle was inserted into the right hind paw, but no injection was made. Hind paw thickness was measured with calipers, and flexion responses to von Frey filament #15 were recorded in triplicate on the morning before the injection and at 0, 3, 6, 24, 48, 172, and 168 hours after injection. On day 7, animals were euthanized by exsanguination followed by transcardial perfusion. Briefly, animals were anesthetized with 5% isoflurane in oxygen, placed on a perfusion tray, and their abdomens and thoraxes were opened. The heart was identified, and a blunted 15 ga needle was inserted through the apex into the aorta, and the right atrium was removed. Heparinized 0.15 M saline was infused at 60-100 mL/minute using a peristaltic pump for 3-5 minutes to clear the blood. Then, the pump was turned off, and the solution was switched to 4% buffered paraformaldehyde (PFA), and 500 mL was infused over 30 minutes. Approximately 4 hours after fixation with 4% PFA, the heart, lungs, liver, spleen, kidneys, left and right feet, left and right sciatic nerves, left and right popliteal lymph nodes, and left and right lumbar (L3-L5) DRG were collected for further evaluation. In another experiment, four rats were anesthetized with isoflurane as described above, and on day 0, 5 µL of 2% Fluoro-gold (FG) in water (Biotium, 80023) was injected into the left and right hind paws. Two animals were anesthetized and euthanized on day 5, and another 2 animals were processed on day 7 using the protocol described above. The lumbar (L3-L5) DRGs were cryoprotected in 20% sucrose until

equilibrated, and cryostat sections were collected onto gelatin-subbed slides. DRGs were cryostat sectioned at 12-µm thickness.

Imaging

To compare the biodistribution of functionalized nanoparticles, e.g., eGFP-CTB-EVs, mCherry-EVs, and eGFP-WGA-EVs, tissues including heart, lungs, liver, spleen, kidneys, left and right feet, left and right sciatic nerves, and left and right popliteal lymph nodes were evaluated in situ and ex vivo using an IVIS optical imager (IVIS Lumina II). The exposure time was 30 seconds. To detect distributed nanoparticles, we used 465/eGFP for eGFP-CTB-EVs or eGFP-WGA-EVs and 535/DsRed for mCherry-EVs. One control animal was used to subtract the background from the total radiant efficiency calculation.

Histology

After fixing with 4% PFA, organs were washed 3 times with PBS for 10 minutes each. Then DRGs were placed in 20% sucrose at 4 °C until they equilibrated. The other organs were placed in 15% sucrose at 4 °C overnight or until they equilibrated, followed by 30% sucrose at 4 °C overnight or until they sank. For cryosectioning, the tissues were embedded in Optimum Cutting Medium (Sakura, 4583) and stored at -80 °C until sectioning, which was performed on a Leica CM3050S cryostat at -22 °C. All tissues were collected onto Superfrost Plus glass slides (Fisherbrand, 22-037-246) and dried at 37 °C for at least 2 hours. After drying, we stored the slides at -20 °C until downstream processing.

For comparison in the FG experiment, DRG were collected, dried, cleared in xylenes, and coverslipped with #1 coverglass (Fisher brand, 12-544E) using non-fluorescent mounting medium. The EVOS fluorescent microscope was used to image FG uptake in DRG using the UV channel.

Immunofluorescence staining

For immunofluorescence staining to compare retrograde transport of eGFP-CTB-EVs, mCherry-EVs, and eGFP-WGA-EVs, organs, including L3-L5 DRG on both sides, were processed. We adapted the protocol from Im et al., and details are provided in the supplemental methods [112]. Briefly, tissues were stained on-slide and in situ by immersion first in a PBS with 0.05% Tween (PBS-T) rinse, a blocking solution made of 5% non-immunized serum from the species of the secondary antibody, followed by primary antibody staining overnight at 4°C, then triple rinsed with PBS-T, secondary antibody to amplify the primary antibody signal, and a final triple rinse with PBS-T. In some cases, we stained nuclei with DAPI. The stained slides were coverslipped with a #1.5 coverslip using Prolong™ Glass Antifade Mountant (Invitrogen, P36964). The slides were stored in a lightproof box at room temperature, left to set for at least 48 hours, and then observed by confocal microscopy (Zeiss LSM 880) with a 40x objective (Zeiss Neofluor, 1.3 NA). We randomly selected six non-overlapping fields (approximately 212.55 x 212.55 μm^2 sampled per treatment). After setting the imaging parameters, we processed the stored images offline using ImageJ (Fiji).

Data analysis

For in vitro experiments, we used the fluorescence intensity ratio of signal to DAPI, quantified in Zen software for confocal microscopy. FIJI (ImageJ, [113]) was used for data analysis for in vivo experiments. We quantified the FG experiment by counting positive cells and reporting the percentage of positive cells among all cells. For EV or lipid nanoparticle uptake analysis, particle numbers were evaluated using the TrackMate plugin [114]. We defined the cutoff between small and medium-to-large neurons based on the neuron's cross-sectional area. Neurons with an area less than 600 μm^2 were considered small, and those with an area of 600 μm2 or greater were

considered medium-to-large [115]. Particle counts were validated and reported as positive-signal EVs per 100 μm^2 of neuronal area. Statistical analysis was performed using R software versions 4.3.3 and 4.6.1 [116,117]. Artificial intelligence (GenAI) was used in this paper to assist with the R scripts, including ChatGPT and Gemini 4. The authors reviewed and edited all AI-assisted output and took full responsibility for the content of this publication.

Results

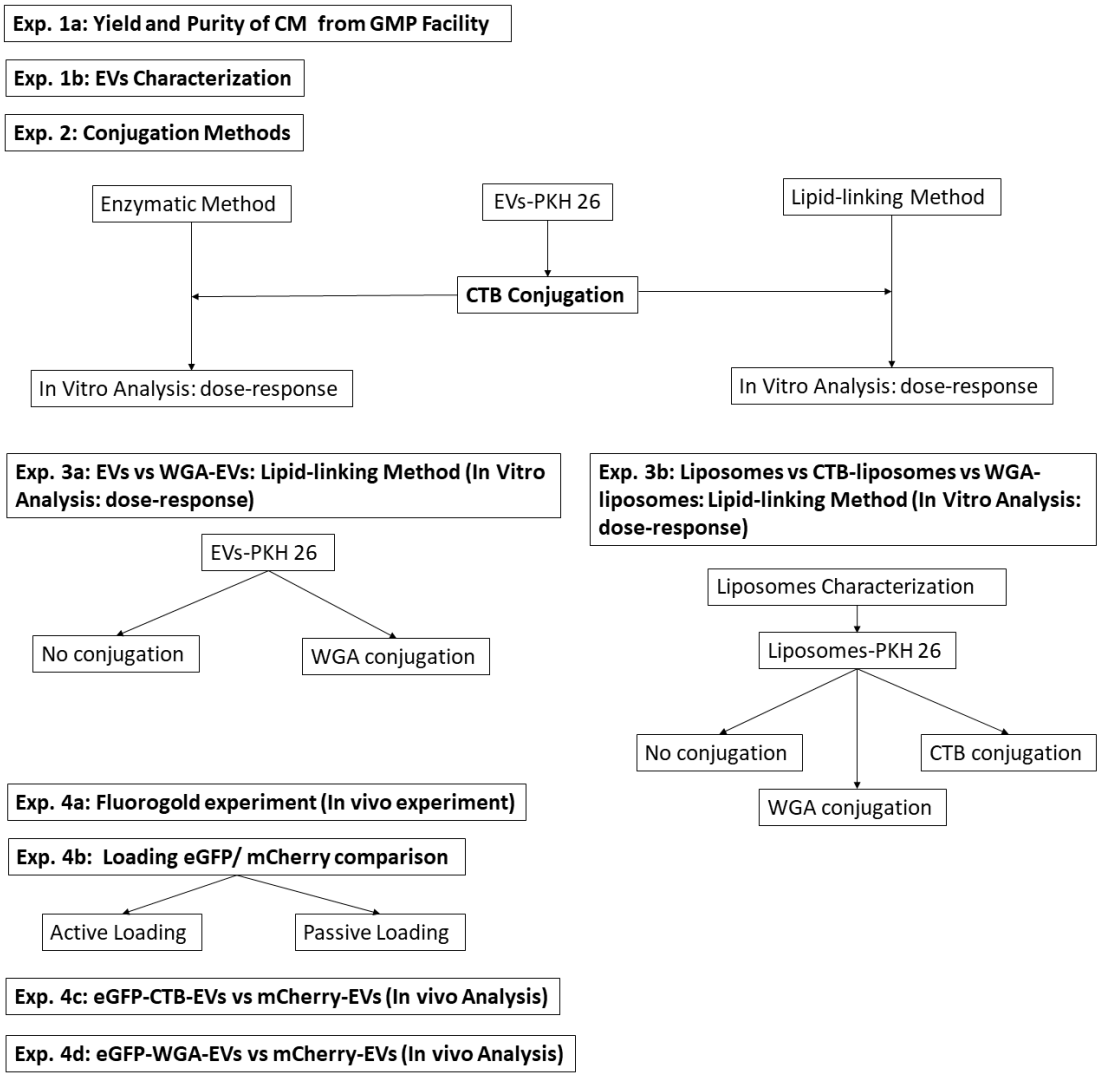


Figure 2.2. Experimental Schematic: We isolated extracellular vesicles (EVs) from human mesenchymal stromal cell conditioned medium (MSCs-CM) using either tangential flow filtration (TFF) and size exclusion chromatography (SEC) or SEC alone. Liposomes were prepared by thin-

film hydration. We compared the efficiency of the two conjugation methods for attaching CTB to EVs by in vitro uptake. We compared CTB- and WGA-conjugated EVs and liposomes in vitro. Next, fluorogold injection experiments were performed, followed by comparison of loading with either eGFP or mCherry. To determine fluorescence Localization, CTB-EVs were compared with EVs, and WGA-EVs were compared with EVs, to assess uptake after injection into the hind footpad of rats.

Experimental Overview

Experimental procedures for EVs and liposomes are shown in Fig. 2.5. Exp. 1a: EVs were isolated from batches of conditioned medium (CM) received from the Good Manufacturing Practice (GMP) facility producing mesenchymal stromal cells (MSCs), and we compared yield and purity. Isolation was performed by Size Exclusion Chromatography (SEC) or by Tangential Flow Filtration (TFF) followed by SEC, followed by characterization (exp. 1b). In the second experiment, EVs were labeled with PKH26, and cholera toxin B subunit (CTB) was conjugated using either an ABC method or a lipid-linking method to compare conjugation efficiency and cellular uptake between the two methods. In the third experiment, we used the lipid-linking method to compare cellular uptake of EVs (experiment 3a) and liposomes (experiment 3b), prepared by the thin-film method and conjugated with either CTB or wheat germ agglutinin (WGA). Experiment 4a compared Fluorogold labeling in the dorsal root ganglia (DRG) on days 5 and 7 post-administration in rats, followed by experiment 4b, which compared loading of fluorescent protein into EVs between eGFP and mCherry. In experiments 4c and 4d, 4c compared uptake of eGFP-CTB-EVs and mCherry-EVs in vivo, and 4d compared uptake of eGFP-WGA-EVs and mCherry-EVs in vivo.

Exp 1. Yield and Purity Analysis of EV Production from Mesenchymal Stromal Cells Conditioned Media (MSCs-CM) derived from Good Manufacturing Practice (GMP) MSC production runs

Three batches of MSC CM from MSC GMP production runs were supplied by the Midwest Stem Cell Therapy Center at the University of Kansas Medical Center (RS, director). In all cases, the MSCs were expanded in NutriStem XF medium supplemented with 5% human platelet lysate in a 3D stirred-tank bioreactor with microparticles in suspension, and the MSCs conditioned the medium for 6 days. We collected CM during the 500 x 10^6 MSC target expansion stage. Each batch was provided in frozen 50 mL aliquots. The 3 batches were used to isolate EVs from CM 7 separate times, including batch 1: Isolation A and B; batch 2: Isolation A; and batch 3: Isolation A-D, with each isolation ranging from 225 mL to 800 mL of CM. Yield of EVs from the 7 isolations is shown in Figure 2.6a. A regression analysis showed a statistically significant positive linear relationship between CM volume and total EV particle yield (R^2 = 0.75, y=6.94 × 10^{10}x - 1.26 x 10^{13}, x = CM (mL) and y = EV particle yield, Fig. 2.6a). EV particle yield per 1 mL CM had a mean of 3.71 × 10^{10} ± 1.98 × 10^{10} (mean ± SD, n = 7) and a median of 3.87 × 10^{10} based on NTA measurements of fresh samples (fig 2.6b). Approximately 5 × 10^9 cells yielded 2 L of CM (equivalent to 2.5 × 10^6 cells per 1 mL of CM). By back-calculation estimate, a mean yield of 3.71 × 10^{10} ± 1.98 × 10^{10} EV particles per 1 mL of CM and approximately 1.48 x 10^4 ± 7.92 × 10^3 particles were released from 1 MSC.

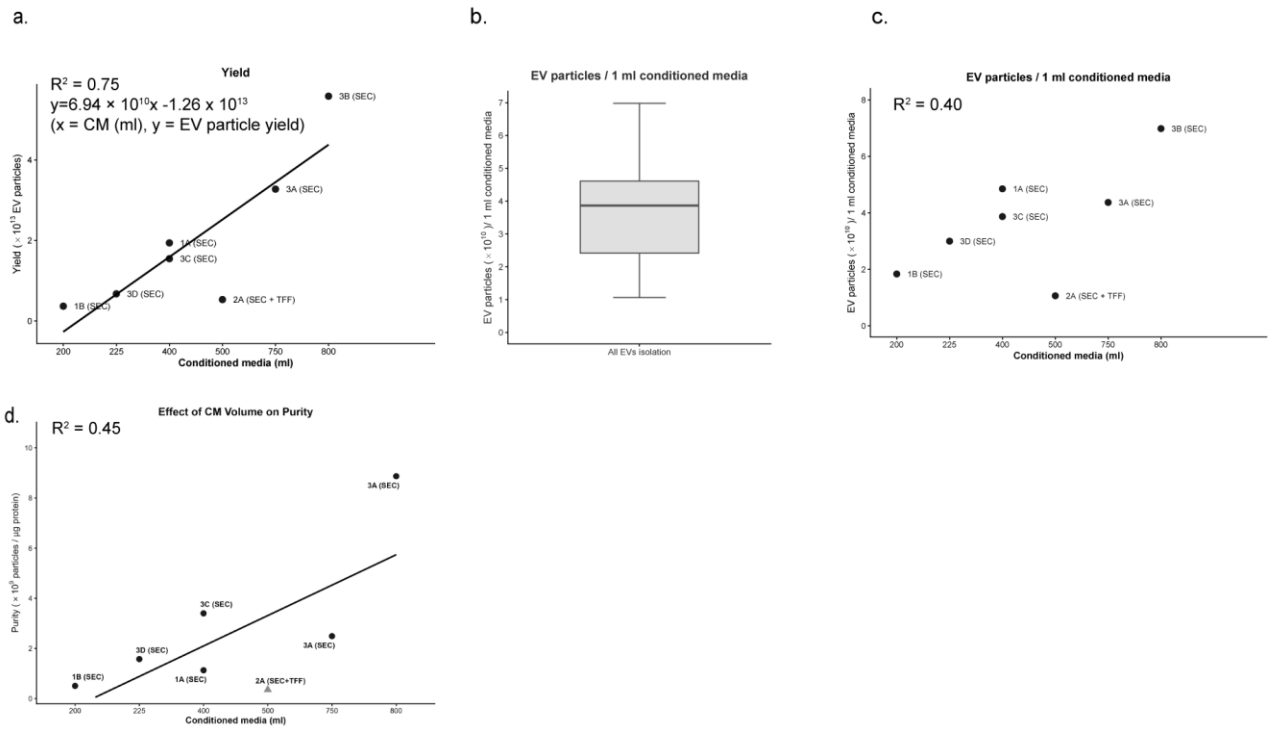


Figure 2.3. Yield and Purity Analysis of EV Production from CM. (a) Yield (total EV particles for each CM isolation) and regression analysis showed a positive correlation between CM (mL) and yield (CM volume as the x variable, p=0.01). (b) EV particles per 1 mL of CM. mean = 3.71 x 10^{10} ± 1.98 x 10^{10} EV particle per 1 mL of CM, median = 3.87 x 10^{10} EV particle per 1 mL of CM. (c) EV particles per 1 mL of CM based on each isolation (CM (mL)). (d) Purity (EV particles/ ug protein). The yield and purity of EVs isolated from CM were not impacted by batch effects or isolation method

To determine whether the CM starting volume affected EV yield efficiency, we performed a regression analysis between EV particle yield per 1 mL of CM and CM volume (Fig. 2.6c). No significant relationship emerged, suggesting isolation efficiency remained constant across starting CM volumes and the three batches of CM received from KUMC. This suggested that using MSC CM from GMP MSC production, coupled with SEC and TFF/SEC isolation, was scalable and predictive of EV particle yield with the specified equipment.

Next, purity analysis was performed. We defined EV purity as EV particles per µg of protein (using BCA or micro BCA to determine protein concentration). We found the purity of EVs isolated from CM to range approximately as follows: for batch 1, 5.06 x 10^8–1.13 x 10^9 particles/µg for two isolation runs; for batch 2, 3.53 × 10^8 particles/µg for one isolation run; and for batch 3, 1.58 x 10^9–8.87 x 10^9 particles/µg for four isolation runs. The average purity of all seven runs was 2.62 x 10^9 particles per µg protein. We had too few samples to make statistical comparisons of purity between batches or EV isolation methods. Next, we evaluated whether starting CM volume affected EV purity. As shown in Fig. 2.6d, the data suggest that starting CM volume did not affect EV purity (R^2 = 0.45). This suggests that starting volume did not grossly affect EV purity. EV yield and purity from CM were not grossly affected by batch effects or isolation method.

Exp 1b. EVs Characterization

Naïve EVs, i.e., EVs isolated straight away from CM samples, were characterized using Western blotting, Nanoparticle Tracking Analysis (NTA), Transmission Electron Microscopy (TEM), Polydispersity Index (PDI), Zeta Potential (ZP), ELISA, and protein concentration, as outlined in the ISEV consortium MISEV characterization guidelines [32]. Appendix Tables B1 and Fig. B. 1a-c, l-n, and B. 2a-e show representative results for nanoparticle size and concentration from NTA, DLS data for size, PDI, and ZP, and TEM. Western blot data confirmed that EVs isolated from CM were positive for EV-relevant proteins (CD9, CD63, and CD81), as shown in Fig. 2.7a. These results support the contention that the EVs isolated are similar to those isolated from 2D MSC expansion, as we previously described [118], and to those isolated from 3D MSC expansion as reported by others [119].

Exp 2. Comparison of EV conjugation methods

We modified the EV surface by conjugating CTB using two methods: the ABC method and the lipid-linking method. As outlined in the Materials and Methods, the ABC method was a three-step process. Step 1 involved biotinylating the EV (including sub-steps: biotinylation, removing unbound biotin, and confirming EV biotinylation); step 2 involved mixing avidin with biotinylated EVs and biotinylated CTB; and step 3 involved removing unbound CTB by ultrafiltration and concentrating the final product. We found a limitation in this method: ultrafiltration with Amicon filter cones could not concentrate the product beyond a certain EV concentration. In contrast, the lipid-linking method was a three-step process. Step one involved adding DOPE-PEG-NHS to the CTB, followed by removing unbound DOPE-PEG-NHS via ultrafiltration. Step two was adding EV to the DOPE-PEG-CTB and crosslinking. Step three was to remove unbound DOPE-PEG-CTB and concentrate the sample by ultrafiltration. For lipid linking, we concentrated the CTB-EV sample to a higher particle count than with the ABC method.

EV characterization after surface modification.

The NTA, DLS, and TEM data are provided in the supplemental data (see Appendix Fig. B.1 (a-c and l-n) and B.2 (a-e) and Appendix Table B.1) and are briefly discussed here. The CTB monomer is approximately 11.2 kDa. NTA showed that naïve EVs had a mean size of 185.3 ± 2.3 nm and a mode size of 143.0 ± 7.0 nm. DLS showed a size of 146.0 ± 0.85 nm, a PDI of 0.23 ± 0.01, and a ZP of -16.09 ± 2.34 mV. After CTB conjugation to EVs, NTA showed larger mean sizes using the ABC method (223.1 ± 17.1 nm, $p = 1.84 \times 10^{-4}$) and the lipid-linking method (165.9 ± 2.3 nm, p = 0.03). NTA also showed no statistically significant difference in mode size (p = 0.99), with 141.5 ± 33.2 nm and 142.1 ± 3.7 nm for the ABC and lipid-linking methods, respectively. DLS showed sizes of 665.3 ± 29.07 nm ($p = 1.26 \times 10^{-7}$) and 169.6 ± 10.08 nm (p = 0.31) for the ABC method, which were larger than those of unconjugated EVs; the latter was not

statistically different from naïve EVs. Compared with naïve EVs, the ABC method PDI was 0.56 ± 0.09, significantly different from naïve ($p = 5 \times 10\text{-}4$), and the lipid-linking method PDI was 0.26 ± 0.02 ($p = 0.74$), not different from naïve EVs. This suggests that the ABC method may produce multiple particle populations, whereas the lipid-linking method produces a more uniform population. The ZP was -17.56 ± 1.92 mV ($p = 0.65$) and -4.28 ± 1.66 mV ($p = 8.55 \times 10^{-4}$) for the ABC and lipid-linking methods, respectively, compared with naïve EVs. Thus, CTB conjugation increased EV surface charge (i.e., made it more negative) compared to naïve EVs.

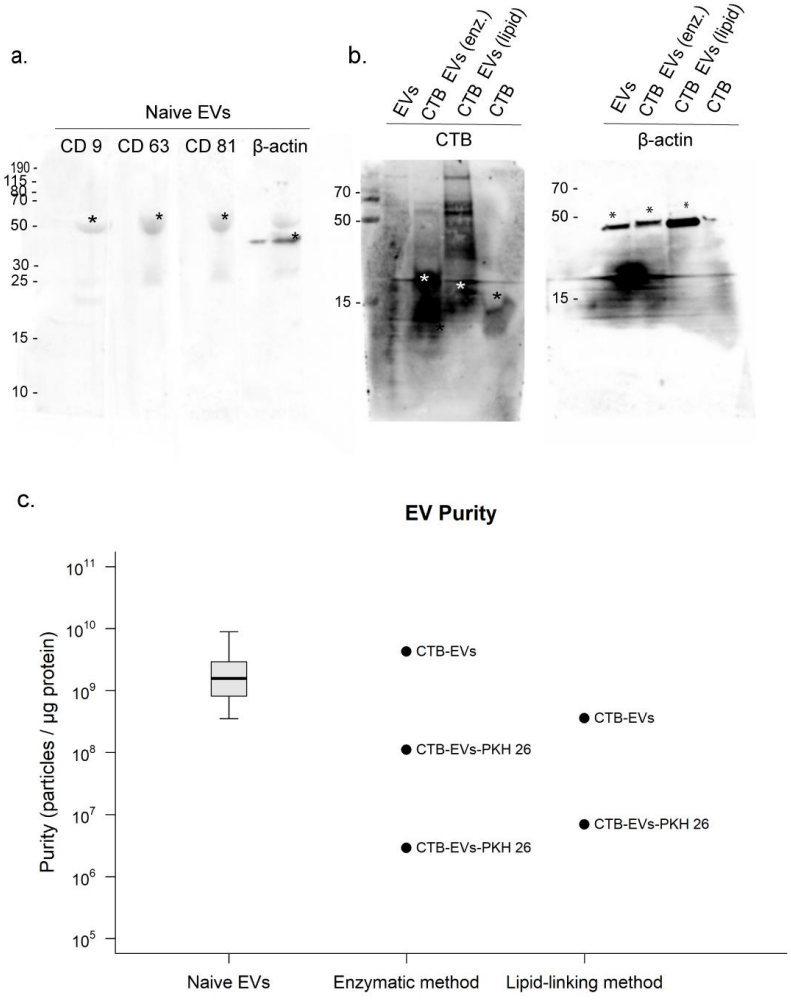


Figure 2.4. EV characterization and purity comparison of ligand conjugation: Western blot for (a) CD9, CD63, CD81, and β-actin detection. Naïve EVs were positive for all EV markers. (b)

CTB detection. After EV conjugation with CTB, CTB-EVs were positive for CTB. (c) Purity of EVs and CTB-EVs. CTB-EVS with both the ABC method and the lipid-linking method tend to decrease purity compared to naïve EVs

TEM data showed the size ± SD (nm) of naïve EVs, EVs with CTB by the ABC method, and EVs with CTB by the lipid-linking method were 50.44 ± 28.84, 73.67 ± 53.87, and 139.14 ± 44.94 nm, respectively (see supplemental data; Appendix Figure B.1(l- n)). Specifically, we did not observe additional clumping or dimer formation in the ABC method sample, as indicated by the PDI, or gross changes in particle size, as indicated by DLS. Since the particles were negatively stained, we did not observe changes in the EV membrane that might be associated with CTB conjugation.

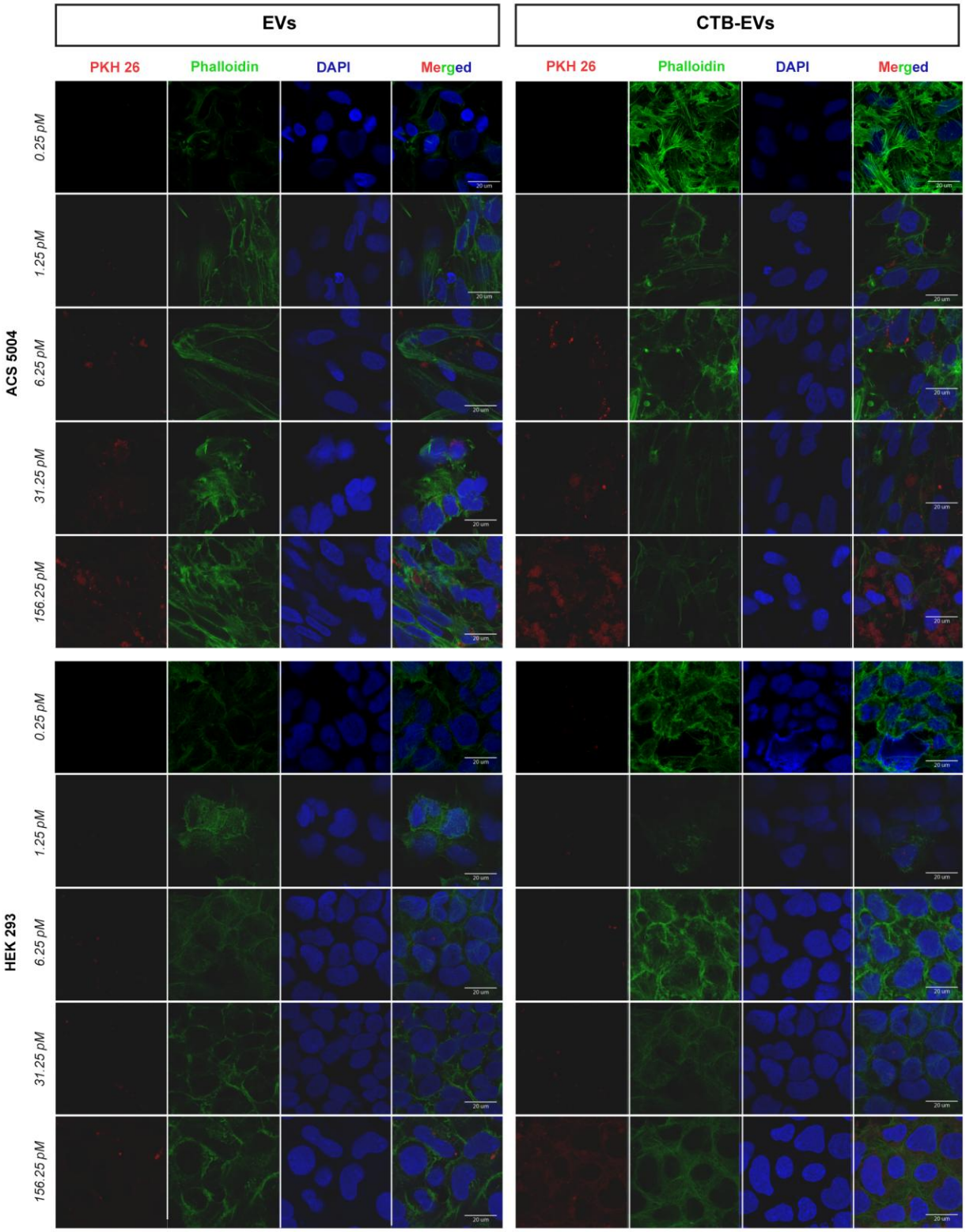
Western blot and ELISA indicated CTB incorporation: Western blot results in Figure 2.7b show that both the ABC and lipid-linking methods successfully conjugated CTB to EVs. The Western blot showed CTB in both ABC and lipid-linking samples. In contrast, the ELISA results in Appendix Figure B.3 showed that CTB-EVs conjugated by the ABC method had CTB levels below the detection limit. In contrast, CTB-EVs conjugated by the lipid-linking method had a CTB concentration of 0.213 pg/10^6 particles. In summary, the Western blot data suggest that both methods successfully conjugated CTB to EVs, and the ELISA suggests that the lipid-linking method added more CTB per EV than the ABC method.

We compared the purity of naïve EVs and EVs conjugated with CTB by ABC or lipid-linking methods. Depending on how EV purity is defined, we expected purity values to decrease after adding the protein CTB to the EVs. As shown in Figure 2.7c, we observed a trend toward decreased purity after both the ABC and lipid-linking methods.

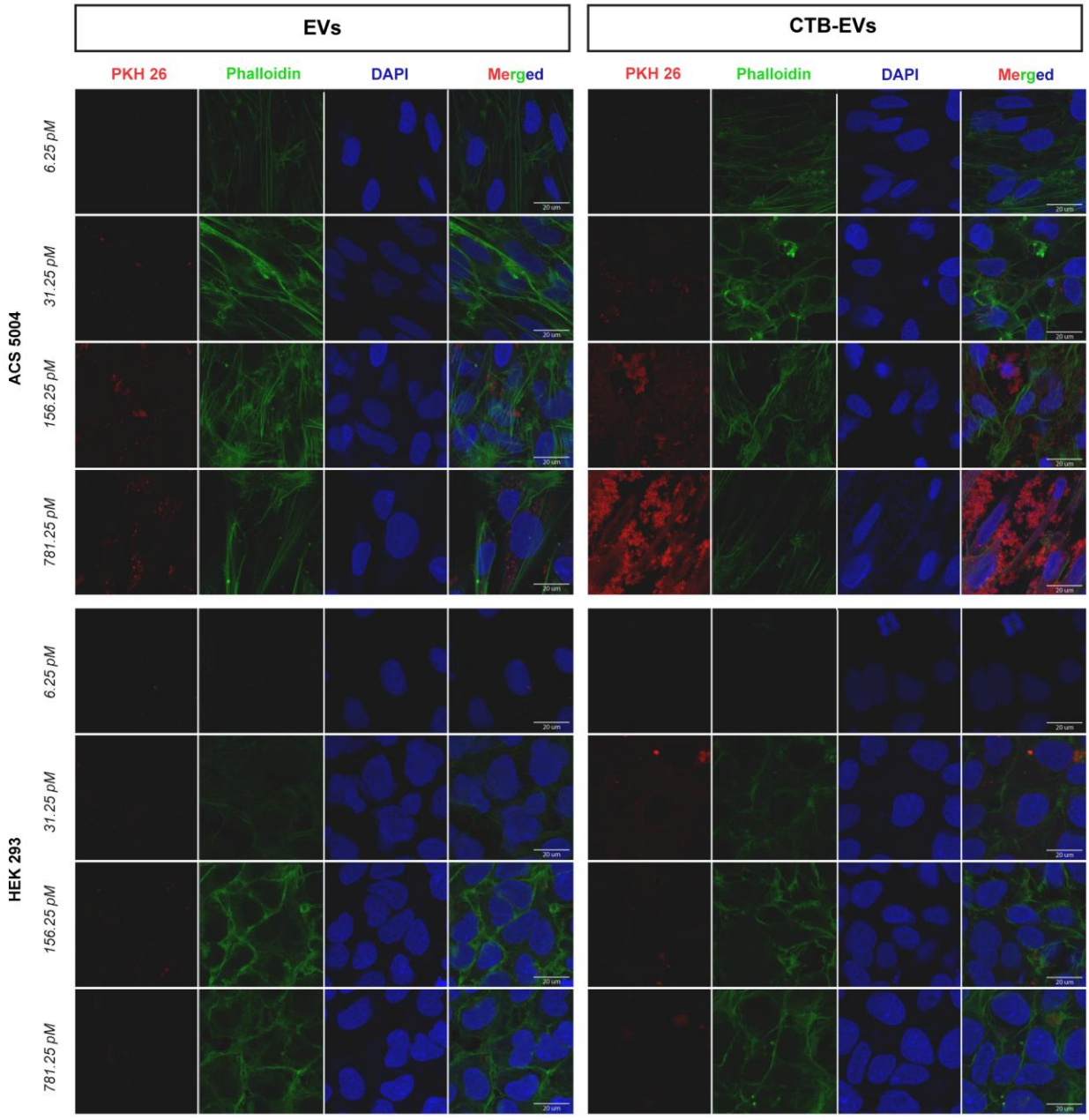
Cellular uptake comparison of the different methods for conjugating CTB onto EVs

We assessed in vitro cellular uptake of CTB-conjugated EVs using the two methods. Figures 2.8a and 2.8c show CTB-EV uptake after the ABC method (EV biotinylation with avidin and biotinylated CTB), and Figures 2.8b and 2.8d show CTB-EV uptake after the lipid-linking method (DOPE-PEG-NHS). Two different cell types, ACS 5004 (human neural progenitor cell line) and HEK 293 (human embryonic kidney cell line), were used to assess CTB-EV uptake at varying doses, including 0.25 pM, 1.25 pM, 6.25 pM, 31.25 pM, and 156.25 pM of CTB-EVs for the ABC method and 6.25 pM, 31.25 pM, 156.25, and 781.25 pM of CTB-EVs for the lipid-linking method. We performed the experiment in technical triplicates. After transforming the fluorescent intensity ratio into a log response, we used an ANOVA to examine the main effects of EV type (naive EV vs. CTB-EV), cell line (ACS5004 vs. HEK 293), and the five doses on fluorescence intensity, as well as all interactions, because the raw fluorescent intensity dataset did not meet the assumptions of normality and homogeneity of variance required for ANOVA. We found a significant three-way interaction for the ABC method but not for the lipid-linking method. We used a post hoc Holm-Bonferroni adjustment to examine pre-planned comparisons.

a. Enzymatic Method



b. Lipid-linking Method



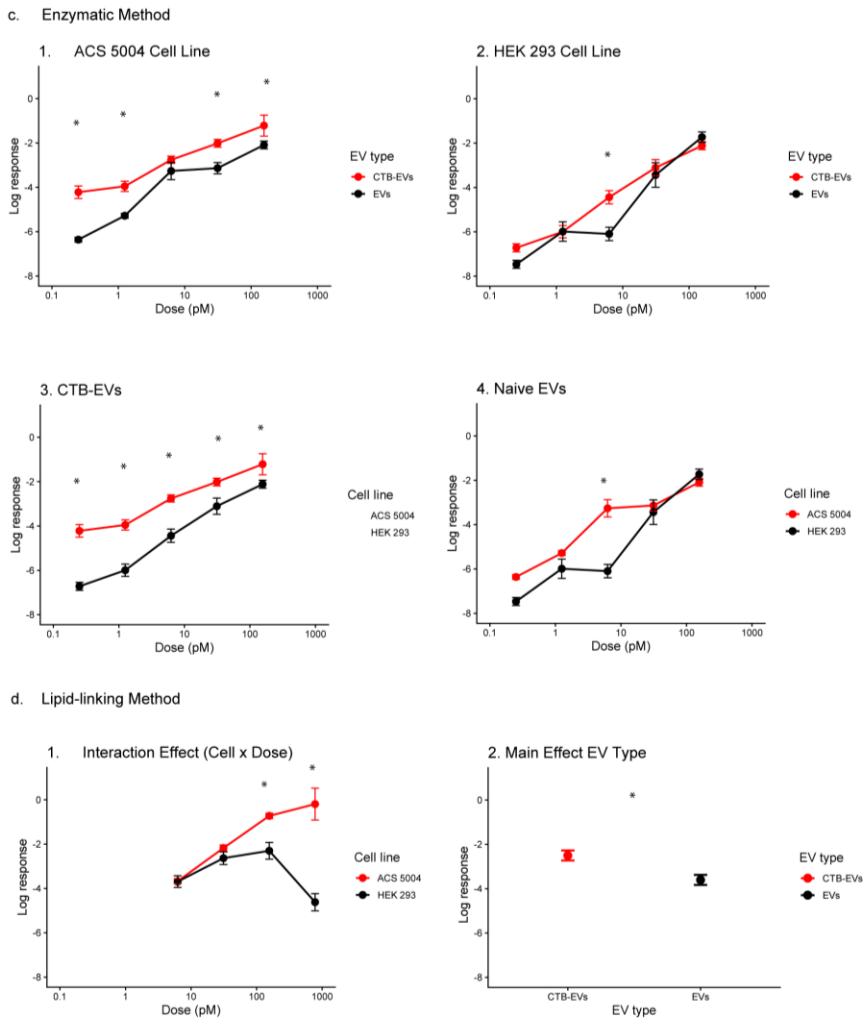


Figure 2.5. Uptake of EVs or CTB-EVs by two cell lines: ACS 5004 and HEK 293. (a) Representative confocal microscopy images of EVs or CTB-EVs (EV membrane labeled with the lipophilic membrane dye PKH 26, red) in ACS 5004 and HEK 293 cells at different doses (0.25, 1.25, 6.25, 31.25, and 156.25 pM) using the ABC method. (b) Representative confocal microscopy images of EVs and CTB-EVs (labeled with the lipophilic membrane dye PKH 26, red) in ACS 5004 and HEK 293 at different doses (6.25, 31.25, 156.25, and 781.25 pM) using the lipid-linking method. (c) Quantitative analysis of the ABC method. CTB-EVs were taken up in a dose-dependent manner by ACS 5004 cells. (d) Quantitative analysis of the lipid-linking method. (Calibration bar = 20 µm, brightness and contrast adjusted). Note: Both the ABC method and lipid linker method for CTB conjugation on EVs were successful and tend to be specific to ACS 5004 more than HEK 293

First, we compared CTB-EV uptake versus naive EV uptake in the two cell lines following ABC conjugation (Fig. 2.8a and c). In Figure 2.8c(1) in the ACS 5004 cell line, CTB-EVs showed significantly different (higher) accumulation than naive EVs at doses of 0.25, 1.25, 31.25, and 156.25 pM ($p = 1.28 \times 10^{-6}$, $p = 0.002$, $p = 0.008$, and $p = 0.037$, respectively) except only 1 dose at the middle (6.25 pM) that did not show higher accumulation. Thus, in ACS 5004, EV uptake appears to be influenced by the addition of the CTB ligand and by varying the particle dose.

Figure 2.8c(2) shows the uptake of naive EVs and CTB-EVs in the HEK 293 cell line. CTB-EVs showed a different (higher) accumulation at the middle dose (6.25 pM) ($p = 1.28 \times 10^{-4}$) only. HEK 293 showed a trend toward increased uptake with CTB-EVs compared with naive EVs. Thus, in HEK 293 cells, particle concentration appears to influence cellular uptake—more than ligand.

In Figure 2.8c(3), uptake of CTB-EVs was compared between the two cell lines: ACS 5004 and HEK 293. This graph showed that ACS 5004 had higher uptake than HEK 293 for CTB-EVs at all doses. This indicates that ACS5004 takes up more CTB-EVs.

Figure 2.8c(4) compares naïve EV uptake between the two cell lines, ACS 5004 and HEK 293. The graph shows a trend toward greater uptake in both cell lines as doses increased, with higher uptake only for ACS 5004 at the lowest dose (0.25 pM; $p = 0.009$) and at the middle dose (6.25 pM; $p = 7 \times 10^{-10}$). This indicated that naive EV uptake increased in both cell types, with some low- to mid-dose levels higher in ACS 5004.

In summary, both cell types showed a dose-dependent trend toward increased uptake of naive and CTB-EV. However, ACS5004, the neural cell type, showed a larger, more consistent difference, specifically greater CTB-EV uptake. Thus, the data suggest that ABC-conjugated CTB-EVs enhanced cellular uptake in ACS5004 compared with HEK 293 cells.

Second, in Figures 2.8b and 2.8d, we compared CTB-EV uptake with naive EV uptake in the two cell lines following lipid-linking conjugation (Fig. 2.8b and 2.8d). No significant three-way interaction emerged among doses, cell lines, and EV type ($p = 0.368$). However, the two-way interaction between cell lines and doses was significant ($p < 0.01$). EV type also had a significant main effect.

FFigure 2.8d(1) showed the two-way interaction between cell lines and doses. At the two highest doses (156.25 pM and 781.25 pM), ACS 5004 had a higher estimated mean than HEK 293. Figure 2.8d (2) showed that the main effect indicated that CTB-EVs had a higher estimated mean than EVs, regardless of cell type or dose. Thus, with the lipid-linking method for CTB-EVs, uptake exceeded that of naïve EVs across cell lines and doses, reflecting the main effect of EV type. Uptake was cell-line-dependent for ACS 5004, especially at the two highest doses, although ACS 5004 showed no CTB-EV-specific uptake.

In summary, these data support the notion that conjugating the CTB ligand can enhance EV uptake, although the effect varies with conjugation method, cell type, and dose. With the ABC method, ACS 5004 showed more consistent CTB-EV uptake and enhanced targeting, suggesting a preference for neural cells. With the lipid-linking method, CTB-EVs also showed significantly greater overall uptake regardless of cell type or dose, reflecting CTB's overall effect on EV uptake. At the higher dose, ACS 5004 showed greater uptake than HEK 293, although this was not significant. We attributed the difference to CTB specifically, as there was no significant 3-way interaction. Taken together, both approaches supported the conclusion that CTB modification increases EV uptake. Although we did not directly compare the two conjugation methods, we selected the method for the following work based not only on cellular uptake or biological activity but also on physicochemical characterization, CTB incorporation, and practical considerations.

The lipid-linking method demonstrated several advantages. First, it was faster to prepare because it required fewer, simpler steps and had a more practical workflow. Second, it produced a more uniform particle population than the ABC method, as indicated by the PDI. Third, it yielded greater CTB per EV than the ABC method, as measured by ELISA. Fourth, it enabled preparation of CTB-EVs at a higher final concentration than the ABC method. For these reasons, we used the lipid-linking method for the downstream experiments.

Experiment 3a. Lipid-linking method for WGA-EVs (In Vitro Analysis: dose-response)

As described above, the lipid-linking method conjugates WGA to the EV surface.

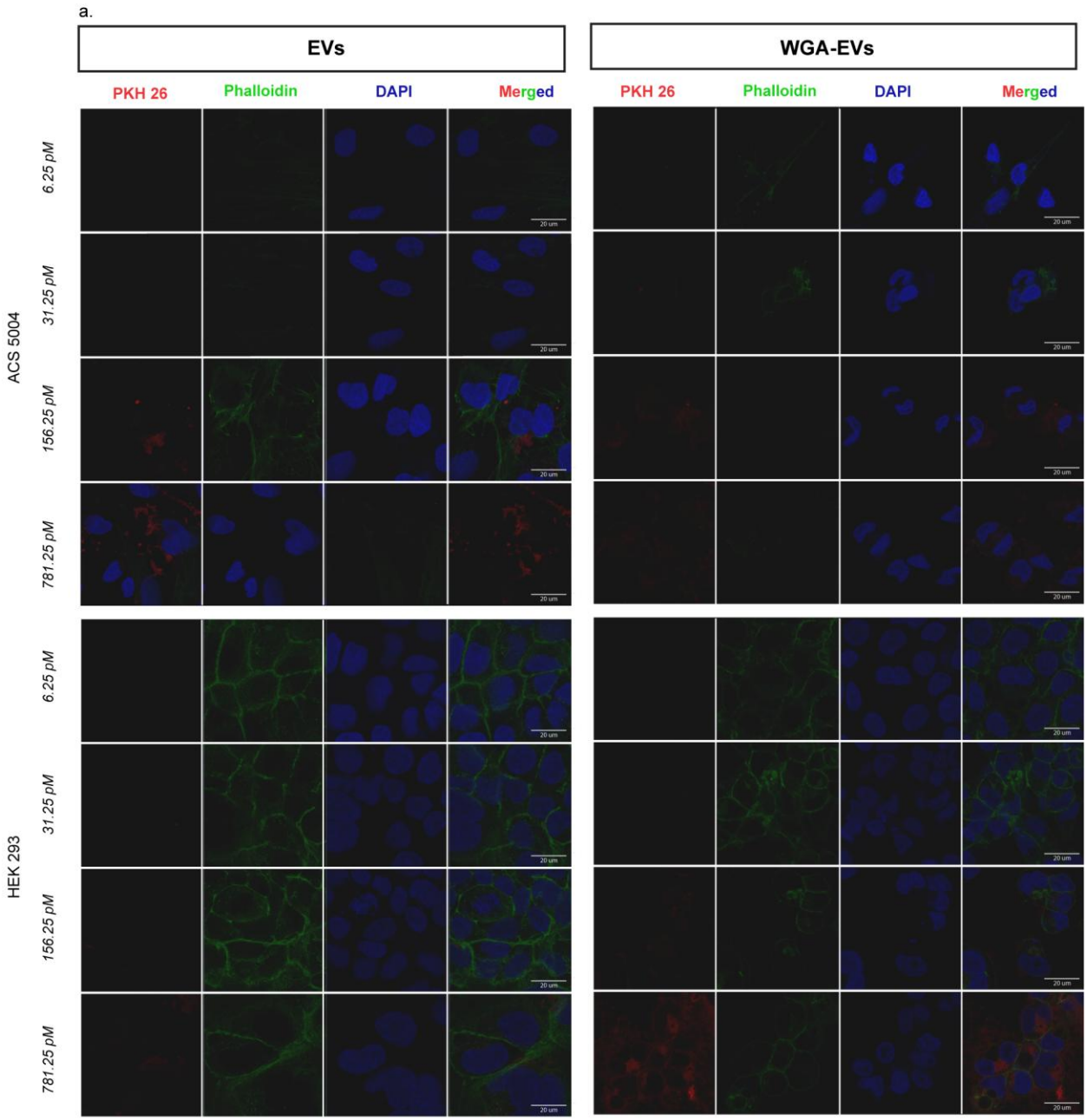
EV characterization after surface modification.

The WGA monomer is approximately 33 kDa. Western blot showed WGA conjugation successfully onto EVs (Appendix Figure B.4). As shown in Appendix Table B.1 and Appendix Fig. B.1 (d-e, o-p) and B.2 (f-j), NTA showed that naïve EVs had a mean size of 155.8 ± 1.6 nm and a mode size of 130.8 ± 3.7 nm. DLS showed a size of 169.5 ± 8.8 nm, a PDI of 0.30 ± 0.00, and a ZP of -11.13 ± 1.23 mV. After WGA conjugation to EVs, NTA showed a different mean ($p = 2.03 \times 10^{-9}$) and mode size ($p = 1.41 \times 10^{-6}$) (mean = 95.6 ± 3.4 nm and mode = 78.4 ± 1.1 nm). DLS showed a size of 6164 ± 1074.0 nm, which was larger than that of naïve EVs (p = 0.01). The PDI was 0.41 ± 0.23 (p = 0.49), and the ZP was -7.84 ± 2.31 mV (p = 0.09), neither of which differed significantly from naïve EVs. Thus, WGA conjugation did not change ZP and EV surface charge compared to naïve EVs.

Cellular uptake comparison of WGA-EVs and naïve EVs.

Next, we asked whether WGA conjugation to EVs modified EV uptake in vitro, as observed for CTB-EVs (Fig. 2.9a and b). We used an ANOVA to examine the main effects of EV

type (naive EV vs. WGA-EV), cell line (ACS5004 vs. HEK 293), and the four doses of EVs and WGA-EVs, as well as all interactions. The fluorescent intensity ratio was transformed to a log-scale response, as in previous experiments, for four doses: 6.25 pM, 31.25 pM, 156.25 pM, and 781.25 pM.



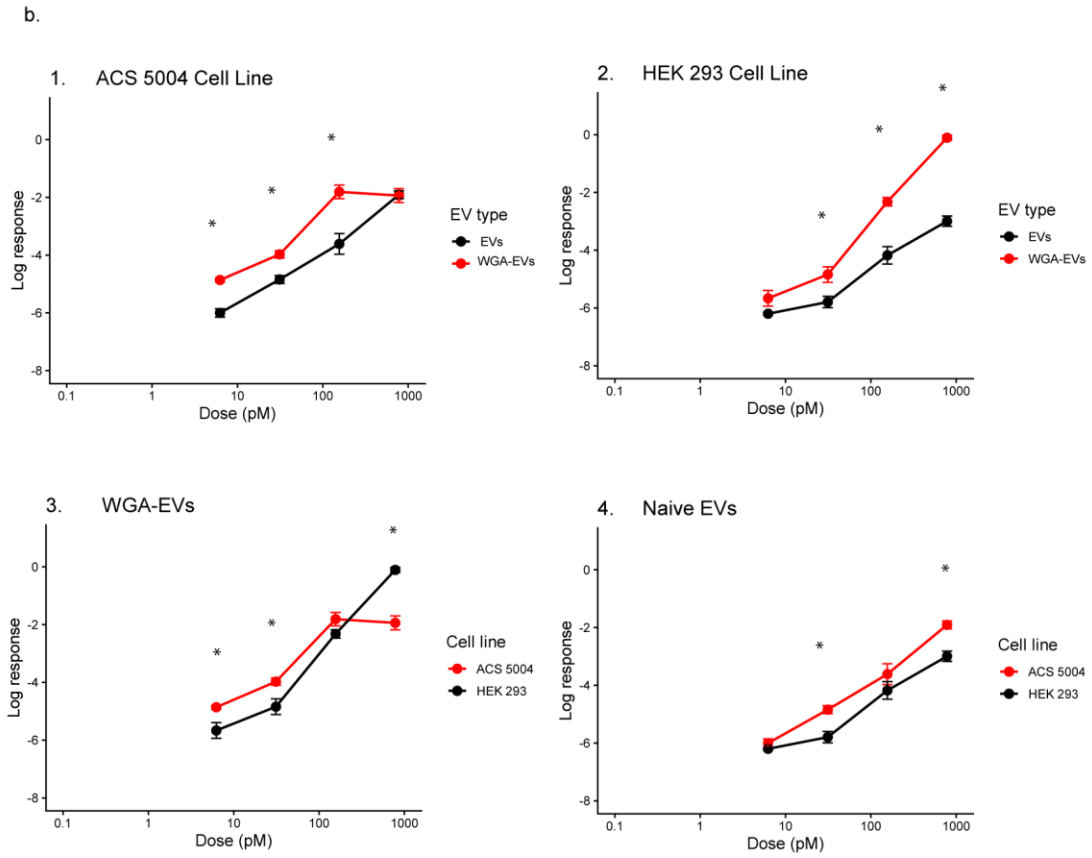


Figure 2.6. Uptake of EVs or WGA-EVs by two cell lines: ACS 5004 and HEK 293. (a) Representative confocal microscopy images of EVs or WGA-EVs (EV membrane labeled with the lipophilic membrane dye PKH 26, red) in ACS 5004 and HEK 293 cells at different doses (6.25, 31.25, 156.25, 781.25 pM) using the lipid-linking method. (b) Quantitative analysis using the lipid-linking method indicated that ACS 5004 did not specifically take up WGA-EVs. (Calibration bar = 20 µm, brightness and contrast adjusted).

Figure 2.9b (1 and 2) shows WGA-EV uptake versus naïve EV uptake across four doses in ACS 5004 and HEK 293. In both cell lines, EV and WGA-EV uptake increased dose-dependently, with some statistical significance. In ACS 5004 Fig. 2.9b(1), WGA-EV uptake was higher than EV uptake at all doses except the highest (781.25 pM). In HEK 293 cells Fig. 2.9b(2), WGA-EV

uptake was also higher than naïve EV uptake at all doses except the lowest. These trends suggest that WGA-EVs increase uptake in cells regardless of cell type.

In Figure 2.9b (3 and 4), respectively, WGA-EV and naïve EV uptake were compared between the two cell lines. For WGA-EVs, as shown in Figure 2.9b(3), ACS 5004 showed modest but significantly different uptake than HEK 293 at the two lower doses (6.25 pM, $p = 0.0063$ and 31.25 pM, $p = 0.0033$). At 156.25 pM, uptake did not differ ($p = 0.052$). In contrast, HEK 293 took up more WGA-EVs, with significantly higher uptake at the highest dose compared to ACS 5004 (781.25 pM, $p = 1.03 \times 10^{-8}$). In Figure 2.9b(4), uptake of naïve EVs is again compared between the two cell lines, as in experiment 2; a modest, dose-dependent increase was observed in the ACS 5004 cell line. This independent experiment confirms the above: naïve EV uptake increases with increasing particle concentration. This experiment replicated previous findings showing that naïve EVs are taken up in a dose-response manner by both ACS5004 and HEK 293 cells. These results suggest that WGA-EVs increase uptake in ACS 5004 at low doses but not at high doses.

In summary, these findings suggest that WGA conjugation enhanced uptake in HEK 293 cells and the neural cell line ACS 5004. This means that although uptake increased, it was not specific to the cell of interest. In contrast, in vitro testing of CTB-EVs suggests that surface modification by adding CTB can alter uptake in a particular cell line, specifically ACS 5004.

Experiment 3b: Lipid-linking method for CTB, WGA, to liposomes (In Vitro Analysis:dose-response)

We used the thin-film method for liposome synthesis, followed by conjugation with CTB or WGA using a lipid-based conjugation method. During liposome synthesis and after conjugation, we extruded liposomes through 100 nm and 1,000 nm membranes (respectively) to produce a consistent product size. As shown in Appendix Table B.3 and Appendix Figure B.5, we used NTA

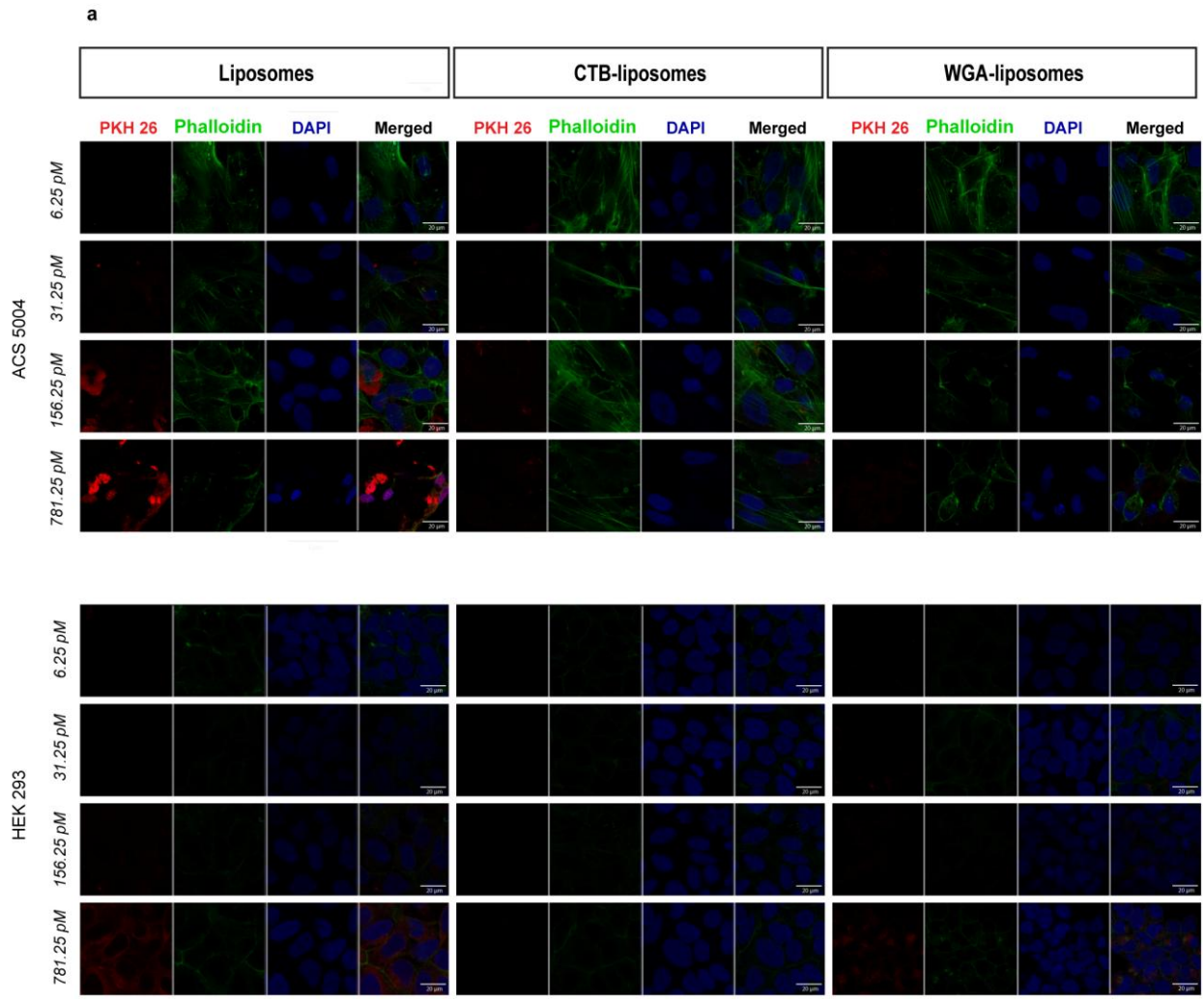
to measure size and particle concentration. We used DLS to measure size, PDI, and zeta potential. We used Western blot to confirm successful conjugation of CTB and WGA. Finally, we tested liposomes for cellular uptake in ACS 5004 and HEK 293 cells across a range of doses.

Cellular uptake comparison of liposomes conjugated with CTB or WGA (CTB-liposomes and WGA-liposomes)

Fig. 2.10 (a-b) compares cellular uptake of liposomes, CTB-liposomes, and WGA-liposomes. We transformed the fluorescent intensity ratio to a log scale, as in previous experiments, at four doses (6.25 pM, 31.25 pM, 156.25 pM, and 781.25 pM), then performed ANOVA. Although we observed no 3-way interaction among liposome type (liposomes vs. CTB-liposomes vs. WGA-liposomes), cell line (ACS 5004 vs. HEK 293), and the four doses, we observed 2 main interaction effects. We analyzed 2 main interactions: liposome type × cell line and liposome type × dose, as described below.

First, we assessed the liposome type × cell line interaction regardless of dose (Fig. 2.10a (1-2)). As shown in Figure 2.10b(1), in the ACS5004 cell line, unconjugated liposomes had higher uptake than CTB-liposomes and WGA-liposomes ($p = 0.0001$ and 3.87×10^{-6}, respectively). In HEK 293 (Fig. 2.10b(1)), liposomes had higher uptake than CTB-EVs ($p = 4.01 \times 10^{-11}$). However, WGA-liposomes had higher uptake than liposomes in HEK 293 ($p = 3.87 \times 10^{-6}$) and than CTB-liposomes ($p = 2.50 \times 10^{-24}$). Interestingly, ACS5004 showed higher uptake than HEK 293, regardless of conjugation.

Second, another main interaction was assessed: liposome type × dose, regardless of cell line (Fig. 2.10b(3)). At the lowest dose, 6.25 pM, WGA-liposomes showed higher uptake than


a
Liposomes
CTB-liposomes
WGA-liposomes
PKH 26
Phalloidin
DAPI
Merged
ACS 5004
HEK 293
6.25 pM
31.25 pM
156.25 pM
781.25 pM

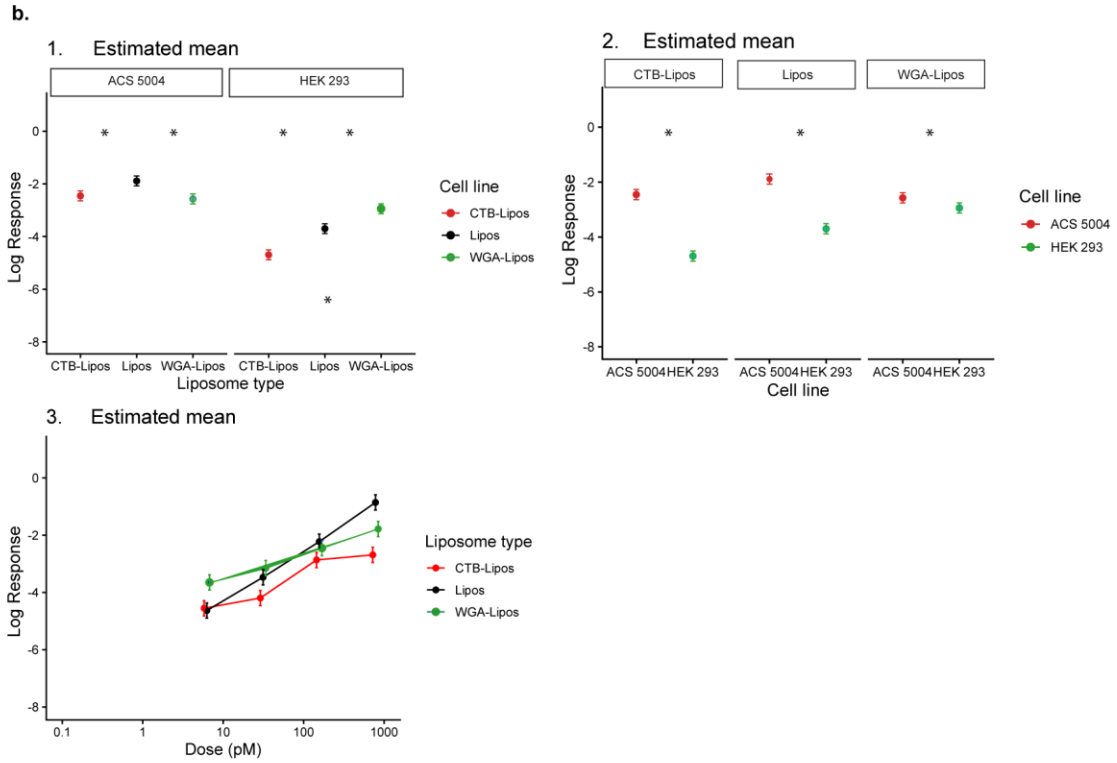


Figure 2.7. Uptake of liposomes, CTB-liposomes, or WGA-liposomes by two cell lines: ACS 5004 and HEK 293. (a) Representative confocal microscopy images of liposomes, CTB-liposomes, or WGA-liposomes (liposome membrane labeled with the lipophilic membrane dye PKH 26, red) in ACS 5004 and HEK 293 cells at different doses (6.25, 31.25, 156.25, 781.25 pM). (b) Quantitative analysis showed that ACS 5004 did not specifically take up CTB-liposomes or WGA-liposomes. (Calibration bar = 20 µm, brightness and contrast adjusted)

CTB liposomes and liposomes ($p = 0.0004$ and $p = 2.66 \times 10^{-6}$, respectively). However, at 31.25 pM, liposomes showed higher uptake than CTB-liposomes ($p = 0.0004$), and WGA-liposomes showed higher uptake than CTB-liposomes ($p = 6.63 \times 10^{-7}$). At 156.25 pM, liposomes had higher uptake than CTB-liposomes ($p = 0.0031$). At the highest dose, 781.25 pM, the highest uptake was in liposomes, which was higher than WGA-liposomes and CTB-liposomes ($p = 6.57 \times 10^{-6}$ and $p = 3.40 \times 10^{-16}$), with WGA-liposomes higher than CTB-liposomes ($p = 6.57 \times 10^{-6}$)

In summary, conjugation of liposomes with WGA or CTB did not significantly enhance liposome uptake in ACS 5004. Surprisingly, uptake of unconjugated liposomes was higher than that of conjugated ones. Additionally, all liposomes, including CTB-liposomes and WGA-liposomes, targeted ACS 5004 rather than HEK 293. This suggests that uptake in the neural cell line ACS 5004 may be driven by the nanocarrier itself rather than the ligands. Taken together, ACS 5004 neural cells did not prefer either CTB-liposomes or WGA-liposomes, and naïve liposomes showed the strongest uptake.

Metabolic activity assessment of CTB-EVs, CTB-liposomes, WGA-EVs, and WGA-liposomes on ACS 5004 and HEK 293

For the MTT assessment, as shown in the appendix. fig. B.6, we used ART-ANOVA because the data did not meet the assumptions of normality and homogeneity of variance. For EVs, we tested doses of 6.25 pM, 31.25 pM, 156.25 pM, and 781.25 pM of EVs, CTB-EVs, and WGA-EVs. We tested two cell lines, ACS 5004 and HEK 293, as in experiments 2 and 3. In ACS 5004 (appendix fig. B.6a), at 31.25 pM, metabolic activity differed more between CTB-EVs and EVs than between CTB-EVs and WGA-EVs ($p = 0.02$), and CTB-EVs had higher metabolic activity than WGA-EVs ($p = 0.02$). In HEK 293 (appendix fig. B.6b), no statistically significant differences were observed among the EVs at any dose. This indicated that CTB-EVs and WGA-EVs showed effects at some doses in ACS 5004 but not in HEK 293, compared with EVs.

We used the same doses and cell lines for liposomes **as** for **EVs.** As shown in Appendix Figure B.6c, at 31.25 pM in ACS 5004, WGA-liposomes had higher metabolic activity than CTB-liposomes ($p = 0.04$), and CTB-liposomes had higher metabolic activity than WGA-liposomes ($p = 0.04$**). In HEK 293** (appendix figure B.6d)**, at 156.25 pM and 781.25 pM, WGA-liposomes had higher metabolic activity than liposomes ($p = 0.04$ for both). This indicated that CTB-**

EVs and WGA-EVs showed effects at some doses in ACS 5004 and HEK 293, compared with EVs.

Taken together, conjugated EVs and liposomes with either CTB or WGA caused differences in metabolic activity at some of the doses tested in ACS 5004 and HEK 293.

Experiment 4a: Fluorogold injection to determine the end of the experiment

The next experiment in the animal model focused on analyzing EV modifications conjugated to either CTB or WGA. To do that, we assessed in vivo detection using CTB-EVs, WGA-EVs, and EVs. They were injected into rats' hind feet to track retrograde transport to the DRG and organ distribution throughout the body on day 7. To determine the optimal day for sample collection, we injected fluorogold (FG) to track retrograde transport and compare days 5 and 7. The results showed no statistically significant difference between days 5 and 7. We therefore chose day 7 for the rest of the experiment (Appendix, Fig. B.7a and b). The latter time point provided sufficient time for retrograde transport and accumulation for the assessment.

Experiment 4b: Loading eGFP/ mCherry-EVs (In vitro analysis)

Next, EVs loaded with different fluorescent proteins, including eGFP and mCherry, were prepared for in vivo experiments to compare CTB-EV and WGA-EV injections (Fig. 2.11). To test which method successfully loaded fluorescent protein into EVs, the experiment used eGFP under different loading treatments, including sonication, 2-hour room-temperature incubation, and 2-hour incubation at 37 °C. A Western blot comparison was then performed after these procedures to determine whether the protein was located on the membrane or inside EVs. After room-temperature incubation, relatively less protein was detected than after 37 °C incubation and sonication (fig. 2.11a). Therefore, only the 37 °C incubation and sonication condition was used to analyze location.

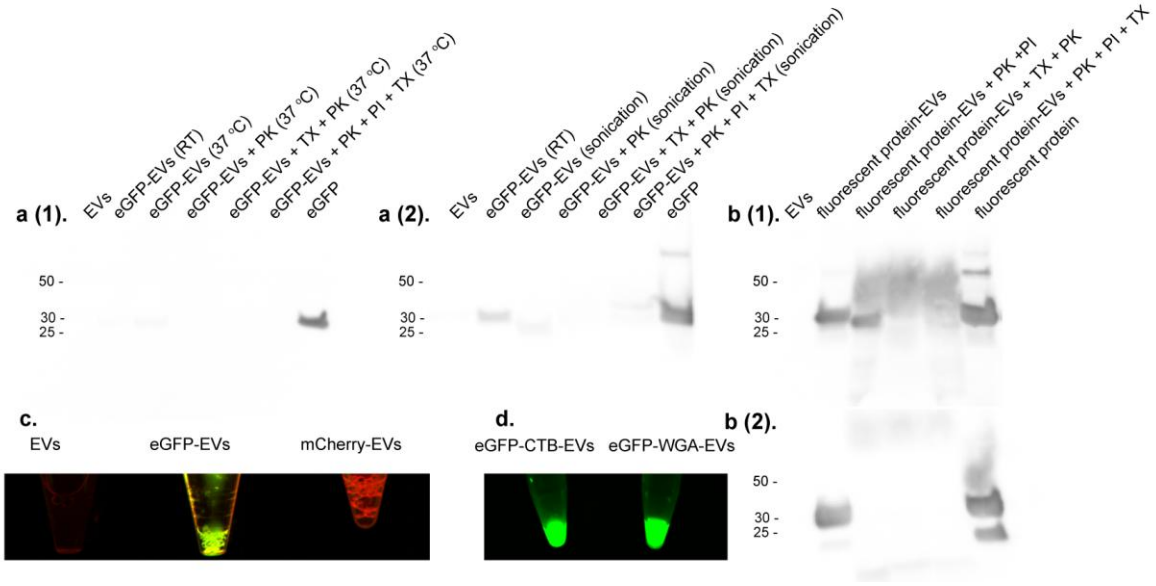


Figure 2.8. Loading of fluorescent protein into EVs using various methods and detection. (a) Western blot of eGFP-EVs under different treatments after EV loading with eGFP. (a(1).) eGFP was loaded into EVs at RT or 37 °C, then subjected to various treatments to determine its localization. (a (2).) eGFP was loaded into EVs at RT or by sonication, then subjected to various treatments to determine its localization. (b) Western blot of (b (1)) eGFP-EVs or (b (2)) mCherry-EVs under different treatments after EV loading. (c) Fluorescent detection of naïve EVs, eGFP-EVs, and mCherry-EVs. (d) Fluorescent detection of eGFP-CTB-EVs and eGFP-WGA-EVs. (RT: room temperature, PK: proteinase K, PI: protease inhibitor, TX: Triton X-100). Note: eGFP and

mCherry were successfully loaded into EVs. eGFP was present on the membrane and inside, whereas mCherry was membrane-only.

The results showed that after proteinase K (PK) treatment of eGFP-EVs (37 °C incubation), no detectable signals were observed. This indicated that 37 °C incubation allowed eGFP to bind to the EV membrane rather than reside inside EVs, as shown in the sup. fig. 2.11a (1). However, after sonication of eGFP-loaded EVs and treatment with PK and proteinase inhibitor (PI), detectable signals remained, albeit at lower levels. Therefore, sonication of eGFP-EVs resulted in eGFP being present on the membrane and inside the EVs, as shown in Fig. 2.11a(2), and sonication was used to load eGFP and mCherry into EVs in the next step.

Next, we loaded EVs with fluorescent proteins (eGFP or mCherry) by sonication and applied various treatments to determine whether the proteins were inside or on the EVs (Fig. 2.11b). The results showed that sonication successfully loaded the proteins (eGFP) into the EVs. For eGFP EVs, the eGFP signal remained strong after PK treatment, as shown in the supplementary material. fig. 2.11b (1). After permeabilizing eGFP-EVs with Triton X-100 (TX), the eGFP signal was lost in some cases, indicating that eGFP was loaded onto and within the EVs. For mCherry-EVs, by contrast, the protein was on the membrane, since no signal remained after treatment with PK and PI, as shown in Fig. 2.11b (2). These results indicate that eGFP and mCherry were successfully loaded into EVs, although at different locations.

We confirmed fluorescent protein loading after sample preparation and before in vivo analysis. We used eGFP-EVs for CTB and WGA (eGFP-CTB-EVs and eGFP-WGA-EVs, respectively), and mCherry-EVs as naïve EVs. After sonication, the fluorescent protein remained intact in both eGFP-EVs and mCherry-EVs (Fig. 2.11c). Additionally, after eGFP-EVs bound to either CTB or WGA, the fluorescent signal remained (Fig. 2.11d).

Experimental 4c: eGFP-CTB EVs vs mCherry-EVs (In vivo analysis)

We compared eGFP-CTB EVs and mCherry-EVs in a rat model as shown in Fig. 2.12. On day 0, five animals received eGFP-CTB-EVs in the left hind foot and mCherry-EVs in the right hind foot. One animal served as a control: a needle was inserted into the left hind foot, and 30 uL of PBS was injected into the right hind foot. Footpad thickness was measured in triplicate at the following times (before injection and at 0, 3, 6, 24, 48, 72, and 168 hours after injection). The experiment ended on day 7 (168 hours) after injection. Organs were collected on day 7 after sacrifice. Organs, including the heart, lungs, liver, spleen, kidneys, left and right sciatic nerves, left and right popliteal lymph nodes, and left and right feet, were analyzed using the IVIS system. We further evaluated the left and right L3-L5 DRG by sectioning and immunofluorescent staining. We used anti-eGFP and anti-mCherry antibodies as primary antibodies for immunofluorescence staining of the left- and right-sided organs, respectively. Confocal microscopy was used to image six randomly selected areas. Small-DRG neurons and medium-to-large-DRG neurons were categorized by neuronal area, using a 600 μm^2 cut-off.

First, we measured footpad thickness throughout the experimental procedure (Fig. 2.12a). We analyzed the interaction effect of treatment groups and time points (as indicated above) using a two-way repeated-measures ANOVA within each treatment group. The results showed no change in footpad thickness across time points compared with the pre-injection baseline, except for eGFP-CTB-EVs and mCherry-EVs on day 7, which had thinner footpads than before injection ($p = 0.013$ and $p = 0.010$, respectively).

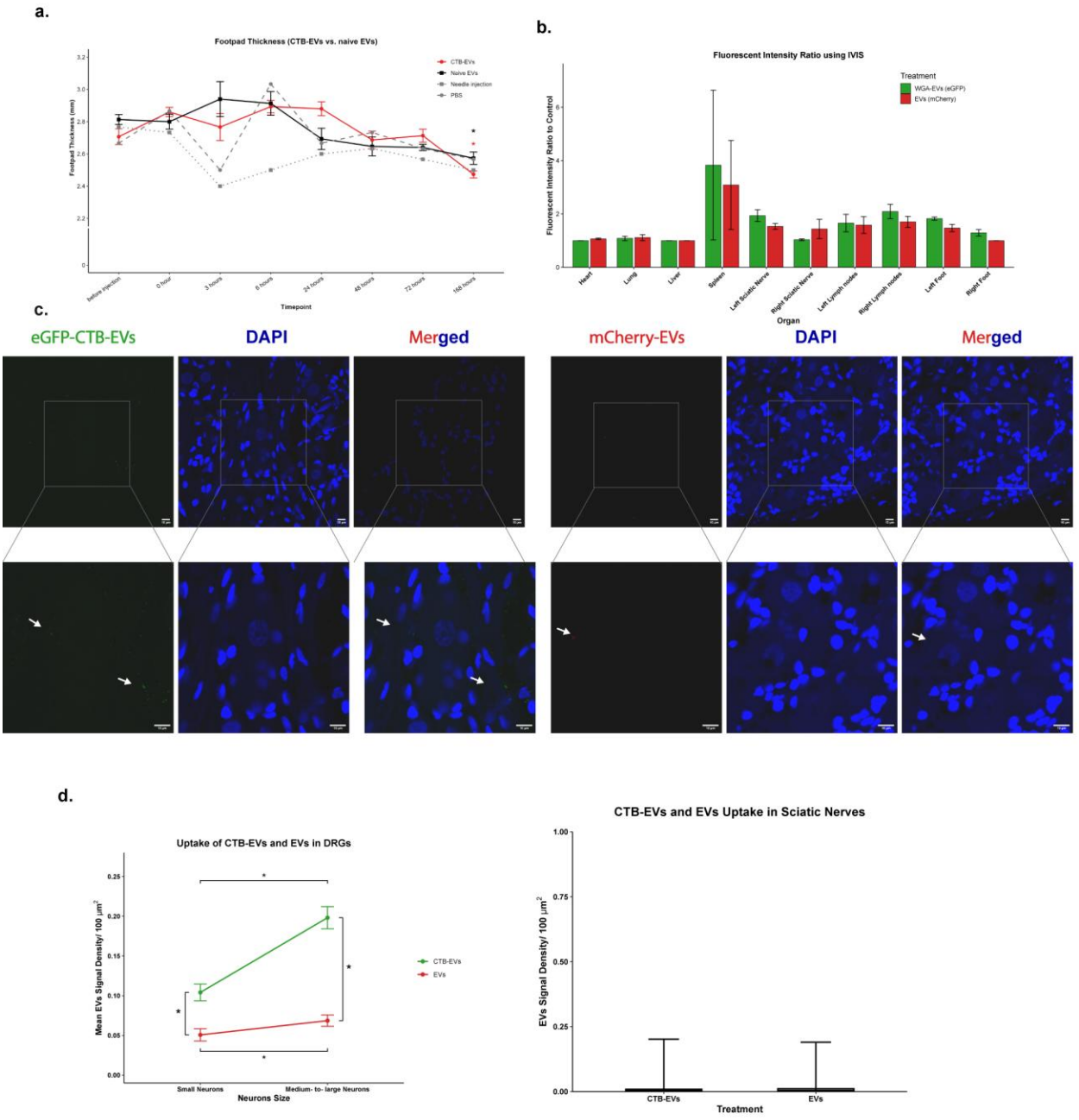


Figure 2.9 CTB-EVs vs. EVs uptake analysis in an animal model. (a) Footpad thickness of animals. (b) Analysis using the IVIS system. Note: No statistically significant difference between CTB-EVs and EVs uptake in different organs. (c) Representative confocal microscopy images of mCherry-EVs or eGFP-CTB-EVs in DRG. (d) Quantitative analysis using a binomial model of CTB and EVs in DRG, and quantitative analysis of the number of detected observations of CTB and EVs in DRG.

The ratio relative to the control animal. We used ART-ANOVA to analyze the data and determine whether different organs and treatments affected the fluorescent intensity ratio relative to the control. The results showed that there was no statistically significant difference between organs and treatments (eGFP-CTB-EVs vs mCherry-EVs) ($p = 0.370$)

Lastly, we evaluated uptake in DRG using confocal microscopy, The two-part model was used for analysis: 1. detection status (detected versus not detected) as a binomial model, and 2. observed amount among detected observations. This was because confocal microscopy detection in the eGFP-WGA-EVs vs mCherry-EVs experiment (exp. 4d) showed signal only in 21 DRGs among the 2,654 DRGs we measured; the rest showed no signal. Given the missing (unknown) limit of detection, we did not know whether the detected signals were true positives, so we used the two-part model mentioned above.

For the binomial model (detected vs. not detected), as shown in Fig. 2 .12d, the interaction effect (EV type x Cell size) was not statistically significant ($p = 0.785$), indicating no evidence that the EV-type difference in detection varied by cell size. In medium to large DRG, the EVs have lower detection odds than CTB-EVs ($p < 0.001$). For CTB-EVs, small neurons have lower detection odds than medium-to-large cells ($p < 0.001$). For the number of detected observations, as shown in Fig. 2 .12d, a linear model fitted to log-transformed density showed that, for medium-to-large DRG, EVs had a lower estimated density than CTB-EVs ($p = 4.53$ x 10-13). For CTB-EVs, small DRG had more signal than medium-to-large DRG ($p = 1.21$ x 10-6). For medium-to-large neurons, CTB-EVs showed greater uptake than EVs.

Overall, CTB-EV injection did not cause foot pad thickening, and we observed no inflammation. Regarding CTB-EVs vs EVs, the two treatments showed no difference in organ distribution. For DRG uptake analysis, the data suggested that although small DRG had more

signal than medium-to-large DRG, medium-to-large DRG with EVs had a lower estimated density than with CTB-EVs

Experimental 4d: eGFP-WGA EVs vs mCherry-EVs (In vivo analysis)

The 4d experiment comparing eGFP-WGA-EVs and mCherry-EVs followed the injection protocol from experiment 4c for eGFP-CTB-EVs and mCherry-EVs. Figure 2.13 shows footpad thickness and biodistribution measurements. Figure 2.13 shows IVIS and confocal microscopy uptake analyses. The results are described below.

First, the footpad thickness comparison across the indicated time points (Figure 8a) was analyzed using a t-test to compare at that timeline to baseline (before injection), and the result showed that on the side injection with WGA-EVs having footpad thickening at 3 hours ($p = 0.039$) and 48 hours ($p = 0.0001$) after injection and on the side injection with EVs having a footpad thickening at 48 hours ($p = 0.039$) and 72 hours ($p= 0.039$) after injection. Both-side injections increased thickness only in the acute timeline.

Second, we assessed biodistribution using IVIS (Fig. 2.13b) to measure the fluorescent intensity ratio relative to the control animal. The results showed no statistically significant difference between organs and treatments (eGFP-WGA-EVs vs mCherry-EVs) ($p = 0.289$).

Next, we analyzed DRG uptake using confocal microscopy (fig 2.13c). We planned to use the binomial model (detected vs. not detected) and the number of detected observations for data analysis in both the eGFP-WGA-EVs vs. mCherry EVs and eGFP-CTB-EVs vs. mCherry EVs experiments because the positive signal was sparse for the eGFP-WGA-EVs vs. mCherry EVs experiment. Because the data were sparse, that is, signal was detected in ~1% of more than 2,000 DRGs sampled, we did not proceed with statistical analysis. We are not confident enough to interpret the data because of the low overall positive signal.

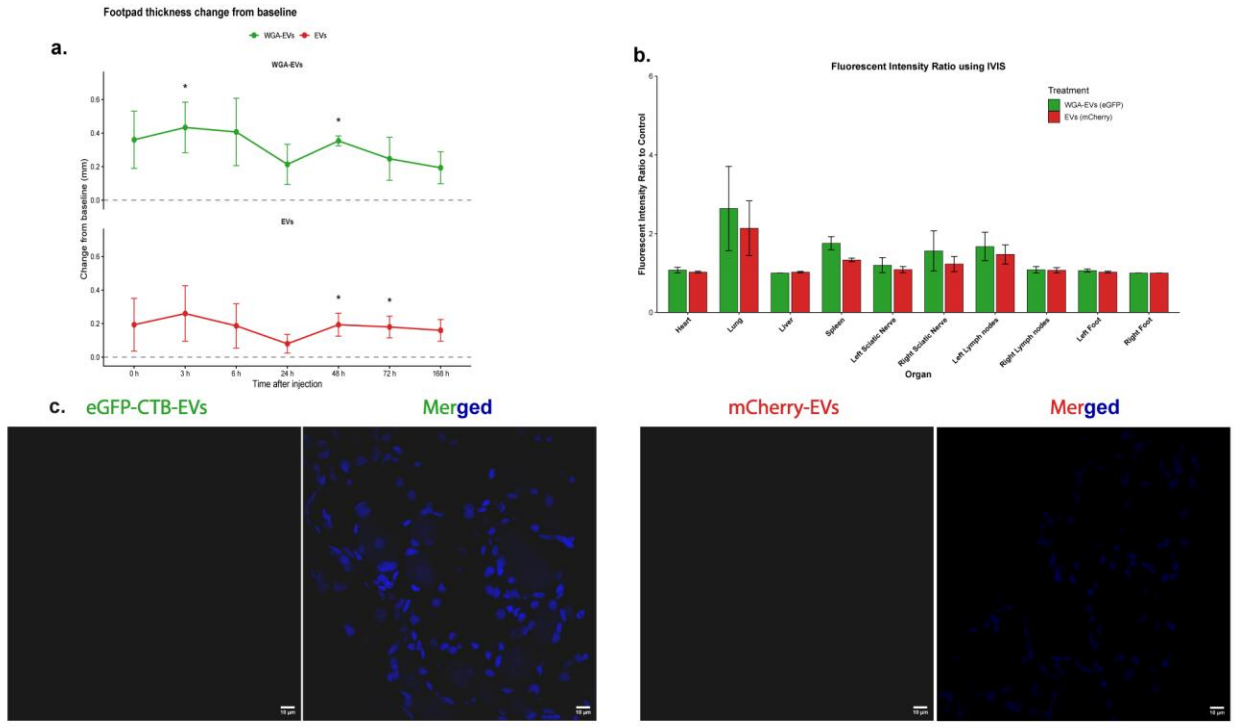


Figure 2.10. WGA-EVs vs EVs uptake analysis in an animal model. (a) Footpad thickness of animals. (b) Analysis using the IVIS system. Note: No statistically significant difference between WGA-EVs and EVs uptake in different organs. (c) Representative confocal microscopy images of mCherry-EVs or eGFP-CTB-EVs in DRG.

Discussion

Here, we evaluated nanoparticle engineering with ligands specific to DRG neurons for uptake. We tested two methods to conjugate ligands to the nanoparticle surface. Both the ABC method using biotin and avidin and the lipid-linking method using DOPH-PEG-NHS successfully conjugated the ligand CTB to EVs. However, the lipid-linking method was more efficient, adding more ligand to the EV particle and enabling preparation of a high concentration of EVs. Using the lipid-linking method, we added WGA and CTB to EV or liposome membranes for comparison. We investigated neural uptake by the engineered particles. In vitro uptake analysis showed that

ACS5004 neural cells took up CTB-EVs more than naive EVs or WGA-EVs, and this pattern was not observed in the HEK 293 non-neural cell line; it also demonstrated a dose-dependent relationship. However, CTB-liposomes, WGA-EVs, or WGA-liposomes did not show the same uptake pattern in neural cells. To further evaluate targeted neural uptake, we assessed DRG labeling after peripheral injection. We found that large DRG neurons took up CTB-EVs, with no evidence of uptake by naïve EVs. We cannot analyze WGA-EVs in an in vivo model. Taken together, these results suggest that EVs with CTB as a ligand enable dose-dependent uptake, regardless of the conjugation method, and may target large DRG neurons after peripheral injections. This work suggests that ligands bound to nanoparticles using the lipid-linking method may affect EV uptake in specific tissues. Still, additional work is needed to identify ligands that enable EV uptake by small DRG neurons.

Using CM from GMP production to generate EVs: Purity and Yield

To transition MSCs and MSC-derived EVs into clinical use, GMP cell culture has moved from 2D to 3D systems. GMP requires greater control of the manufacturing process and optimization of cell yields and medium changes. As a result, MSC and EV yield efficiency increases in 3D [120,121]. Indeed, 3D culture of MSCs increases EV production [121], perhaps due to shear forces incurred in 3D culture [122]. Here, EVs were derived from 3-3L batches of conditioned media (CM) obtained from expanding umbilical cord-derived MSCs, received from the University of Kansas Medical Center stem cell therapy GMP production facility (RS is the facility manager), and stored in aliquots at -80^{o} C until use [118]. The da Silva lab reported scaling up EV production using 3D culture systems, documenting a yield of ~6.9 x 10^{9} EVs/ml of CM starting with 600 mL of CM [123]. In contrast, the yields reported here are 3.71 x 10^{10} ± 1.98 x 10^{10} EV particles per 1 mL CM, starting with 225- 800 mL of CM. Because the MSCs were in the

growth phase over the 6 days of conditioning, we did not calculate the number of EVs released per cell/day. Still, previous estimates by us in 2D culture [118] and by others in 3D culture [122] yielded an estimate of approximately 1.2-3.0 x 10^4 EVs/cell/day. Also, compared with another GMP-level study of MSCs, the highest EV yield was 1.4 x 10^4 particles/cell [124]. Gong et al. reported 3D cell culture in the bioreactor containing 5% HPL in the media for up to 20 days, yielding >5 x 10^8 cells/ batch (PSC-iMSC) and ~1.2 x 10^{13} particles/ day (based on daily harvest with TFF and SEC for EV isolation)[125]. Also, compared with another GMP-level study of MSCs, the highest EV yield was 1.4 x 10^4 particles/cell [124]. Our procedure yielded 2000 mL of CM containing ~5 x 10^9 MSCs and 3.71 x 10^{10} ± 1.98 x 10^{10} EV particles per 1 mL, resulting in an ending yield of 7.42 x 10^{13} ± 3.96 x 10^{13} particles at day 6 (144 hours).

Here, we used TFF to reduce CM volume before SEC in some batches, similar to the isolation method described by [121] because TFF and SEC are scalable methods that can be made GMP-compliant. As reported previously, SEC reduces protein contamination co-isolated during ultracentrifugation-based EV isolation [118]. We calculated sample purity as the number of EVs/µg protein, as suggested by Cliff and Clayton [122,126]. In this schema, a higher purity value indicates lower protein contamination. Three batches of naïve EVs derived from 3D culture of MSCs in the bioreactor had a purity value of about ~3 x 10^9 EVs/µg protein. The value fits at the high end of purity previously reported for MSC-derived EVs isolated by SEC [121,122,127].

Nanoparticle Characterization

Regarding size (based on NTA and DLS) and PDI information for nanoparticles after manipulation, our findings suggested that there were discrepancies in size and PDI due to functionalization with method tagging (ABC method vs. lipid linking method), ligands (CTB and WGA), or loading with fluorescent proteins (mCherry vs. eGFP-CTB). To explain why some

samples appear larger in size and PDI, these naïve EVs with added ligands form a corona, which the NTA and DLS detect as larger particles. Another possibility is that CTB and WGA have different forms, leading to multiple binding sites per molecule that may bridge the two vesicles and promote vesicle clustering/aggregation [128,129]. Fukui et al. reported that CTB-liposomes showed a larger trend than unconjugated liposomes, and Krishnan et al. found that TTC-exosomes increased in size compared to naïve exosomes [2,65]. To explain why modified nanoparticles are smaller, the manipulation step (e.g., sonication or extrusion) may cause large particles to physically break into smaller ones [130,131].

We successfully loaded fluorescent proteins into EVs and confirmed their localization. eGFP can bind to the membrane and be present in the lumen, whereas mCherry associates with the EV membrane only after active loading via sonication. Colja et al. showed successful loading of nanobodies on the EV membrane and inside EVs with sonication. [132]. According to Chen et al., sonication depletes cargo from EVs more effectively than electroporation [133]. To improve loading, you can use cationic lipids commonly used for DNA and RNA transfection [134]. The cationic lipid is reported to be used with supercharged protein (in this case, GFP) to load into EVs successfully [135]. The cationic lipid is reported to be used with supercharged protein (in this case, GFP) to load into EVs successfully [135]. Although both eGFP and mCherry are approximately 28 kDa, their ionizable forms (as measured by isoelectric points) differ, which may contribute to their distinct loading behaviors. To confirm this, we can repeat the experiment at different pH values to alter the ratio of ionized to non-ionized forms. We also did not quantify the fluorescent protein per EV yield. These details will need further clarification in future work.

Several different ligands enable trafficking to the nervous system. Many of these have been used experimentally as neuroanatomical tracers or to enhance delivery of drugs to the CNS

or PNS, which is a well-known challenge. These ligands include antibodies, nanobodies, viral proteins, toxins, aptamers, lectins, and proteins (see the review [136]). Here, we tested WGA and CTB as ligands to target small and medium- to large DRG neurons, respectively, based on previous work using WGA- or CTB-conjugated horseradish peroxidase [1,137]. That work demonstrated that CTB retrogradely labels large and medium-sized NF200+ DRG neurons, and WGA retrogradely labels mostly small CGRP+ DRG neurons, most likely nociceptors [137,138]. One curious observation was that simultaneous injection of both CTB- and WGA- horseradish conjugates did not label either DRG subset [1], suggesting that co-injection prevented uptake by an unknown mechanism.

Both WGA and CTB are thought to be taken up by receptor-mediated endocytosis. CTB binds to GM1 ganglioside, which is found in cholesterol-rich lipid-raft microdomains, and is taken up by clathrin-independent, lipid-raft/caveolae-dependent endocytosis [139,140], but in some cell types, including hippocampal neurons, CTB enters via a clathrin-dependent mechanism [141]. Finally, in motor neurons, CTB enters using an ARF6-dependent pathway [142].

In contrast to CTB, WGA binds N-acetylglucosamine and sialic acid glycoprotein residues and is taken up by receptor-mediated endocytosis via clathrin- and caveolin-dependent pathways [143,144]. We hypothesized that WGA-labeled EVs or liposomes would target nociceptors, and CTB-labeled EVs or liposomes would label non-nociceptor populations, based upon their HRP conjugate preferences. The data partially support the hypothesis. In vitro testing showed that neural ACS 5004 cells preferentially took up CTB-labeled EVs in a dose-dependent manner. Non-neural HEK cells did not take up CTB-EVs more efficiently than naïve EVs. Labeling EVs or liposomes with WGA did not affect their uptake in vitro. We speculate that DRG neurons may have a limit to the size of material they can take up. WGA-labeled EVs may be too large to be taken up.

However, CTB-liposomes are taken up and retrogradely transported when injected into the sciatic nerve [2]. We cannot reconcile these discrepancies here.

Ligand binding methods

We evaluated two methods for attaching the ligand CTB to the EV membrane: ABC and lipid-linking. The ABC method used the strong affinity between avidin and biotin to label the membrane in two steps: EVs were first biotinylated and then incubated with avidin-labeled CTB. This avidin-based method has been proposed for various applications because of its advantages, including stability and affinity, which help amplify the signal because 1 avidin can bind to 4 biotin molecules. The avidin-biotin system has broad applications in the nanoparticle field, as reviewed here. In EVs, this system has been proposed to encapsulate FITC and fabricate gelatin .

In contrast, the lipid-linking method was a one-step approach that had previously functionalized nanoparticles with peptides/proteins using either DSPG or DOPE [145][146]. Here, we found that both methods could functionalize the EV membrane, but for several reasons we used the lipid-linking method in downstream work. First, the ABC method yielded fewer functionalized EVs. Second, the lipid-linking method produced measurable amounts of CTB bound to EVs, while the ABC method did not. Third, the lipid-linking method required fewer steps, simplifying functionalized EV production. Fourth, the lipid-linking method can produce a higher concentration than the ABC method.

We compared tagging efficiency and uptake. Although the ABC method showed less CTB functionalization per EV, as shown by ELISA, uptake followed the same dose-response trend for both methods in neural cell lines based on the number of EVs added to cells. At the same dose of CTB-EVs, adding more CTB to each EV (lipid linking method) did not result in more uptake, perhaps because the “optimal ligand” is more important than the number of CTB per particle and

perhaps because having more receptors per CTB-EV reduces the number of available receptors for uptake of other CTB-EVs [147]. While CTB-liposomes were not successfully internalized, internalization in a neural cell line may be influenced by membrane complexity arising from lipid composition, which varies with different ratios and affects uptake.

Based on MTT analysis, we observed no evidence of cellular toxicity across all cell lines tested with CTB- or WGA-conjugated EVs or liposomes. We observed no statistically significant difference between these conjugates and unconjugated nanoparticles. Across all 7-day observations of footpad thickness after injection, we observed no local swelling at the injection site. This suggests no local inflammation in the acute or chronic phases.

Ligand testing for retrograde transport to DRG after peripheral injection

In vivo analysis showed that CTB-EVs specifically targeted medium- to large-sized neurons in DRG. This supports a study showing that CTB-HRP targets large neurons after sciatic nerve injection [2]. Based on CTB-EV and CTB-liposome experiments, the ligand CTB is not the only factor to consider in cargo development for neuronal targeting; the cargo itself (e.g., lipid composition, natural/synthetic) can also contribute to cellular uptake. A previous study made CTB-liposomes and demonstrated retrograde transport to motor neurons in vitro [16,148]. This work did not examine retrograde transport to the DRG.

We also tested WGA as a ligand for cellular uptake; in vitro analysis showed that neither WGA-EVs nor WGA-liposomes exhibited specificity for a neural cell line or a dose-response. This observation in an in vivo model also showed that WGA-EVs did not undergo retrograde transport to DRG after peripheral injection, or they were not detectable in DRG, since we collected more than 2,000 DRG in total, but only 1% were detected. Based on this, we fitted the in vivo data to both a binomial model and a model for the number of detected observations. However, because

the number of positive signals was too low to proceed, we omitted the data analysis for these experiments. Our results did not align with the previous finding that WGA-HRP injection at the sciatic nerve successfully transported retrograde to small-diameter cells in DRG or passed the blood-brain barrier when coupled with gold nanoparticles after injection via the intradiaphragm [149]. Also, our findings did not support that WGA-HRP-gold nanoparticle (WGA-HRP-AuNP) injection at axonal sites in a microfluidic setting resulted in retrograde transport to cell body sites [150]. Another interesting point, beyond HRP conjugation and nanoparticle type, is that the study timeline was less than 72 hours, compared with 168 hours in our study. This difference in study duration may contribute to differing findings.

Alternative to CTB and WGA

The most "popular" peptide ligand on EVs for brain-targeted therapeutics is Rabies Viral Glycoprotein (RVG) [41]. RVG binds the nicotinic acetylcholine receptor and facilitates EV crossing of the blood-brain barrier [41,151]. Specifically, after systemic injection, RVG-exosomes crossed the blood-brain barrier and targeted neurons, microglia, and oligodendrocytes in the brain [41]. RVG-R9/siRNA can undergo retrograde transport to the DRG [82], but RVG-exosomes crossed the blood-brain barrier and entered the brain in a mouse but did not enter the DRG [152]. No evidence shows that RVG-exosomes traffic to the DRG after peripheral injection. In contrast, peripheral injection of rabies virus infects sensory and motor neurons [153], but rabies virus stains only subsets of DRG neurons, specifically large-diameter, capsaicin-insensitive neurons [154]. Pseudorabies virus can also label motor and sensory pathways after peripheral injections [155]. Similarly, Herpes simplex virus can retrogradely label motor and sensory pathways after peripheral injections [156,157]. Therefore, empty viral envelopes or nanoparticles conjugated to viral

membrane glycoproteins that bind neural membranes may provide targeting ligands to enhance peripheral neural uptake.

Tetanus toxin-C fragment (TTC) is another example of a ligand targeting the PNS [90,158,159]. Tetanus toxin binds to GT1b and GD1b in the presynaptic membrane [160,161]. TTC's function supports this selective uptake and retrograde transport as a neuroanatomical tracer. [162,163]. TTC is useful for specific targeting and for modifying nanoparticles, e.g., exosomes; however, no data show ligand-labeled vesicle uptake by DRG, only motor neurons [65]. TTC was also shown in vitro to enhance uptake by SH-SY5Y and N18-R105 neural cell lines [164]. TTC-functionalized chitosan, PEI, or PEG particles can be taken up and retrogradely transported to the DRG [90,165,166]. In summary, RVG and TTC can be functionalized and effectively target neural membranes, but membrane-bound nanoparticle trafficking to the DRG has not been demonstrated [162,163].

As alternatives to these ligands, pseudorabies virus, herpes simplex virus, and adeno-associated virus 9 (AAV9) have been widely used as vectors to target the CNS and PNS after systemic injection in research and clinical applications [167]. Of these, HSV preferentially labels small-diameter DRG neurons[168].

One possible suggestion for future work, following this work on targeting specific cells, is to test other ligands (e.g., RVG and TTC) to assess retrograde transport after peripheral injection into DRG. Another possibility is to focus on therapeutic applications (e.g., pain, neurodegenerative diseases) with specificity for the desired target organs. Challenges in this work include using a single lipid composition ratio in the experiments and a one-ended study at 168 hours in the in vivo experiment. These suggest that, in the next project, we should vary these parameters to develop an appropriate study protocol.

Chapter 3 - Conclusion

The dorsal root ganglion (DRG) is a collection of sensory neuron cell bodies that transmit various sensations from peripheral organs to the central nervous system. Directly targeting neuronal cell bodies within the DRG can be challenging because the ganglia are located adjacent to the vertebral column. However, their axons project to the periphery, making them an alternative route to access these neurons. Neurotracers or drug delivery systems may be taken up at the periphery and able to undergo retrograde transport to the soma without direct injection into the DRG. To target the DRG, I decided to do the work by using nanoparticles, both natural (EVs) and synthetic (liposomes), for peripheral injection to see whether they can undergo retrograde transport to the soma or not with the two ligands of interest. We hypothesize that CTB targets medium-to-large neurons (> 600 um^2) and WGA targets small neurons (< 600 um^2) after functionalization with EVs and liposomes (CTB-EVs, WGA-EVs, CTB-liposomes, and WGA-liposomes). I organized the dissertation into three chapters: Chapter 1 as the introduction, Chapter 2 as the main experiments (abstract, introduction, materials and methods, results, and discussion), and Chapter 3 as the conclusion. Following this description, I will summarize my Chapter 2 and break it down into details from experiments 1 to 4b.

In Experiments 1a and 1b, I isolated EVs from the GMP-MSC facility and assessed yield and purity across isolation batches. Yield linearly increased with higher starting CM volumes, indicating consistent EV isolation across batches. The purity (particles/protein) of naïve EVs tends to be higher than that of conjugated EVs. This aligns with the Western blot evidence showing successful ligand conjugation to the EVs. I also present EV characterization by Western blot for EV markers and conjugation, NTA and DLS for size, PDI and z-potential, and TEM for EV presence. Overall, CM from the GMP facility provided a valuable resource practicing scaling up

EV isolation, with yield and purity demonstrated and EV presence confirmed by multiple characterization methods. TFF is a commercially scalable method for concentrating CM, and SEC is well-established as a method for isolating high-purity EVs. My work suggests that these methods are scalable and could be validated for producing GMP-grade EVs for clinical translation.

In experiment 2, I demonstrated two conjugation methods: the ABC method (biotinylated EVs with avidin and biotinylated CTB) and the lipid-linking method (EVs with DOPE-PEG-NHS and CTB) to conjugate the ligand (in this case, CTB) to EVs. Both methods successfully tagged EVs with CTB and increased neuronal uptake compared with a non-neuronal cell line across the doses tested. However, given its ease of use and higher yield, I chose the lipid-linking method for subsequent experiments. Taken together, both methods achieved successful conjugation and increased uptake in the neuronal cell line. However, when considering clinical translation, the lipid-linking method should be prioritized for downstream optimization and scaling.

In experiments 3a and 3b, I tested the lipid-linking method with different ligands (WGA) in experiment 3a and with different nanoparticles (liposomes) using both CTB and WGA in experiment 3b. In experiment 3a, although conjugation with WGA-EVs was successful, uptake was not specific to the neural cell line. That is, the ligand did not increase uptake in ACS 5004 as the dose increased. In experiment 3b, CTB-liposomes and WGA-liposomes showed lower uptake than liposomes in the neural cell line. This indicates that the ligands are not the only main criteria to consider for uptake preference and highlights that nanoparticle types may affect cellular accumulation patterns. This may be explained by differences in lipid composition that affect cellular uptake. Considering this, I decided not to test the liposomes in an in vivo model.

In experiments 4a-4d, all experiments were related to the in vivo model. Experiment 4a was a fluorogold (FG) injection analysis to establish the appropriate timeline for the in vivo

experiment. FG showed no difference in the number of positive cells in the DRG between day 5 and day 7 after peripheral injection. This led us to terminate the experiment on day 7 to ensure that, after injection of either CTB-EVs or WGA-EVs, they reach the DRG within the timeline of interest. Then, in the next experiment (4b), for EV preparation, we used eGFP for CTB-EVs or WGA-EVs and mCherry for mCherry-EVs. I showed successful EV loading with fluorescent proteins using sonication, which was the most efficient method I tested. Lastly, in experiments 4c and 4d, I completed the in vivo model to test whether CTB-EVs target medium-to-large DRG neurons compared with naïve EVs, and whether WGA-EVs target small DRG neurons compared with naïve EVs. The results showed that CTB-EVs preferentially target medium-to-large DRG neurons and that this preference is specific. The in vitro model supports the in vivo model of CTB-EV uptake. The WGA-EVs in vitro model showed no specific uptake across cell lines, while the in vivo data were too sparse for analysis. For unknown reasons, differences were found in the background fluorescence between the CTB and WGA in vivo studies. It is possible the elevated background confounded my ability to detect signal in the WGA studies. Further work is needed to resolve the hypothesis that WGA-labeled EVs traffic to small DRG neurons.

In summary, GMP-MSC CM is a useful source for large-scale EV production and can support downstream applications. Both ligands and nanoparticle types affect cellular uptake. The next step is to test variations in lipid composition for synthetic nanoparticles or EVs from different cell lines to assess the potential for higher uptake or cell preference.

Appendix A - Supplemental Materials and Methods

Protein analysis

For SDS-PAGE, the sample was mixed with 4x Bolt™ LDS Sample Buffer (Invitrogen, B0007) and 10x Bolt™ Sample Reducing Agent (Invitrogen, B0004) in distilled water (DW) (Invitrogen, 10977023), and incubated at 70 °C for 10 minutes before electrophoresis on an XCell SureLock™ Mini-Cell (Invitrogen, EI0001) at 200 V constant with Bolt™ Bis-Tris Plus Mini Protein Gels, 12%, 1.0 mm, WedgeWell™ format (Invitrogen, NW00120BOX), using 20x Bolt™ MES running buffer (Invitrogen, B0002) diluted in DW and supplemented with Bolt™ Antioxidant (Invitrogen, BT005). A protein ladder was used as a reference size (Thermo Scientific, 26619). Proteins were transferred overnight at 10 mA from the gels to either a nitrocellulose membrane (Bio-Rad, 162-0097) or a polyvinylidene difluoride (PVDF) membrane (Thermo Scientific, 88518) that had been soaked in 100% methanol for 15 minutes, followed by distilled water for 1 minute for the PVDF membrane. The membrane was blocked with 3% BSA in PBS with 0.05% Tween (PBS-T) at room temperature for 1 hour with gentle rocking. Next, replace the blocking solution with primary antibody at the optimal dilution in PBS-T and incubate at room temperature for 1 hour. After removing the primary antibody, wash the membrane 3 times with PBS-T for 5 minutes each. Next, add the secondary antibody at the optimal dilution in PBS-T and incubate at room temperature for 1 hour. We then removed the secondary antibody and washed the membrane with PBS-T for 5 minutes, 3 times. After the final wash, we localized the proteins using SuperSignal™ West Femto Maximum Sensitivity Substrate (Thermo Scientific, 34095) and visualized them with Azure 600 via enhanced chemiluminescence (ECL) detection on an Azure imager. We captured TIFF images of the blot. Table 1 lists the antibodies.

Modification of EVs and liposomes with CTB or WGA

Calculation Note (modified from [111]):

For 10^{13} nanoparticles, x mg of DOPE-CTB (or DOPE-WGA) is needed

- Molecular Weight (MW) of CTB = 11,600 Da, MW of WGA = 36,000 Da, DOPE-PEG 5000-NHS ≈ 5,000 Da
- 6.023×10^{23} particles of nanoparticles/ mole
- n ligands/EVs = 6,000 Hu et al., 2021 [111]
- Mole (M) of DOPE-WGA = $\frac{6000 \times 10^{13}}{6.023 \times 10^{23}}$ = approx. 10^{-7} M

A) MW (Da) of DOPE-CTB = ~5,000 (DOPE-PEG-NHS) + 11,600 (CTB) = 16,600 Da

- The weight (mass) of DOPE-CTB needed is x mg = M * MW = 10^{-7} x 16600 = 1.66 mg.
- 10^{13} nanoparticles required 1.66 mg of DOPE-CTB, but a 2-fold excess by weight (3.32 mg) was used to increase reaction speed and efficiency.
- A 1:1.5 molar ratio of DOPE-PEG-NHS: CTB was used. We then added 200 µM DOPE-PEG-NHS (1 mg) and 300 µM CTB (3.48 mg).

B) MW (Da) of DOPE-WGA = ~5000 (DOPE-PEG-NHS) + 36,000 (WGA) = 41,000 Da

- The weight (mass) of DOPE-WGA needed is x mg = M * MW = 10^{-7} x 41000 = 4.1 mg
- 10^{13} nanoparticles required 4.1 mg of DOPE-CTB, but a 2-fold excess by weight (8.82 mg) was used to increase reaction speed and efficiency.
- A 1:1.5 molar ratio of DOPE-PEG-NHS: WGA was used. Then, 200 µM DOPE-PEG-NHS (1 mg) and 300 µM CTB (10.8 mg) were used.

Immunofluorescence staining

Slides were allowed to come to room temperature for 20 minutes after removal from -20 °C, then washed 3 times with PBS for 5 minutes each. Slides were permeabilized with PBS with 0.3% Triton X-100 (PBS-Tx for 20 minutes, then washed 3 times with PBS for 5 minutes each. Next, slides were blocked with 5% normal goat serum in PBS-TX (Thermo Fisher, Cat. No. 31872) for 1 hour at room temperature. Slides were incubated with the primary antibody (diluted in blocking buffer) overnight at 4 °C, using 1:1500 rabbit anti-GFP (Abcam, Cat. No. ab 6556) for left-sided organs (eGFP-CTB-EVs or eGFP-WGA-EVs) and 1:500 mouse anti-mCherry Ab (Abcam, Cat. No. ab 125096) for right-sided organs (mCherry-EVs injection site). The following day, slides were washed with 0.05% PBS-TX for 5 minutes, 3 times, then incubated with the secondary antibody (diluted in blocking buffer) for 1 hour at room temperature, using 1:500 Goat anti-Rabbit IgG (H+L) Highly Cross-Adsorbed Secondary Antibody, Alexa Fluor™ Plus 488 (Invitrogen, Cat. No. A32731) for eGFP detection and 1:1000 Goat anti-Mouse IgG (H+L) Highly Cross-Adsorbed Secondary Antibody, Alexa Fluor™ Plus 594 (Invitrogen, Cat. No. A32742) for mCherry detection. After counterstaining with DAPI, slides were coverslipped with a #1.5 coverglass using ProLong™ Glass Antifade Mountant (Thermo Fisher, Cat. No. P36980) and observed under a confocal microscope (Carl Zeiss, LSM-880).

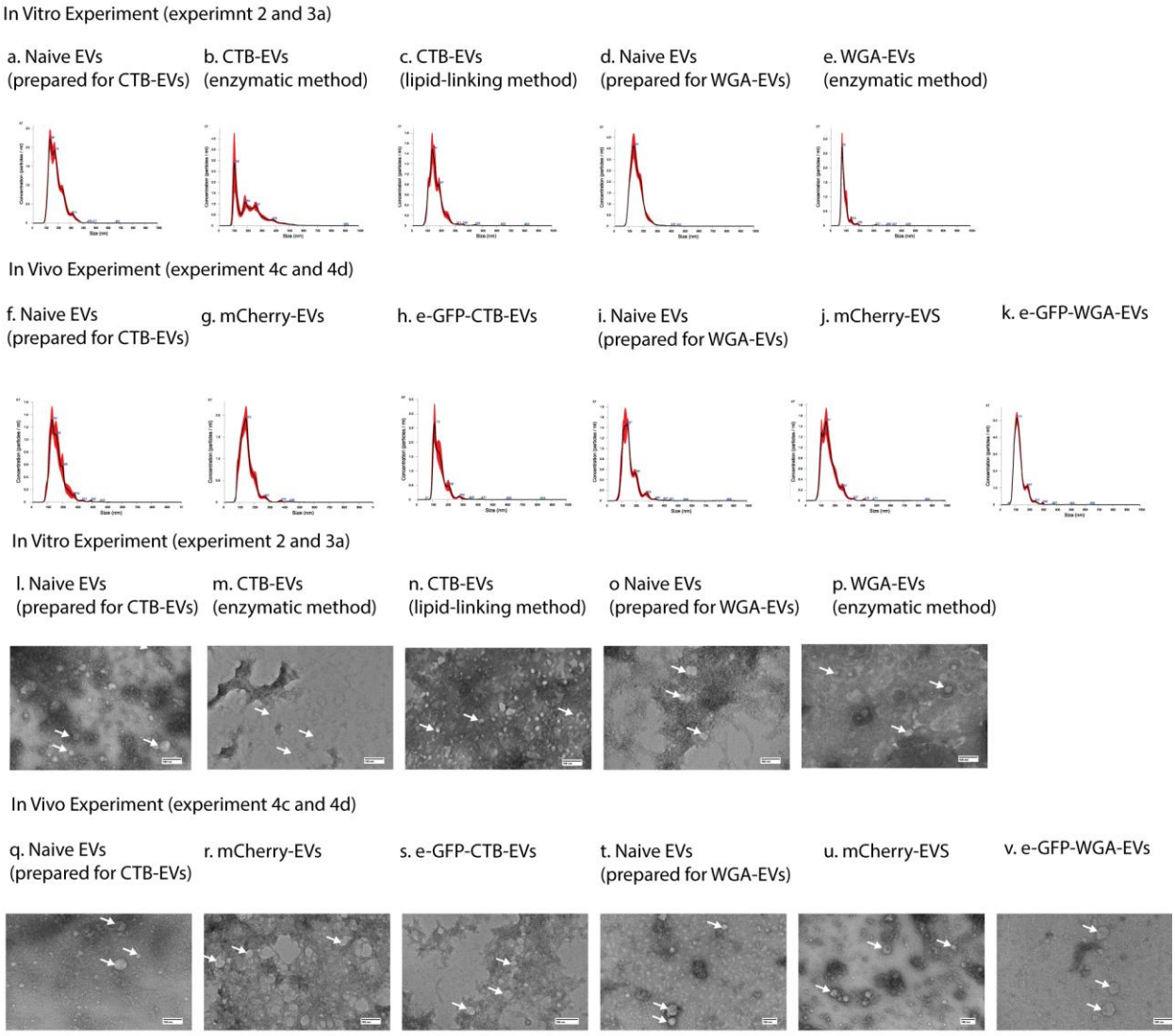
Table 1: List of antibodies used for immunoblotting and immunofluorescence assay

Detection	Antibody	Company, Cat. No.	Dilution
CD 9	Human CD 9 (C-4)	Santa Cruz Biotechnology, sc-13118, mouse mAB, IgG1k	1:1,000
CD 63	Human CD 63(MX-49.129.6)	Santa Cruz Biotechnology, sc-5275, mouse mAB, IgG1 k	1:1,000

CD 81	Human CD81 (1.3.3.22)	Santa Cruz Biotechnology, sc-7637, mouse mAB, IgG1 k	1:1,000
β-actin	Human β-actin (C4)	Santa Cruz Biotechnology, sc-47778, mouse mAB, IgG1 k	1:1,000
CTB	Anti-Cholera Toxin, B-subunit	Sigma-Aldrich, 227040, goat polyclonal, IgG	1:2,000
	Anti-Cholera toxin, B subunit (CTXB)	Sigma-Aldrich, SAB4200844-100 µL, mouse mAB, IgG1	1:200
WGA	Anti-WGA	Abcam, ab178444, rabbit polyclonal, IgG	1:500
eGFP	Anti-GFP antibody	Abcam, ab6556, rabbit polyclonal, IgG	1:1,500
mCherry	Anti-mCherry antibody (1C51)	Abcam, ab125096, mouse mAB, IgG2a	1:500
Goat IgG (H+L)	donkey anti-goat IgG (H+L) Secondary Ab, HRP	Invitrogen, A15999, donkey polyclonal, IgG (H+L)	1:2,000
mouse IgG_1, IgG_{2a} and IgG_{2b} immunoglobulins	m-IgG Fc BP-HRP	Santa Cruz Biotechnology, sc-525409, mouse IgG Fc conjugated to horseradish peroxidase	1:2,000
rabbit IgG secondary antibody	Mouse anti-rabbit IgG-HRP	Santa Cruz Biotechnology, sc-2357, mouse mAb, IgG	1:1,000

		conjugated to horseradish peroxidase	

Appendix B - Supplementary Figures and Tables



Appendix Figure B.1. EV characterization using NTA and TEM

NTA was used to determine EV particle concentration and size distribution. TEM confirmed the presence of EVs in the samples. **NTA:** Samples for experiments 2 and 3a (in vitro experiments): (a) EVs (batch-prepared for CTB-EVs with ABC method and lipid-linking method experiment), (b) CTB-EVs ABC method preparation, (c) CTB-EVs lipid-linking method preparation, (d) EVs (batch-prepared for WGA-EVs with lipid-linking method), (e) WGA-EVs. Samples for experimental 4c (in vivo experiment): (f) EVs, (g) mCherry-EVs, (h) eGFP-CTB-EVs. Samples for experimental 4d (in vivo experiment): (i) EVs, (j) mCherry-EVs, and (k) eGFP-WGA-EVs.

TEM: Samples for experiments 2 and 3a (in vitro experiments): (l) EVs (batch-prepared for CTB-EVs), (m) CTB-EVs ABC method preparation, (n) CTB-EVs lipid-linking method, (o) EVs (batch-prepared for WGA-EVs), (p) WGA-EVs lipid-linking method preparation. Samples for experimental 4c (in vivo experiment): (q) EVs, (r) mCherry-EVs, (s) eGFP-CTB-EVs. Samples for experimental 4d (in vivo experiment): (t) EVs, (u) mCherry-EVs, and (v) eGFP-WGA-EVs. (Bar scale = 100 nm)

Appendix Table B.1. Physicochemical characterization of EVs (experiments 2 and 3a (in vitro experiments))

Parameters	Naïve EVs (Batch prepared for experiment 2)	CTB-EVs (ABC method)	CTB-EVs (lipid-linking method)	Naïve EVs (Batch prepared for experiment 3a)	WGA-EVs (lipid-linking method)
NTA (mean± SD, mode ± SD)	185.3 ± 2.3, 143.0 ± 7.0	223.1 ± 17.1, 141.5 ± 33.2	165.9 ± 2.3, 142.1 ± 3.7	155.8 ± 1.6, 130.8 ± 3.7	95.6 ± 3.4, 78.4 ± 1.1
DLS (nm) (mean ± SD)	146.0 ± 0.85	665.3 ± 29.07	169.6 ± 10.08	169.5 ± 8.8	6164 ± 1074.0
PDI (mean ± SD)	0.23 ± 0.01	0.56 ±0.09	0.26 ± 0.02	0.30 ± 0.00	0.41 ± 0.23
ZP (mV) (mean ± SD)	-16.09 ± 2.34	-17.56 ± 1.92	-4.28 ± 1.66	-11.13 ± 1.23	-7.84 ± 2.31

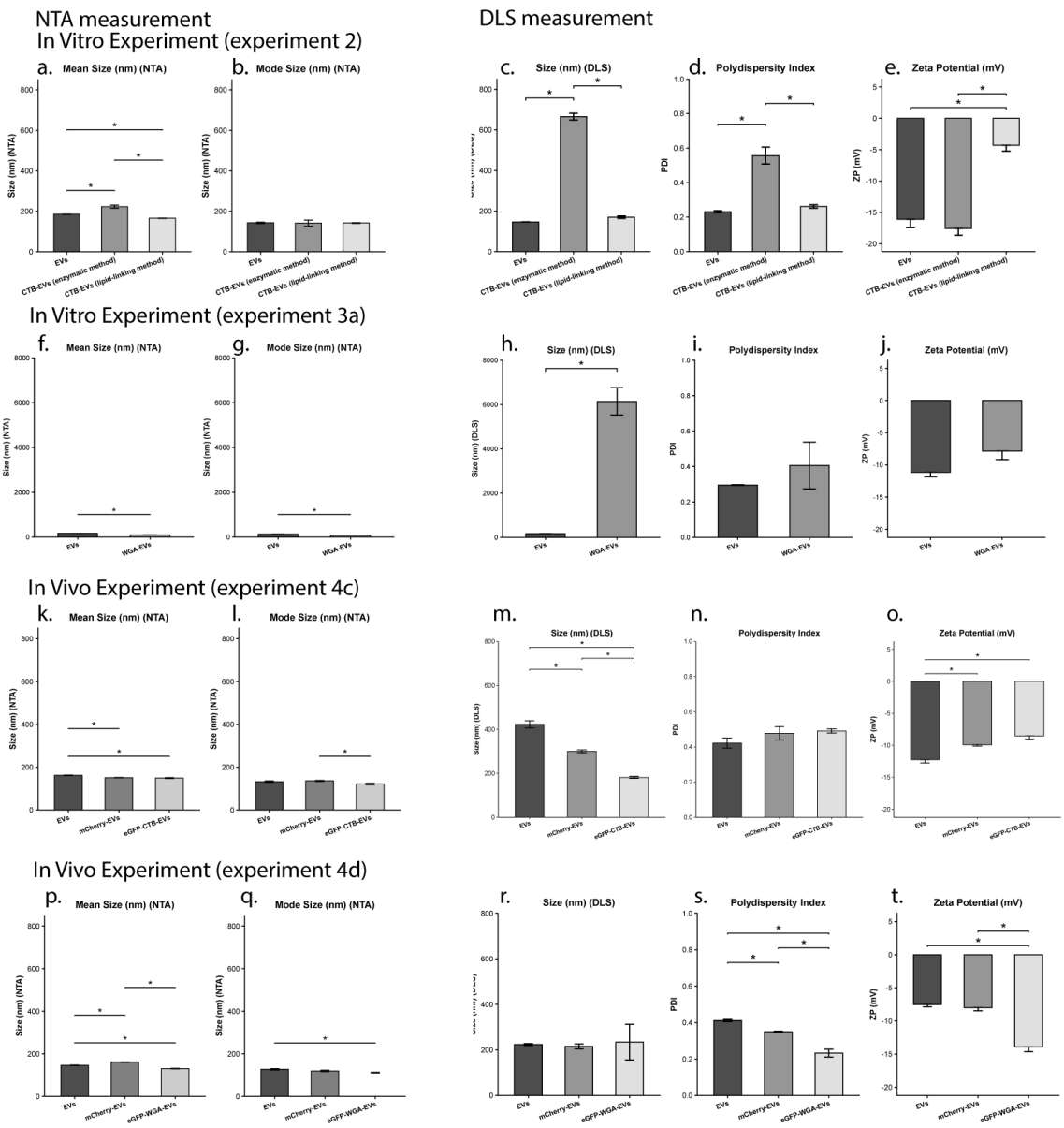
We characterized samples for experiments 2 (conjugation methods) and 3a (lipid-linking method for WGA-EVs) (in vitro experiments) and prepared them separately for exp 2 and exp 3a. We prepared one batch of CTB-EVs using the ABC or lipid-linking method and another batch of WGA-EVs using the lipid-linking method. We measured nanoparticle tracking analysis (NTA), Dynamic Light Scattering (DLS), Polydispersity Index (PDI), and Zeta Potential (ZP). NTA measured particle size as mean ± SD (n=5) ranging from 95.6 ± 3.4 nm to 223.1 ± 17.1 nm, and mode ± SD (n=5) ranging from 78.4 ± 1.1 nm to 143.0 ± 7.0 nm. DLS-measured particle size (n=3)

ranged from 146.0 ± 0.85 nm to 6164 ± 1074.0 nm. PDI (n=3) ranged from 0.23 ± 0.01 to 0.56 ± 0.09. ZP (n=3) ranged from -4.28 ± 1.66 mV to -17.56 ± 1.92 mV.

Appendix Table B.2. Physicochemical characterization of EVs (experiments 4c and 4d (in vivo experiments))

Parameters	EVs (Batch prepared for experiment 4b)	mCherry-EVs	eGFP-CTB-EVs	EVs (Batch prepared for experiment 4c)	mCherry-EVs	eGFP-WGA-EVs
NTA(mean± SD, mode ± SD)	162.1 ± 3.3, 132.8 ± 6.9	151.1 ± 1.9 , 136.1 ± 4.9	149.2 ± 3.8. 121.7 ± 7.7	146.2 ± 2.8, 127.5 ± 7.0	161.2 ± 1.6, 119.7 ± 7.2	130.8 ± 1.9, 112 ± 3.4
DLS (nm) (mean ± SD)	422.87 ± 28.40	299.97 ± 11.57	181.50 ± 8.47	223.8 ± 7.63	215.63 ± 19.11	234.09 ± 136.09
PDI (mean ± SD)	0.42 ± 0.05	0.48 ± 0.07	0.49 ± 0.02	0.41 ± 0.01	0.35 ± 0.00	0.23 ± 0.04
ZP (mV) (mean ± SD)	-12.25 ± 1.24	-9.91 ± 0.48	-8.52 ± 1.24	-7.51 ± 0.88	-7.98 ± 1.21	-13.92 ± 1.77

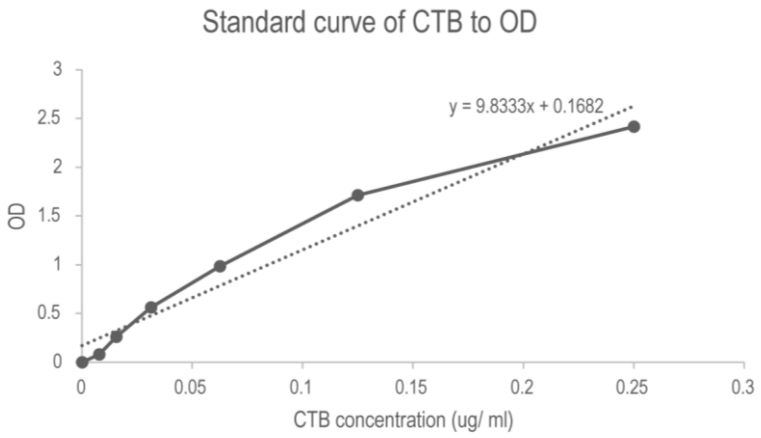
Samples for experiments 4c (eGFP-CTB-EVs vs mCherry (in vivo experiment)) and 4d (eGFP-CTB-EVs vs mCherry (in vivo experiment)) were characterized; samples were prepared separately for exp. 4c and exp 4d. We also prepared 2 batches of naïve EVs. The first batch was for mCherry-EVs and eGFP-CTB-EVs, and the second batch was for mCherry-EVs and eGFP-WGA-EVs. We measured NTA, DLS, PDI, and ZP. NTA measured particle size as mean ± SD (n=5) ranging from 130.8 ± 1.9 nm to 162.1 ± 3.3 nm, and mode ± SD (n=5) ranging from 112 ± 3.4 nm to 136.1 ± 4.9 nm. DLS-measured particle size (mean ± SD; n=3) ranged from 181.50 ± 8.47 nm to 422.87 ± 28.40 nm. PDI (mean ± SD; n=3) ranged from 0.23 ± 0.04 to 0.49 ± 0.02. ZP with a mean ± SD (n=3) ranging from -7.51 ± 0.88 mV to -13.92 ± 1.77 mV



Appendix Figure B.2. Measurement of EV samples: mean and mode size by NTA and mean size, PDI, and Z-potential by DLS.

Samples shown here are EVs conjugated using different methods and ligands for both in vitro (exp. 2 and 3a) and in vivo (exp. 4c and 4d) experiments. NTA Mean (a, f, k, p) and mode size (b, g, l, q), DLS mean size (c, h,m, r), PDI (d, I, n, s), and z-potential (e, j, o, t) were compared. (a-e) Samples for experiment 2 (EVs and CTB-EVs) using the ABC and lipid-linking methods. Note: EVs conjugated with CTB, regardless of method, showed a larger mean size (NTA) but no mode. DLS showed larger sizes for the ABC method than for unconjugated EVs; CTB-EVs conjugated

by lipid-linking were not statistically different from naïve EVs. PDI was higher for the ABC method but not for the lipid-linking method. ZP was more positive for the lipid-linking method conjugation. (f-j) Samples for experiment 3a (EVs and WGA-EVs). Note: WGA conjugation did not change the mean or mode size by NTA compared to unconjugated EVs, but DLS showed a larger mean. PDI and Z-potential remained unchanged after conjugation. (k-o) samples for experiment 4c (EVs, mCherry-EVs, and eGFP-CTB-EVs). Note: NTA showed that naïve EVs had a mean size of 162.1 ± 3.3 nm and a mode size of 132.8 ± 6.9 nm. DLS showed a size of 422.87 ± 28.40 nm, a PDI of 0.42 ± 0.05, and a ZP of -12.25 ± 0.1.24 mV. After sample preparation as mCherry-EVs and eGFP-CTB-EVs, NTA showed smaller mean sizes of 151.1 ± 1.9 nm ($p = 3.16 \times 10^{-4}$) and 149.2 ± 3.8 nm ($p = 7.32 \times 10^{-5}$), and mode sizes of 136.1 ± 4.9 nm and 121.7 ± 7.7 nm with no statistically significant difference from naïve EVs, respectively. DLS showed sizes of 299.97 ± 11.57 nm (p = 0.0004) and 181.50 ± 4.87 nm (p = 0.005), respectively. The PDI was 0.48 ± 0.07 (p = 0.41) and 0.49 ± 0.02 (p = 0.27), respectively, and neither differed significantly from Naïve EVs. The ZP was -9.91 ± 0.48 mV (p = 0.004) and -8.52 ± 1.24 mV ($p = 5.13 \times 10^{-5}$), both statistically significantly different from Naïve EVs. (p-t) samples for experiment 4d (EVs, mCherry-EVs, and eGFP-WGA-EVs). Note: NTA showed that naïve EVs had a mean size of 146.2 ± 2.8 nm and a mode size of 127.5 ± 7.0 nm. DLS showed a size of 223.8 ± 4.41 nm, a PDI of 0.41 ± 0.01, and a ZP of -7.51 ± 0.36 mV. After sample preparation as mCherry-EVs and eGFP-WGA-EVs, NTA showed mean sizes of 161.2 ± 1.6 nm ($p = 3.64 \times 10^{-7}$) and 130.8 ± 1.9 nm ($p = 2.72 \times 10^{-7}$), and mode sizes of 119.7 ± 7.2 nm (p = 0.15) and 112 ± 3.4 nm (p=0.004), respectively. DLS showed sizes of 215.63 ± 19.11 nm and 234.09 ± 136.09 nm (p = 0.96), respectively. The PDI was 0.35 ± 0.00 (p = 0.04) and 0.23 ± 0.04 (p = 0.002), respectively. The ZP was -7.98 ± 1.21 mV (p = 0.82) and -13.92 ± 1.77 mV (p = 0.004), respectively.



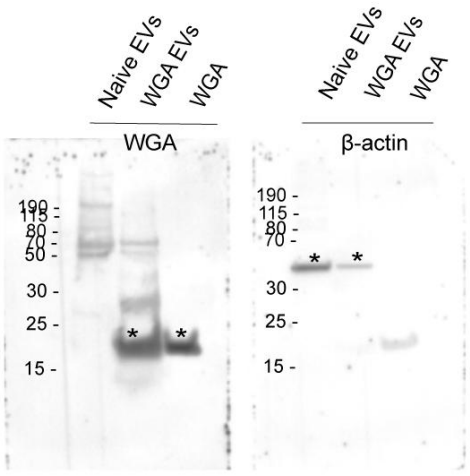
Appendix Figure B.3. CTB control standard curve and quantification.

CTB was plated in a 2-fold dilution series with varying primary antibody concentrations and a fixed secondary antibody concentration to generate the standard curve. The 2-fold serial dilution of CTB ranged from 0.0078125 µg/mL to 0.125 µg/mL. The dashed line represents the linear regression model used for sample interpolation. Note: y = 13.823x + 0.0422 (x = CTB concentration (µg/mL), y = OD), R^2 = 0.9885. CTB protein was undetectable using the ABC method, but the lipid-linking method showed 0.213 pg of CTB per 10^6 EV particles.

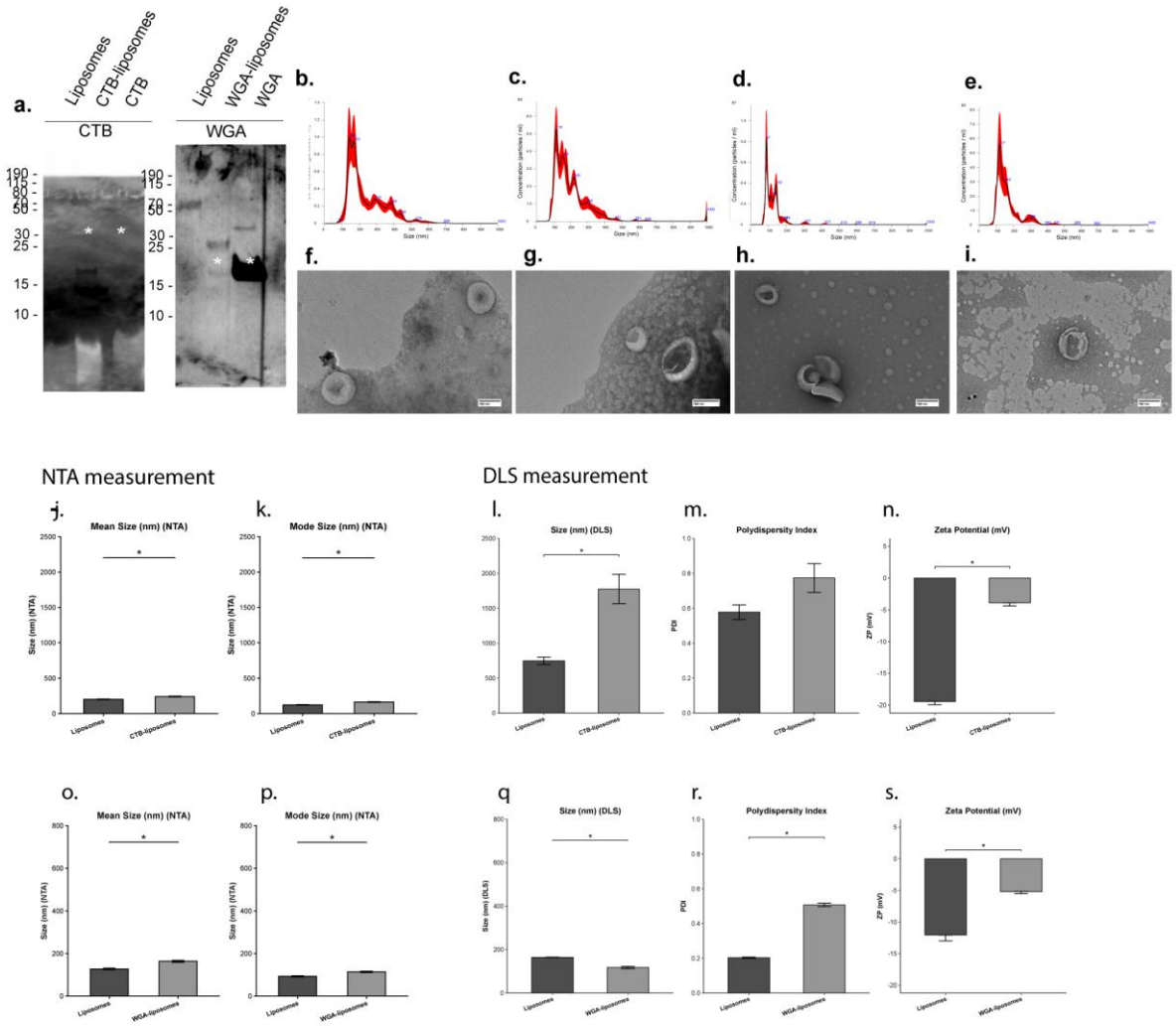
Appendix Table B.3. **Physicochemical characterization of liposomes (experiment 3b)**

Parameters	Liposomes (batch prepared for CTB-liposomes)	CTB-liposomes	Liposomes (batch prepared for WGA-liposomes)	WGA-liposomes
NTA (mean± SD, mode ± SD)	199.1 ± 7.7, 121.8 ± 6.1	239.3 ± 12.2, 161.0 ± 8.5	127.5 ± 6.6, 92.8 ± 5.5	163.6 ± 8.9, 114.0 ± 6.0
DLS (nm) (mean ± SD)	747.8 ± 91.3	1775.3 ± 365.1	164.5 ± 1.8	117.7 ± 8.9
PDI (mean ± SD)	0.58 ± 0.1	0.77 ± 0.1	0.20 ± 0.01	0.51 ± 0.02
ZP (mV) (mean ± SD)	-19.43 ± 0.86	-3.89 ± 0.84	-12.08 ± 1.57	-5.19 ± 0.59

Samples for experiments 3b (lipid-linking method for liposomes, CTB-liposomes, and WGA-liposomes); 2 batches of liposomes were prepared separately, one for CTB-liposomes and another for WGA-liposomes. We measured NTA, DLS, PDI, and ZP. NTA measured particle size as mean ± SD (n=5), ranging from 127.5 ± 6.6 nm to 239.3 ± 12.2 nm, and mode ± SD (n=5), ranging from 92.8 ± 5.5 nm to 161.0 ± 8.5 nm. DLS-measured particle size (n=3) ranged from 117.7 ± 8.9 nm to 1775.3 ± 365.1 nm. PDI (n=3) ranged from 0.20 ± 0.01 to 0.77 ± 0.1. ZP (n=3) ranged from -3.89 ± 0.84 mV to -19.43 ± 0.86 mV.



Appendix Figure B.4. Western Blot of WGA detection. After EV conjugation with WGA using the lipid-linking method, WGA-EVs were positive for WGA.

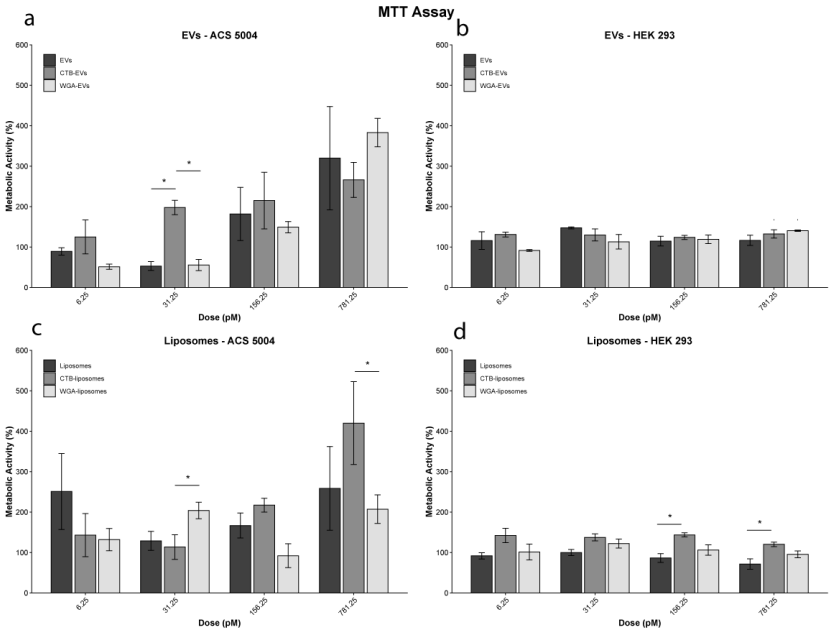


Appendix Figure B.5. Liposome characterizations. (experiment 3b)

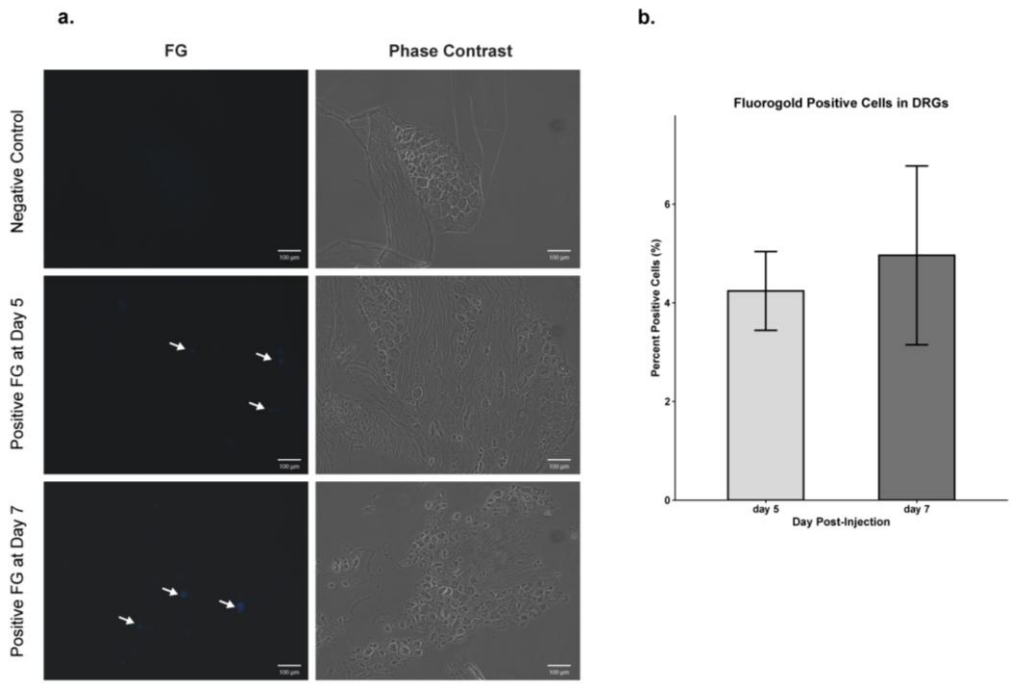
The samples shown here are liposomes conjugated with different ligands for the in vitro experiment (experiment 3b). (a) Western blot detection of CTB and WGA. After liposome conjugation with CTB, CTB-liposomes were positive for CTB. After liposome conjugation with WGA, WGA- liposomes were positive for WGA. (b) NTA of liposomes, (c) NTA of CTB-liposomes, (d) NTA of liposomes, (e) NTA of WGA-liposomes, (f) TEM of liposomes, (g) TEM of CTB-liposomes, (h) TEM of liposomes, and (i) TEM of WGA-liposomes. NTA measurements: mean (j, o) and mode size (k, p), DLS mean size (l, q), PDI (m, r), and z-potential (n, s) were compared. (j- n) samples for liposomes and CTB-liposomes. (o-s) samples for liposomes and WGA-liposomes

Nanoparticle tracking analysis (NTA) was used to determine particle concentration and size distribution for in vitro experiment samples (experiment 3b) (b) liposomes (batch-prepared for

CTB-liposomes), (c) CTB-liposomes, (d) liposomes (batch-prepared for WGA-liposomes), (e) WGA-liposomes. Transmission Electron Microscopy (TEM) was used for imaging of in vitro experimental samples in (f) liposomes (batch-prepared for CTB- liposomes), (g) CTB-liposomes, (h) liposomes (batch-prepared for WGA-liposomes), and (i) WGA-liposomes. (k) NTA measurement for the mean and mode of liposome particle size. (x) DLS measurement for size, PDI, and Z-potential.



Appendix Figure B.6. Dose-response effects of EVs, CTB-EVs, WGA-EVs, liposomes, CTB-liposomes, and WGA-liposomes on ACS5004 or HEK293 cell proliferation, as measured by the MTT assay. (a) EVs in ACS 5004 cells. (b) EVs in HEK 293 cells. No trend or significance was observed across all doses, treatments, and cell lines. (c) Liposomes in ACS 5004 cells. (b) Liposomes in HEK 293 cells. No trend or significance was observed across all doses, treatments, and cell lines.



Appendix Figure B.7. Uptake of Fluorogold (FG) in Dorsal Root Ganglia (DRG). (a) Representative fluorescent microscopy images of negative controls and FG detection on days 5 and 7 after injection. (b) Quantitative analysis of FG detection on days 5 and 7 after injection. No difference in the % of FG-positive cells across days after injection. (Calibration bar = 100 µm, brightness and contrast adjusted)

References

1. Liu, H.; Llewellyn-Smith, I.J.; Basbaum, A.I. Co-injection of wheat germ agglutinin-HRP and choleragenoid-HRP into the sciatic nerve of the rat blocks transganglionic transport. *J Histochem Cytochem* **1995**, *43*, 489-495, doi:10.1177/43.5.7730587.
2. Fukui, T.; Tateno, H.; Nakamura, T.; Yamada, Y.; Sato, Y.; Iwasaki, N.; Harashima, H.; Kadoya, K. Retrograde Axonal Transport of Liposomes from Peripheral Tissue to Spinal Cord and DRGs by Optimized Phospholipid and CTB Modification. *International Journal of Molecular Sciences* **2022**, *23*, 6661, doi:10.3390/ijms23126661.
3. Berta, T.; Strong, J.A.; Zhang, J.M.; Ji, R.R. Targeting dorsal root ganglia and primary sensory neurons for the treatment of chronic pain: an update. *Expert Opin Ther Targets* **2023**, *27*, 665-678, doi:10.1080/14728222.2023.2247563.
4. Haberberger, R.V.; Barry, C.; Dominguez, N.; Matusica, D. Human Dorsal Root Ganglia. *Frontiers in Cellular Neuroscience* **2019**, *13*, doi:10.3389/fncel.2019.00271.
5. Scroggs, R.S.; Todorovic, S.M.; Anderson, E.G.; Fox, A.P. Variation in IH, IIR, and ILEAK between acutely isolated adult rat dorsal root ganglion neurons of different sizes. *J Neurophysiol* **1994**, *71*, 271-279, doi:10.1152/jn.1994.71.1.271.
6. Lawson, S.N. Phenotype and Function of Somatic Primary Afferent Nociceptive Neurones with C-, Adelta- or Aalpha/beta-Fibres. *Exp Physiol* **2002**, *87*, 239-244, doi:10.1113/eph8702350.
7. Harper, A.A.; Lawson, S.N. Conduction velocity is related to morphological cell type in rat dorsal root ganglion neurones. *J Physiol* **1985**, *359*, 31-46, doi:10.1113/jphysiol.1985.sp015573.
8. Meltzer, S.; Santiago, C.; Sharma, N.; Ginty, D.D. The cellular and molecular basis of somatosensory neuron development. *Neuron* **2021**, *109*, 3736-3757, doi:10.1016/j.neuron.2021.09.004.
9. Middleton, S.J.; Perez-Sanchez, J.; Dawes, J.M. The structure of sensory afferent compartments in health and disease. *J Anat* **2022**, *241*, 1186-1210, doi:10.1111/joa.13544.
10. Usoskin, D.; Furlan, A.; Islam, S.; Abdo, H.; Lonnerberg, P.; Lou, D.; Hjerling-Leffler, J.; Haeggstrom, J.; Kharchenko, O.; Kharchenko, P.V.; et al. Unbiased classification of sensory neuron types by large-scale single-cell RNA sequencing. *Nat Neurosci* **2015**, *18*, 145-153, doi:10.1038/nn.3881.
11. Li, C.L.; Li, K.C.; Wu, D.; Chen, Y.; Luo, H.; Zhao, J.R.; Wang, S.S.; Sun, M.M.; Lu, Y.J.; Zhong, Y.Q.; et al. Somatosensory neuron types identified by high-coverage single-cell RNA-sequencing and functional heterogeneity. *Cell Res* **2016**, *26*, 83-102, doi:10.1038/cr.2015.149.
12. Wang, K.; Cai, B.; Song, Y.; Chen, Y.; Zhang, X. Somatosensory neuron types and their neural networks as revealed via single-cell transcriptomics. *Trends Neurosci* **2023**, *46*, 654-666, doi:10.1016/j.tins.2023.05.005.
13. Tong, Y.G.; Wang, H.F.; Ju, G.; Grant, G.; Hokfelt, T.; Zhang, X. Increased uptake and transport of cholera toxin B-subunit in dorsal root ganglion neurons after peripheral axotomy: possible implications for sensory sprouting. *J Comp Neurol* **1999**, *404*, 143-158, doi:10.1002/(SICI)1096-9861(19990208)404:2<143::AID-CNE1>3.0.CO;2-#.

14. Robertson, B.; Arvidsson, J. Transganglionic transport of wheat germ agglutinin-HRP and choleragenoid-HRP in rat trigeminal primary sensory neurons. *Brain Res* **1985**, *348*, 44-51, doi:10.1016/0006-8993(85)90357-9.
15. Mantilla, C.B.; Zhan, W.Z.; Sieck, G.C. Retrograde labeling of phrenic motoneurons by intrapleural injection. *J Neurosci Methods* **2009**, *182*, 244-249, doi:10.1016/j.jneumeth.2009.06.016.
16. Gonzalez Porras, M.A.; Durfee, P.; Giambini, S.; Sieck, G.C.; Brinker, C.J.; Mantilla, C.B. Uptake and intracellular fate of cholera toxin subunit b-modified mesoporous silica nanoparticle-supported lipid bilayers (aka protocells) in motoneurons. *Nanomedicine* **2018**, *14*, 661-672, doi:10.1016/j.nano.2018.01.002.
17. Gonatas, N.K.; Harper, C.; Mizutani, T.; Gonatas, J.O. Superior sensitivity of conjugates of horseradish peroxidase with wheat germ agglutinin for studies of retrograde axonal transport. *J Histochem Cytochem* **1979**, *27*, 728-734, doi:10.1177/27.3.90065.
18. Schwab, M.E.; Javoy-Agid, F.; Agid, Y. Labeled wheat germ agglutinin (WGA) as a new, highly sensitive retrograde tracer in the rat brain hippocampal system. *Brain Res* **1978**, *152*, 145-150, doi:10.1016/0006-8993(78)90140-3.
19. C., L.C.; Kapadia, S.; Shapiro, C.M. Central Projections of the Sciatic, Saphenous, Median, and Ulnar Nerves of the Rat Demonstrated by Transganglionic Transport of Choleragenoid-HRP (B-HRP) and Wheat Germ Agglutinin-HRP (WGA-HRP). *J Comp Neurol* **1991**, *311*, 546-562, doi:doi.org/10.1002/cne.903110409Digital Object Identifier (DOI).
20. Kuo, Y.C.; Lin, C.Y.; Li, J.S.; Lou, Y.I. Wheat germ agglutinin-conjugated liposomes incorporated with cardiolipin to improve neuronal survival in Alzheimer's disease treatment. *Int J Nanomedicine* **2017**, *12*, 1757-1774, doi:10.2147/IJN.S128396.
21. Gurung, S.; Perocheau, D.; Touramanidou, L.; Baruteau, J. The exosome journey: from biogenesis to uptake and intracellular signalling. *Cell Commun Signal* **2021**, *19*, 47, doi:10.1186/s12964-021-00730-1.
22. Lundy, D.J.; Chau, Z.L.; Chen, S.Y.; Fujisawa, N.; Hill, J.J.; Hsu, B.M.; Liu, J.K.; Mai, K.W.; Lai, J.J. Beyond Extracellular Vesicle (EV) Hype: Practical Solutions and Remaining Hurdles in EV Research, Manufacturing, and Clinical Translation. *Adv Sci (Weinh)* **2026**, *13*, e21913, doi:10.1002/advs.202521913.
23. Nsairat, H.; Khater, D.; Sayed, U.; Odeh, F.; Al Bawab, A.; Alshaer, W. Liposomes: structure, composition, types, and clinical applications. *Heliyon* **2022**, *8*, e09394, doi:10.1016/j.heliyon.2022.e09394.
24. Luo, M.F.; Oomah, B.D.; Akoetey, W.; Zhang, Y.Q.; Daneshfozoun, H.; Hosseinian, F. Liposomes as sustainable delivery systems in food, cosmetic, and pharmaceutical applications. *J Am Oil Chem Soc* **2025**, *102*, 547-568, doi:10.1002/aocs.12907.
25. Pande, S. Liposomes for drug delivery: review of vesicular composition, factors affecting drug release and drug loading in liposomes. *Artif Cells Nanomed Biotechnol* **2023**, *51*, 428-440, doi:10.1080/21691401.2023.2247036.
26. Gatto, M.S.; Johnson, M.P.; Najahi-Missaoui, W. Targeted Liposomal Drug Delivery: Overview of the Current Applications and Challenges. *Life (Basel)* **2024**, *14*, doi:10.3390/life14060672.
27. Kang, M.; Jordan, V.; Blenkiron, C.; Chamley, L.W. Biodistribution of extracellular vesicles following administration into animals: A systematic review. *J Extracell Vesicles* **2021**, *10*, e12085, doi:10.1002/jev2.12085.

28. Liu, Q.; Huang, J.; Xia, J.; Liang, Y.; Li, G. Tracking tools of extracellular vesicles for biomedical research. *Front Bioeng Biotechnol* **2022**, *10*, 943712, doi:10.3389/fbioe.2022.943712.
29. Ulpiano, C.; da Silva, C.L.; Monteiro, G.A. Bioengineered Mesenchymal-Stromal-Cell-Derived Extracellular Vesicles as an Improved Drug Delivery System: Methods and Applications. *Biomedicines* **2023**, *11*, 1231, doi:10.3390/biomedicines11041231.
30. Li, X.; Wei, Y.; Zhang, Z.; Zhang, X. Harnessing genetically engineered cell membrane-derived vesicles as biotherapeutics. *Extracell Vesicles Circ Nucl Acids* **2024**, *5*, 44-63, doi:10.20517/evcna.2023.58.
31. Andreu, Z.; Yanez-Mo, M. Tetraspanins in extracellular vesicle formation and function. *Front Immunol* **2014**, *5*, 442, doi:10.3389/fimmu.2014.00442.
32. Welsh, J.A.; Goberdhan, D.C.I.; O'Driscoll, L.; Buzas, E.I.; Blenkiron, C.; Bussolati, B.; Cai, H.; Di Vizio, D.; Driedonks, T.A.P.; Erdbrugger, U.; et al. Minimal information for studies of extracellular vesicles (MISEV2023): From basic to advanced approaches. *J Extracell Vesicles* **2024**, *13*, e12404, doi:10.1002/jev2.12404.
33. Rubinstein, E.; Le Naour, F.; Lagaudriere-Gesbert, C.; Billard, M.; Conjeaud, H.; Boucheix, C. CD9, CD63, CD81, and CD82 are components of a surface tetraspan network connected to HLA-DR and VLA integrins. *Eur J Immunol* **1996**, *26*, 2657-2665, doi:10.1002/eji.1830261117.
34. Wiklander, O.P.B.; Mamand, D.R.; Mohammad, D.K.; Zheng, W.; Jawad Wiklander, R.; Sych, T.; Zickler, A.M.; Liang, X.; Sharma, H.; Lavado, A.; et al. Antibody-displaying extracellular vesicles for targeted cancer therapy. *Nat Biomed Eng* **2024**, *8*, 1453-1468, doi:10.1038/s41551-024-01214-6.
35. Choi, H.; Choi, K.; Kim, D.H.; Oh, B.K.; Yim, H.; Jo, S.; Choi, C. Strategies for Targeted Delivery of Exosomes to the Brain: Advantages and Challenges. *Pharmaceutics* **2022**, *14*, 672, doi:10.3390/pharmaceutics14030672.
36. Liang, X.; Niu, Z.; Galli, V.; Howe, N.; Zhao, Y.; Wiklander, O.P.B.; Zheng, W.; Wiklander, R.J.; Corso, G.; Davies, C.; et al. Extracellular vesicles engineered to bind albumin demonstrate extended circulation time and lymph node accumulation in mouse models. *J Extracell Vesicles* **2022**, *11*, e12248, doi:10.1002/jev2.12248.
37. Stickney, Z.; Losacco, J.; McDevitt, S.; Zhang, Z.; Lu, B. Development of exosome surface display technology in living human cells. *Biochem Biophys Res Commun* **2016**, *472*, 53-59, doi:10.1016/j.bbrc.2016.02.058.
38. Jafari, D.; Shajari, S.; Jafari, R.; Mardi, N.; Gomari, H.; Ganji, F.; Forouzandeh Moghadam, M.; Samadikuchaksaraei, A. Designer Exosomes: A New Platform for Biotechnology Therapeutics. *BioDrugs* **2020**, *34*, 567-586, doi:10.1007/s40259-020-00434-x.
39. Liu, Y.; Li, D.; Liu, Z.; Zhou, Y.; Chu, D.; Li, X.; Jiang, X.; Hou, D.; Chen, X.; Chen, Y.; et al. Targeted exosome-mediated delivery of opioid receptor Mu siRNA for the treatment of morphine relapse. *Sci Rep* **2015**, *5*, 17543, doi:10.1038/srep17543.
40. Cui, G.H.; Guo, H.D.; Li, H.; Zhai, Y.; Gong, Z.B.; Wu, J.; Liu, J.S.; Dong, Y.R.; Hou, S.X.; Liu, J.R. RVG-modified exosomes derived from mesenchymal stem cells rescue memory deficits by regulating inflammatory responses in a mouse model of Alzheimer's disease. *Immun Ageing* **2019**, *16*, 10, doi:10.1186/s12979-019-0150-2.

41. Alvarez-Erviti, L.; Seow, Y.; Yin, H.; Betts, C.; Lakhal, S.; Wood, M.J. Delivery of siRNA to the mouse brain by systemic injection of targeted exosomes. *Nat Biotechnol* **2011**, *29*, 341-345, doi:10.1038/nbt.1807.
42. Ren, X.; Zhao, Y.; Xue, F.; Zheng, Y.; Huang, H.; Wang, W.; Chang, Y.; Yang, H.; Zhang, J. Exosomal DNA Aptamer Targeting alpha-Synuclein Aggregates Reduced Neuropathological Deficits in a Mouse Parkinson's Disease Model. *Mol Ther Nucleic Acids* **2019**, *17*, 726-740, doi:10.1016/j.omtn.2019.07.008.
43. He, J.; Du, Z.; Zhang, H.; Wang, B.; Xia, J. Exosomes derived from human umbilical cord mesenchymal stem cells loaded with RVG-Lamp2b and Netrin-1 promotes Schwann cell invasion and migration. *Tissue Cell* **2023**, *85*, 102219, doi:10.1016/j.tice.2023.102219.
44. Kim, H.; Yun, N.; Mun, D.; Kang, J.Y.; Lee, S.H.; Park, H.; Park, H.; Joung, B. Cardiac-specific delivery by cardiac tissue-targeting peptide-expressing exosomes. *Biochem Biophys Res Commun* **2018**, *499*, 803-808, doi:10.1016/j.bbrc.2018.03.227.
45. Kim, G.; Lee, Y.; Ha, J.; Han, S.; Lee, M. Engineering exosomes for pulmonary delivery of peptides and drugs to inflammatory lung cells by inhalation. *J Control Release* **2021**, *330*, 684-695, doi:10.1016/j.jconrel.2020.12.053.
46. Liu, W.; Liu, A.; Li, X.; Sun, Z.; Sun, Z.; Liu, Y.; Wang, G.; Huang, D.; Xiong, H.; Yu, S.; et al. Dual-engineered cartilage-targeting extracellular vesicles derived from mesenchymal stem cells enhance osteoarthritis treatment via miR-223/NLRP3/pyroptosis axis: Toward a precision therapy. *Bioact Mater* **2023**, *30*, 169-183, doi:10.1016/j.bioactmat.2023.06.012.
47. Hung, M.E.; Leonard, J.N. Stabilization of exosome-targeting peptides via engineered glycosylation. *J Biol Chem* **2015**, *290*, 8166-8172, doi:10.1074/jbc.M114.621383.
48. Vance, J.E.; Tasseva, G. Formation and function of phosphatidylserine and phosphatidylethanolamine in mammalian cells. *Biochim Biophys Acta* **2013**, *1831*, 543-554, doi:10.1016/j.bbalip.2012.08.016.
49. Wang, R.; Xiao, R.; Zeng, Z.; Xu, L.; Wang, J. Application of poly(ethylene glycol)-distearoylphosphatidylethanolamine (PEG-DSPE) block copolymers and their derivatives as nanomaterials in drug delivery. *Int J Nanomedicine* **2012**, *7*, 4185-4198, doi:10.2147/IJN.S34489.
50. Dos Santos, N.; Allen, C.; Doppen, A.M.; Anantha, M.; Cox, K.A.; Gallagher, R.C.; Karlsson, G.; Edwards, K.; Kenner, G.; Samuels, L.; et al. Influence of poly(ethylene glycol) grafting density and polymer length on liposomes: relating plasma circulation lifetimes to protein binding. *Biochim Biophys Acta* **2007**, *1768*, 1367-1377, doi:10.1016/j.bbamem.2006.12.013.
51. Mohamed, M.; Abu Lila, A.S.; Shimizu, T.; Alaaeldin, E.; Hussein, A.; Sarhan, H.A.; Szebeni, J.; Ishida, T. PEGylated liposomes: immunological responses. *Sci Technol Adv Mater* **2019**, *20*, 710-724, doi:10.1080/14686996.2019.1627174.
52. Geng, T.; Leung, E.; Chamley, L.W.; Wu, Z. Functionalisation of extracellular vesicles with cyclic-RGDyC potentially for glioblastoma targeted intracellular drug delivery. *Biomater Adv* **2023**, *149*, 213388, doi:10.1016/j.bioadv.2023.213388.
53. Liang, Y.; Duan, L.; Lu, J.; Xia, J. Engineering exosomes for targeted drug delivery. *Theranostics* **2021**, *11*, 3183-3195, doi:10.7150/thno.52570.

54. Ding, Y.N.; Li, M.Q.; Song, J.Y.; Guan, P.P.; Wang, P. Engineered exosomes improve the effects of curcumin on protecting mitochondria of neurons in Alzheimer's disease. *Mater Today Bio* **2025**, *32*, 101738, doi:10.1016/j.mtbio.2025.101738.
55. Xu, Y.; Yan, G.; Zhao, J.; Ren, Y.; Xiao, Q.; Tan, M.; Peng, L. Plant-derived exosomes as cell homogeneous nanoplatforms for brain biomacromolecules delivery ameliorate mitochondrial dysfunction against Parkinson's disease. *Nano Today* **2024**, *58*, doi:10.1016/j.nantod.2024.102438.
56. Vandergriff, A.; Huang, K.; Shen, D.; Hu, S.; Hensley, M.T.; Caranasos, T.G.; Qian, L.; Cheng, K. Targeting regenerative exosomes to myocardial infarction using cardiac homing peptide. *Theranostics* **2018**, *8*, 1869-1878, doi:10.7150/thno.20524.
57. Zheng, W.; Schurz, M.; Wiklander, R.J.; Gustafsson, O.; Gupta, D.; Slovak, R.; Traista, A.; Coluzzi, A.; Roudi, S.; Barone, A.; et al. Surface display of functional moieties on extracellular vesicles using lipid anchors. *J Control Release* **2023**, *357*, 630-640, doi:10.1016/j.jconrel.2023.04.033.
58. Jain, A.; Cheng, K. The principles and applications of avidin-based nanoparticles in drug delivery and diagnosis. *J Control Release* **2017**, *245*, 27-40, doi:10.1016/j.jconrel.2016.11.016.
59. Deng, D.; Li, X.; Zhang, J.-J.; Yin, Y.; Tian, Y.; Gan, D.; Wu, R.; Wang, J.; Tian, B.-M.; Chen, F.-M.; et al. Biotin–Avidin System-Based Delivery Enhances the Therapeutic Performance of MSC-Derived Exosomes. *ACS Nano* **2023**, *17*, 8530-8550, doi:10.1021/acsnano.3c00839.
60. Hein, C.D.; Liu, X.M.; Wang, D. Click chemistry, a powerful tool for pharmaceutical sciences. *Pharm Res* **2008**, *25*, 2216-2230, doi:10.1007/s11095-008-9616-1.
61. Mbua, N.E.; Guo, J.; Wolfert, M.A.; Steet, R.; Boons, G.J. Strain-promoted alkyne-azide cycloadditions (SPAAC) reveal new features of glycoconjugate biosynthesis. *Chembiochem* **2011**, *12*, 1912-1921, doi:10.1002/cbic.201100117.
62. Yan, X.; Chen, X.; Shan, Z.; Bi, L. Engineering Exosomes to Specifically Target the Mitochondria of Brain Cells. *ACS Omega* **2023**, *8*, 48984-48993, doi:10.1021/acsomega.3c06617.
63. Tian, T.; Zhang, H.X.; He, C.P.; Fan, S.; Zhu, Y.L.; Qi, C.; Huang, N.P.; Xiao, Z.D.; Lu, Z.H.; Tannous, B.A.; et al. Surface functionalized exosomes as targeted drug delivery vehicles for cerebral ischemia therapy. *Biomaterials* **2018**, *150*, 137-149, doi:10.1016/j.biomaterials.2017.10.012.
64. Zheng, X.; Sun, K.; Liu, Y.; Yin, X.; Zhu, H.; Yu, F.; Zhao, W. Resveratrol-loaded macrophage exosomes alleviate multiple sclerosis through targeting microglia. *J Control Release* **2023**, *353*, 675-684, doi:10.1016/j.jconrel.2022.12.026.
65. Krishnan, M.A.; Alimi, O.A.; Pan, T.; Kuss, M.; Korade, Z.; Hu, G.; Liu, B.; Duan, B. Engineering Neurotoxin-Functionalized Exosomes for Targeted Delivery to the Peripheral Nervous System. *Pharmaceutics* **2024**, *16*, 102, doi:10.3390/pharmaceutics16010102.
66. Jia, G.; Han, Y.; An, Y.; Ding, Y.; He, C.; Wang, X.; Tang, Q. NRP-1 targeted and cargo-loaded exosomes facilitate simultaneous imaging and therapy of glioma in vitro and in vivo. *Biomaterials* **2018**, *178*, 302-316, doi:10.1016/j.biomaterials.2018.06.029.
67. Haroon, K.; Zheng, H.; Wu, S.; Liu, Z.; Tang, Y.; Yang, G.Y.; Liu, Y.; Zhang, Z. Engineered exosomes mediated targeted delivery of neuroprotective peptide NR2B9c for

the treatment of traumatic brain injury. *Int J Pharm* **2024**, *649*, 123656, doi:10.1016/j.ijpharm.2023.123656.
68. Musico, A.; Zenatelli, R.; Romano, M.; Zendrini, A.; Alacqua, S.; Tassoni, S.; Paolini, L.; Urbinati, C.; Rusnati, M.; Bergese, P.; et al. Surface functionalization of extracellular vesicle nanoparticles with antibodies: a first study on the protein corona "variable". *Nanoscale Adv* **2023**, *5*, 4703-4717, doi:10.1039/d3na00280b.
69. Spanedda, M.V.; De Giorgi, M.; Heurtault, B.; Kichler, A.; Bourel-Bonnet, L.; Frisch, B. Click Chemistry for Liposome Surface Modification. *Methods Mol Biol* **2023**, *2622*, 173-189, doi:10.1007/978-1-0716-2954-3_15.
70. Frisch, B.; Hassane, F.S.; Schuber, F. Conjugation of ligands to the surface of preformed liposomes by click chemistry. *Methods Mol Biol* **2010**, *605*, 267-277, doi:10.1007/978-1-60327-360-2_18.
71. Chatterjee, B.P.; Ghosh, M.; Dasgupta, U.; Chatterjee, I.; Agrawal, S.; Singh, S.; Chowdhury, A.D.; Das, P. The Development of Antibody-Functionalized Liposomes via Click Chemistry for Precision Targeting of PD-L1-Positive Ovarian Cancer. *ACS Omega* **2026**, *11*, 9212-9220, doi:10.1021/acsomega.5c08503.
72. Oude Blenke, E.; Klaasse, G.; Merten, H.; Pluckthun, A.; Mastrobattista, E.; Martin, N.I. Liposome functionalization with copper-free "click chemistry". *J Control Release* **2015**, *202*, 14-20, doi:10.1016/j.jconrel.2015.01.027.
73. Dunn, M.R.; Jimenez, R.M.; Chaput, J.C. Analysis of aptamer discovery and technology. *Nature Reviews Chemistry* **2017**, *1*, doi:ARTN 0076
10.1038/s41570017-0076.
74. Zou, J.; Shi, M.; Liu, X.; Jin, C.; Xing, X.; Qiu, L.; Tan, W. Aptamer-Functionalized Exosomes: Elucidating the Cellular Uptake Mechanism and the Potential for Cancer-Targeted Chemotherapy. *Anal Chem* **2019**, *91*, 2425-2430, doi:10.1021/acs.analchem.8b05204.
75. Hosseini, N.F.; Amini, R.; Ramezani, M.; Saidijam, M.; Hashemi, S.M.; Najafi, R. AS1411 aptamer-functionalized exosomes in the targeted delivery of doxorubicin in fighting colorectal cancer. *Biomed Pharmacother* **2022**, *155*, 113690, doi:10.1016/j.biopha.2022.113690.
76. Esposito, C.L.; Quintavalle, C.; Ingenito, F.; Rotoli, D.; Roscigno, G.; Nuzzo, S.; Thomas, R.; Catuogno, S.; de Franciscis, V.; Condorelli, G. Identification of a novel RNA aptamer that selectively targets breast cancer exosomes. *Mol Ther Nucleic Acids* **2021**, *23*, 982-994, doi:10.1016/j.omtn.2021.01.012.
77. Wu, T.; Liu, Y.; Cao, Y.; Liu, Z. Engineering Macrophage Exosome Disguised Biodegradable Nanoplatform for Enhanced Sonodynamic Therapy of Glioblastoma. *Adv Mater* **2022**, *34*, e2110364, doi:10.1002/adma.202110364.
78. Liang, S.; Xu, H.; Ye, B.C. Membrane-Decorated Exosomes for Combination Drug Delivery and Improved Glioma Therapy. *Langmuir* **2022**, *38*, 299-308, doi:10.1021/acs.langmuir.1c02500.
79. Hosseini Shamili, F.; Alibolandi, M.; Rafatpanah, H.; Abnous, K.; Mahmoudi, M.; Kalantari, M.; Taghdisi, S.M.; Ramezani, M. Immunomodulatory properties of MSC-derived exosomes armed with high affinity aptamer toward mylein as a platform for reducing multiple sclerosis clinical score. *J Control Release* **2019**, *299*, 149-164, doi:10.1016/j.jconrel.2019.02.032.

80. Langevin, C.; Jaaro, H.; Bressanelli, S.; Fainzilber, M.; Tuffereau, C. Rabies virus glycoprotein (RVG) is a trimeric ligand for the N-terminal cysteine-rich domain of the mammalian p75 neurotrophin receptor. *J Biol Chem* **2002**, *277*, 37655-37662, doi:10.1074/jbc.M201374200.
81. Wang, Q.; Cheng, S.; Qin, F.; Fu, A.; Fu, C. Application progress of RVG peptides to facilitate the delivery of therapeutic agents into the central nervous system. *RSC Advances* **2021**, *11*, 8505-8515, doi:10.1039/d1ra00550b.
82. Kumar, P.; Wu, H.; Mcbride, J.L.; Jung, K.-E.; Hee Kim, M.; Davidson, B.L.; Kyung Lee, S.; Shankar, P.; Manjunath, N. Transvascular delivery of small interfering RNA to the central nervous system. *Nature* **2007**, *448*, 39-43, doi:10.1038/nature05901.
83. Liu, Y.; Huang, R.; Han, L.; Ke, W.; Shao, K.; Ye, L.; Lou, J.; Jiang, C. Brain-targeting gene delivery and cellular internalization mechanisms for modified rabies virus glycoprotein RVG29 nanoparticles. *Biomaterials* **2009**, *30*, 4195-4202, doi:10.1016/j.biomaterials.2009.02.051.
84. Schlich, M.; Longhena, F.; Faustini, G.; O'Driscoll, C.M.; Sinico, C.; Fadda, A.M.; Bellucci, A.; Lai, F. Anionic liposomes for small interfering ribonucleic acid (siRNA) delivery to primary neuronal cells: Evaluation of alpha-synuclein knockdown efficacy. *Nano Research* **2017**, *10*, 3496-3508, doi:10.1007/s12274-017-1561-z.
85. Bayart, C.; Mularoni, A.; Hemmani, N.; Kerachni, S.; Jose, J.; Gouet, P.; Paladino, J.; Le Borgne, M. Tetanus Toxin Fragment C: Structure, Drug Discovery Research and Production. *Pharmaceuticals (Basel)* **2022**, *15*, 756, doi:10.3390/ph15060756.
86. Calvo, A.C.; Olivan, S.; Manzano, R.; Zaragoza, P.; Aguilera, J.; Osta, R. Fragment C of tetanus toxin: new insights into its neuronal signaling pathway. *Int J Mol Sci* **2012**, *13*, 6883-6901, doi:10.3390/ijms13066883.
87. Kassa, R.; Monterroso, V.; David, L.L.; Tshala-Katumbay, D. Diagnostic and therapeutic potential of tetanus toxin-derivatives in neurological diseases. *J Mol Neurosci* **2013**, *51*, 788-791, doi:10.1007/s12031-013-0065-x.
88. Liu, J.K.; Teng, Q.; Garrity-Moses, M.; Federici, T.; Tanase, D.; Imperiale, M.J.; Boulis, N.M. A novel peptide defined through phage display for therapeutic protein and vector neuronal targeting. *Neurobiol Dis* **2005**, *19*, 407-418, doi:10.1016/j.nbd.2005.01.022.
89. Park, I.K.; Lasiene, J.; Chou, S.H.; Horner, P.J.; Pun, S.H. Neuron-specific delivery of nucleic acids mediated by Tet1-modified poly(ethylenimine). *J Gene Med* **2007**, *9*, 691-702, doi:10.1002/jgm.1062.
90. Townsend, S.A.; Evrony, G.D.; Gu, F.X.; Schulz, M.P.; Brown, R.H., Jr.; Langer, R. Tetanus toxin C fragment-conjugated nanoparticles for targeted drug delivery to neurons. *Biomaterials* **2007**, *28*, 5176-5184, doi:10.1016/j.biomaterials.2007.08.011.
91. Jia, T.; Sun, Z.; Lu, Y.; Gao, J.; Zou, H.; Xie, F.; Zhang, G.; Xu, H.; Sun, D.; Yu, Y.; et al. A dual brain-targeting curcumin-loaded polymersomes ameliorated cognitive dysfunction in intrahippocampal amyloid-beta1-42-injected mice. *Int J Nanomedicine* **2016**, *11*, 3765-3775, doi:10.2147/IJN.S94622.
92. Rizk, S.S.; Misiura, A.; Paduch, M.; Kossiakoff, A.A. Substance P derivatives as versatile tools for specific delivery of various types of biomolecular cargo. *Bioconjug Chem* **2012**, *23*, 42-46, doi:10.1021/bc200496e.
93. Ruan, C.; Liu, L.; Lu, Y.; Zhang, Y.; He, X.; Chen, X.; Zhang, Y.; Chen, Q.; Guo, Q.; Sun, T.; et al. Substance P-modified human serum albumin nanoparticles loaded with

paclitaxel for targeted therapy of glioma. *Acta Pharm Sin B* **2018**, *8*, 85-96, doi:10.1016/j.apsb.2017.09.008.
94. Rangger, C.; Helbok, A.; Sosabowski, J.; Kremser, C.; Koehler, G.; Prassl, R.; Andreae, F.; Virgolini, I.J.; von Guggenberg, E.; Decristoforo, C. Tumor targeting and imaging with dual-peptide conjugated multifunctional liposomal nanoparticles. *Int J Nanomedicine* **2013**, *8*, 4659-4671, doi:10.2147/IJN.S51927.
95. Son, S.; Hwang, D.W.; Singha, K.; Jeong, J.H.; Park, T.G.; Lee, D.S.; Kim, W.J. RVG peptide tethered bioreducible polyethylenimine for gene delivery to brain. *J Control Release* **2011**, *155*, 18-25, doi:10.1016/j.jconrel.2010.08.011.
96. C., L.C.; Kapadia, S.S., C. M. Central Projections of the Sciatic, Saphenous, Median, and Ulnar Nerves of the Rat Demonstrated by Transganglionic Transport of Choleragenoid-HRP (B-HRP) and Wheat Germ Agglutinin-HRP (WGA-HRP). *J Comp Neurol* **1991**, *311*, 546-562, doi:doi.org/10.1002/cne.903110409Digital Object Identifier (DOI).
97. Reinhold, A.K.; Rittner, H.L. Characteristics of the nerve barrier and the blood dorsal root ganglion barrier in health and disease. *Exp Neurol* **2020**, *327*, 113244, doi:10.1016/j.expneurol.2020.113244.
98. Langert, K.A.; Brey, E.M. Strategies for Targeted Delivery to the Peripheral Nerve. *Front Neurosci* **2018**, *12*, 887, doi:10.3389/fnins.2018.00887.
99. Yanez-Mo, M.; Siljander, P.R.; Andreu, Z.; Zavec, A.B.; Borras, F.E.; Buzas, E.I.; Buzas, K.; Casal, E.; Cappello, F.; Carvalho, J.; et al. Biological properties of extracellular vesicles and their physiological functions. *J Extracell Vesicles* **2015**, *4*, 27066, doi:10.3402/jev.v4.27066.
100. Gu, Z.; Xue, W.; Mao, G.; Pei, Z.; Li, J.; Sun, M.; Zhang, X.; Zhang, S.; Li, S.; Cen, J.; et al. Native and Engineered Extracellular Vesicles for the Treatment of Acute Lung Injury and Acute Respiratory Distress Syndrome. *Small Sci* **2025**, *5*, 2400606, doi:10.1002/smsc.202400606.
101. Bulbake, U.; Doppalapudi, S.; Kommineni, N.; Khan, W. Liposomal Formulations in Clinical Use: An Updated Review. *Pharmaceutics* **2017**, *9*, doi:10.3390/pharmaceutics9020012.
102. van der Koog, L.; Gandek, T.B.; Nagelkerke, A. Liposomes and Extracellular Vesicles as Drug Delivery Systems: A Comparison of Composition, Pharmacokinetics, and Functionalization. *Adv Healthc Mater* **2022**, *11*, e2100639, doi:10.1002/adhm.202100639.
103. Kuziemko, G.M.; Stroh, M.; Stevens, R.C. Cholera toxin binding affinity and specificity for gangliosides determined by surface plasmon resonance. *Biochemistry* **1996**, *35*, 6375-6384, doi:10.1021/bi952314i.
104. Pang, H.; Le, P.U.; Nabi, I.R. Ganglioside GM1 levels are a determinant of the extent of caveolae/raft-dependent endocytosis of cholera toxin to the Golgi apparatus. *J Cell Sci* **2004**, *117*, 1421-1430, doi:10.1242/jcs.01009.
105. Monsigny, M.; Sene, C.; Obrenovitch, A.; Roche, A.C.; Delmotte, F.; Boschetti, E. Properties of succinylated wheat-germ agglutinin. *Eur J Biochem* **1979**, *98*, 39-45, doi:10.1111/j.1432-1033.1979.tb13157.x.
106. Song, Q.; Yao, L.; Huang, M.; Hu, Q.; Lu, Q.; Wu, B.; Qi, H.; Rong, Z.; Jiang, X.; Gao, X.; et al. Mechanisms of transcellular transport of wheat germ agglutinin-functionalized polymeric nanoparticles in Caco-2 cells. *Biomaterials* **2012**, *33*, 6769-6782, doi:10.1016/j.biomaterials.2012.05.066.

107. Soder, R.P.; Splan, D.; Dudley, N.R.; Szczypka, M.; Abhyankar, S. Large Scale Manufacturing of Wharton's Jelly Mesenchymal Stromal Cells for Clinical Use. *Stem Cells Int* **2025**, *2025*, 5167739, doi:10.1155/sci/5167739.
108. Wright, A.; Snyder, O.L.; He, H.; Christenson, L.K.; Fleming, S.; Weiss, M.L. Procoagulant Activity of Umbilical Cord-Derived Mesenchymal Stromal Cells' Extracellular Vesicles (MSC-EVs). *Int J Mol Sci* **2023**, *24*, doi:10.3390/ijms24119216.
109. Zhang, H. Thin-Film Hydration Followed by Extrusion Method for Liposome Preparation. In *Liposomes: Methods and Protocols*, 2 ed.; D'Souza, G.G.M., Ed.; Methods in Molecular Biology; Humana: New York, NY, USA, 2017; Volume 1522, pp. 17-22.
110. Sule, R.; Rivera, G.; Gomes, A.V. Western blotting (immunoblotting): history, theory, uses, protocol and problems. *Biotechniques* **2023**, *75*, 99-114, doi:10.2144/btn-2022-0034.
111. Hu, S.; Qiao, L.; Cheng, K. Generation and Manipulation of Exosomes. In *Cardiac Regeneration: Methods and Protocols*, 1 ed.; Poss, K.D.K., Bernhard, Ed.; Methods in Molecular Biology; Humana: 2021; Volume 2158, pp. 295-305.
112. Im, K.; Mareninov, S.; Diaz, M.F.P.; Yong, W.H. An Introduction to Performing Immunofluorescence Staining. In *Biobanking: Methods and Protocols*, 1 ed.; Yong, W.H., Ed.; Methods in Molecular Biology; Humana Press: New York, NY, USA, 2019; pp. 299-311.
113. Schindelin, J.; Arganda-Carreras, I.; Frise, E.; Kaynig, V.; Longair, M.; Pietzsch, T.; Preibisch, S.; Rueden, C.; Saalfeld, S.; Schmid, B.; et al. Fiji: an open-source platform for biological-image analysis. *Nat Methods* **2012**, *9*, 676-682, doi:10.1038/nmeth.2019.
114. Ershov, D.; Phan, M.S.; Pylvanainen, J.W.; Rigaud, S.U.; Le Blanc, L.; Charles-Orszag, A.; Conway, J.R.W.; Laine, R.F.; Roy, N.H.; Bonazzi, D.; et al. TrackMate 7: integrating state-of-the-art segmentation algorithms into tracking pipelines. *Nat Methods* **2022**, *19*, 829-832, doi:10.1038/s41592-022-01507-1.
115. Obata, K.; Yamanaka, H.; Dai, Y.; Mizushima, T.; Fukuoka, T.; Tokunaga, A.; Noguchi, K. Differential activation of MAPK in injured and uninjured DRG neurons following chronic constriction injury of the sciatic nerve in rats. *Eur J Neurosci* **2004**, *20*, 2881-2895, doi:10.1111/j.1460-9568.2004.03754.x.
116. R Core Team *R: A Language and Environment for Statistical Computing*, 4.3.3; R Foundation for Statistical Computing: Vienna, Austria, 2025.
117. R Core Team *R: A Language and Environment for Statistical Computing*, 4.6.1; R Foundation for Statistical Computing: Vienna, Austria, 2026.
118. Wright, A.; Snyder, O.L.; Christenson, L.K.; He, H.; Weiss, M.L. Effect of Pre-Processing Storage Condition of Cell Culture-Conditioned Medium on Extracellular Vesicles Derived from Human Umbilical Cord-Derived Mesenchymal Stromal Cells. *Int J Mol Sci* **2022**, *23*, 7716, doi:10.3390/ijms23147716.
119. Haraszti, R.A.; Miller, R.; Stoppato, M.; Sere, Y.Y.; Coles, A.; Didiot, M.C.; Wollacott, R.; Sapp, E.; Dubuke, M.L.; Li, X.; et al. Exosomes Produced from 3D Cultures of MSCs by Tangential Flow Filtration Show Higher Yield and Improved Activity. *Mol Ther* **2018**, *26*, 2838-2847, doi:10.1016/j.ymthe.2018.09.015.
120. Petry, F.; Smith, J.R.; Leber, J.; Salzig, D.; Czermak, P.; Weiss, M.L. Manufacturing of Human Umbilical Cord Mesenchymal Stromal Cells on Microcarriers in a Dynamic

System for Clinical Use. *Stem Cells Int* **2016**, *2016*, 4834616, doi:10.1155/2016/4834616.
121. Ulpiano, C.; Salvador, W.; Franchi-Mendes, T.; Huang, M.C.; Lin, Y.H.; Lin, H.T.; Rodrigues, C.A.V.; Fernandes-Platzgummer, A.; Cabral, J.M.S.; Monteiro, G.A.; et al. Continuous collection of human mesenchymal-stromal-cell-derived extracellular vesicles from a stirred tank reactor operated under xenogeneic-free conditions for therapeutic applications. *Stem Cell Res Ther* **2025**, *16*, 210, doi:10.1186/s13287-025-04341-2.
122. Kronstadt, S.M.; Patel, D.B.; Born, L.J.; Levy, D.; Lerman, M.J.; Mahadik, B.; McLoughlin, S.T.; Fasuyi, A.; Fowlkes, L.; Van Heyningen, L.H.; et al. Mesenchymal Stem Cell Culture within Perfusion Bioreactors Incorporating 3D-Printed Scaffolds Enables Improved Extracellular Vesicle Yield with Preserved Bioactivity. *Adv Healthc Mater* **2023**, *12*, e2300584, doi:10.1002/adhm.202300584.
123. de Almeida Fuzeta, M.; Bernardes, N.; Oliveira, F.D.; Costa, A.C.; Fernandes-Platzgummer, A.; Farinha, J.P.; Rodrigues, C.A.V.; Jung, S.; Tseng, R.J.; Milligan, W.; et al. Scalable Production of Human Mesenchymal Stromal Cell-Derived Extracellular Vesicles Under Serum-/Xeno-Free Conditions in a Microcarrier-Based Bioreactor Culture System. *Front Cell Dev Biol* **2020**, *8*, 553444, doi:10.3389/fcell.2020.553444.
124. Kink, J.A.; Bellio, M.A.; Forsberg, M.H.; Lobo, A.; Thickens, A.S.; Lewis, B.M.; Ong, I.M.; Khan, A.; Capitini, C.M.; Hematti, P. Large-scale bioreactor production of extracellular vesicles from mesenchymal stromal cells for treatment of acute radiation syndrome. *Stem Cell Research & Therapy* **2024**, *15*, doi:10.1186/s13287-024-03688-2.
125. Gong, S.; Li, N.; Peng, Q.; Wang, F.; Du, R.; Zhang, B.; Wang, J.; Han, L.; Zhang, Y.; Ning, Z.; et al. A scalable platform for EPSC-Induced MSC extracellular vesicles with therapeutic potential. *Stem Cell Res Ther* **2025**, *16*, 426, doi:10.1186/s13287-025-04507-y.
126. Webber, J.; Clayton, A. How pure are your vesicles? *Journal of Extracellular Vesicles* **2013**, *2*, 19861, doi:10.3402/jev.v2i0.19861.
127. Bellotti, C.; Lang, K.; Kuplennik, N.; Sosnik, A.; Steinfeld, R. High-grade extracellular vesicles preparation by combined size-exclusion and affinity chromatography. *Scientific Reports* **2021**, *11*, doi:10.1038/s41598-021-90022-y.
128. Miyata, T.; Oshiro, S.; Harakuni, T.; Taira, T.; Matsuzaki, G.; Arakawa, T. Physicochemically stable cholera toxin B subunit pentamer created by peripheral molecular constraints imposed by de novo-introduced intersubunit disulfide crosslinks. *Vaccine* **2012**, *30*, 4225-4232, doi:10.1016/j.vaccine.2012.04.047.
129. Carcea, M.; Melloni, S.; Narducci, V.; Turfani, V. Wheat Germ Agglutinin (WGA): Its Nature, Biological Role, Significance in Human Nutrition, and Possibility to Be Used as Marker of Whole-Grain Status in Wheat-Based Foods. *Foods* **2024**, *13*, doi:10.3390/foods13182990.
130. Nizamudeen, Z.A.; Xerri, R.; Parmenter, C.; Suain, K.; Markus, R.; Chakrabarti, L.; Sottile, V. Low-Power Sonication Can Alter Extracellular Vesicle Size and Properties. *Cells* **2021**, *10*, doi:10.3390/cells10092413.
131. Ong, S.G.; Chitneni, M.; Lee, K.S.; Ming, L.C.; Yuen, K.H. Evaluation of Extrusion Technique for Nanosizing Liposomes. *Pharmaceutics* **2016**, *8*, doi:10.3390/pharmaceutics8040036.

132. Colja, S.; Jovcevska, I.; Samec, N.; Romih, R.; Zottel, A. Sonication is a suitable method for loading nanobody into glioblastoma small extracellular vesicles. *Heliyon* **2023**, *9*, e15674, doi:10.1016/j.heliyon.2023.e15674.
133. Chen, Y.; Wang, L.; Yu, X.; Mao, W.; Wan, Y. Ultrasonication outperforms electroporation for extracellular vesicle cargo depletion. *Extracell Vesicle* **2024**, *4*, doi:10.1016/j.vesic.2024.100052.
134. Zuris, J.A.; Thompson, D.B.; Shu, Y.; Guilinger, J.P.; Bessen, J.L.; Hu, J.H.; Maeder, M.L.; Joung, J.K.; Chen, Z.Y.; Liu, D.R. Cationic lipid-mediated delivery of proteins enables efficient protein-based genome editing in vitro and in vivo. *Nat Biotechnol* **2015**, *33*, 73-80, doi:10.1038/nbt.3081.
135. Breyne, K.; Ughetto, S.; Rufino-Ramos, D.; Mahjoum, S.; Grandell, E.A.; de Almeida, L.P.; Breakefield, X.O. Exogenous loading of extracellular vesicles, virus-like particles, and lentiviral vectors with supercharged proteins. *Commun Biol* **2022**, *5*, 485, doi:10.1038/s42003-022-03440-7.
136. Moreira, R.; Nobrega, C.; de Almeida, L.P.; Mendonca, L. Brain-targeted drug delivery - nanovesicles directed to specific brain cells by brain-targeting ligands. *J Nanobiotechnology* **2024**, *22*, 260, doi:10.1186/s12951-024-02511-7.
137. LaMotte, C.C.; Kapadia, S.E.; Shapiro, C.M. Central projections of the sciatic, saphenous, median, and ulnar nerves of the rat demonstrated by transganglionic transport of choleragenoid-HRP (B-HRP) and wheat germ agglutinin-HRP (WGA-HRP). *J Comp Neurol* **1991**, *311*, 546-562, doi:10.1002/cne.903110409.
138. Kallogjerovic, S.; Velazquez-Quesada, I.; Hadap, R.; Gligorijevic, B. Retrograde tracing of breast cancer-associated sensory neurons. *J Microsc* **2025**, *298*, 232-244, doi:10.1111/jmi.13340.
139. Wolf, A.A.; Fujinaga, Y.; Lencer, W.I. Uncoupling of the cholera toxin-G(M1) ganglioside receptor complex from endocytosis, retrograde Golgi trafficking, and downstream signal transduction by depletion of membrane cholesterol. *J Biol Chem* **2002**, *277*, 16249-16256, doi:10.1074/jbc.M109834200.
140. L., T.M.; Skretting, G.; V., D.B.; Sandvig, K. Internalization of cholera toxin by different endocytic mechanisms. *J Cell Sci* **2001**, 3737-3747, doi:10.1242/jcs.114.20.3737. PMID: 11707525.
141. Shogomori, H.; Futerman, A.H. Cholera toxin is found in detergent-insoluble rafts/domains at the cell surface of hippocampal neurons but is internalized via a raft-independent mechanism. *J Biol Chem* **2001**, *276*, 9182-9188, doi:10.1074/jbc.M009414200.
142. Massol, R.H.; Larsen, J.E.; Fujinaga, Y.; Lencer, W.I.; Kirchhausen, T. Cholera toxin toxicity does not require functional Arf6- and dynamin-dependent endocytic pathways. *Mol Biol Cell* **2004**, *15*, 3631-3641, doi:10.1091/mbc.e04-04-0283.
143. Levy, S.L.; White, J.J.; Lackey, E.P.; Schwartz, L.; Sillitoe, R.V. WGA-Alexa Conjugates for Axonal Tracing. *Curr Protoc Neurosci* **2017**, *79*, 1 28 21-21 28 24, doi:10.1002/cpns.28.
144. Sethi, A.; Wands, A.M.; Mettlen, M.; Krishnamurthy, S.; Wu, H.; Kohler, J.J. Cell type and receptor identity regulate cholera toxin subunit B (CTB) internalization. *Interface Focus* **2019**, *9*, 20180076, doi:10.1098/rsfs.2018.0076.

145. Wang, J.; Li, W.; Lu, Z.; Zhang, L.; Hu, Y.; Li, Q.; Du, W.; Feng, X.; Jia, H.; Liu, B.-F. The use of RGD-engineered exosomes for enhanced targeting ability and synergistic therapy toward angiogenesis. *Nanoscale* **2017**, *9*, 15598-15605, doi:10.1039/c7nr04425a.
146. Wu, J.Y.; Li, Y.J.; Wang, J.; Hu, X.B.; Huang, S.; Luo, S.; Xiang, D.X. Multifunctional exosome-mimetics for targeted anti-glioblastoma therapy by manipulating protein corona. *J Nanobiotechnology* **2021**, *19*, 405, doi:10.1186/s12951-021-01153-3.
147. Alkilany, A.M.; Zhu, L.; Weller, H.; Mews, A.; Parak, W.J.; Barz, M.; Feliu, N. Ligand density on nanoparticles: A parameter with critical impact on nanomedicine. *Adv Drug Deliv Rev* **2019**, *143*, 22-36, doi:10.1016/j.addr.2019.05.010.
148. Gonzalez Porras, M.A.; Durfee, P.N.; Gregory, A.M.; Sieck, G.C.; Brinker, C.J.; Mantilla, C.B. A novel approach for targeted delivery to motoneurons using cholera toxin-B modified protocells. *J Neurosci Methods* **2016**, *273*, 160-174, doi:10.1016/j.jneumeth.2016.09.003.
149. Zhang, Y.; Walker, J.B.; Minic, Z.; Liu, F.; Goshgarian, H.; Mao, G. Transporter protein and drug-conjugated gold nanoparticles capable of bypassing the blood-brain barrier. *Scientific Reports* **2016**, *6*, 25794, doi:10.1038/srep25794.
150. Wang, W.; Hassan, M.M.; Kapoor-Kaushik, N.; Livni, L.; Musrie, B.; Tang, J.; Mahmud, Z.; Lai, S.; Wich, P.R.; Ananthanarayanan, V.; et al. Neural Tracing Protein-Functionalized Nanoparticles Capable of Fast Retrograde Axonal Transport in Live Neurons. *Small* **2024**, *20*, e2311921, doi:10.1002/smll.202311921.
151. Kim, M.; Kim, G.; Hwang, D.W.; Lee, M. Delivery of High Mobility Group Box-1 siRNA Using Brain-Targeting Exosomes for Ischemic Stroke Therapy. *J Biomed Nanotechnol* **2019**, *15*, 2401-2412, doi:10.1166/jbn.2019.2866.
152. Cui, G.-H.; Guo, H.-D.; Li, H.; Zhai, Y.; Gong, Z.-B.; Wu, J.; Liu, J.-S.; Dong, Y.-R.; Hou, S.-X.; Liu, J.-R. RVG-modified exosomes derived from mesenchymal stem cells rescue memory deficits by regulating inflammatory responses in a mouse model of Alzheimer's disease. *Immunity & Ageing* **2019**, *16*, doi:10.1186/s12979-019-0150-2.
153. Coulon, P.; Derbin, C.; Kucera, P.; Lafay, F.; Prehaud, C.; Flamand, A. Invasion of the peripheral nervous systems of adult mice by the CVS strain of rabies virus and its avirulent derivative AvO1. *J Virol* **1989**, *63*, 3550-3554, doi:10.1128/JVI.63.8.3550-3554.1989.
154. Tuffereau, C.; Schmidt, K.; Langevin, C.; Lafay, F.; Dechant, G.; Koltzenburg, M. The rabies virus glycoprotein receptor p75NTR is not essential for rabies virus infection. *J Virol* **2007**, *81*, 13622-13630, doi:10.1128/JVI.02368-06.
155. Huang, J.; Chowhdury, S.I.; Weiss, M.L. Distribution of sympathetic preganglionic neurons innervating the kidney in the rat: PRV transneuronal tracing and serial reconstruction. *Auton Neurosci* **2002**, *95*, 57-70, doi:10.1016/s1566-0702(01)00356-3.
156. Hoover, J.E.; Strick, P.L. The organization of cerebellar and basal ganglia outputs to primary motor cortex as revealed by retrograde transneuronal transport of herpes simplex virus type 1. *J Neurosci* **1999**, *19*, 1446-1463, doi:10.1523/JNEUROSCI.19-04-01446.1999.
157. Ugolini, G.; Kuypers, H.G.; Simmons, A. Retrograde transneuronal transfer of herpes simplex virus type 1 (HSV 1) from motoneurones. *Brain Res* **1987**, *422*, 242-256, doi:10.1016/0006-8993(87)90931-0.

158. Schwab, M.E.; Thoenen, H. Retrograde axonal and transsynaptic transport of macromolecules: physiological and pathophysiological importance. *Agents Actions* **1977**, *7*, 361-368, doi:10.1007/BF01969569.
159. Herreros, J.; Lalli, G.; Montecucco, C.; Schiavo, G. Tetanus toxin fragment C binds to a protein present in neuronal cell lines and motoneurons. *J Neurochem* **2000**, *74*, 1941-1950, doi:10.1046/j.1471-4159.2000.0741941.x.
160. Critchley, D.R.; Nelson, P.G.; Habig, W.H.; Fishman, P.H. Fate of tetanus toxin bound to the surface of primary neurons in culture: evidence for rapid internalization. *J Cell Biol* **1985**, *100*, 1499-1507, doi:10.1083/jcb.100.5.1499.
161. Chen, C.; Fu, Z.; Kim, J.J.; Barbieri, J.T.; Baldwin, M.R. Gangliosides as high affinity receptors for tetanus neurotoxin. *J Biol Chem* **2009**, *284*, 26569-26577, doi:10.1074/jbc.M109.027391.
162. Evinger, C.; Erichsen, J.T. Transsynaptic retrograde transport of fragment C of tetanus toxin demonstrated by immunohistochemical localization. *Brain Res* **1986**, *380*, 383-388, doi:10.1016/0006-8993(86)90241-6.
163. Fishman, P.S.; Carrigan, D.R. Retrograde transneuronal transfer of the C-fragment of tetanus toxin. *Brain Res* **1987**, *406*, 275-279, doi:10.1016/0006-8993(87)90792-x.
164. Andreu, A.; Fairweather, N.; Miller, A.D. Clostridium neurotoxin fragments as potential targeting moieties for liposomal gene delivery to the CNS. *Chembiochem* **2008**, *9*, 219-231, doi:10.1002/cbic.200700277.
165. Oliveira, H.; Fernandez, R.; Pires, L.R.; Martins, M.C.; Simoes, S.; Barbosa, M.A.; Pego, A.P. Targeted gene delivery into peripheral sensorial neurons mediated by self-assembled vectors composed of poly(ethylene imine) and tetanus toxin fragment c. *J Control Release* **2010**, *143*, 350-358, doi:10.1016/j.jconrel.2010.01.018.
166. Oliveira, H.; Pires, L.R.; Fernandez, R.; Martins, M.C.; Simoes, S.; Pego, A.P. Chitosan-based gene delivery vectors targeted to the peripheral nervous system. *J Biomed Mater Res A* **2010**, *95*, 801-810, doi:10.1002/jbm.a.32874.
167. Mattar, C.N.; Waddington, S.N.; Biswas, A.; Johana, N.; Ng, X.W.; Fisk, A.S.; Fisk, N.M.; Tan, L.G.; Rahim, A.A.; Buckley, S.M.; et al. Systemic delivery of scAAV9 in fetal macaques facilitates neuronal transduction of the central and peripheral nervous systems. *Gene Ther* **2013**, *20*, 69-83, doi:10.1038/gt.2011.216.
168. Ugolini, G. Transneuronal transfer of herpes simplex virus type 1 (HSV 1) from mixed limb nerves to the CNS. I. Sequence of transfer from sensory, motor, and sympathetic nerve fibres to the spinal cord. *J Comp Neurol* **1992**, *326*, 527-548, doi:10.1002/cne.903260404.